



**INVESTIGATION OF THE HIGH-CYCLE FATIGUE LIFE OF SELECTIVE  
LASER MELTED AND HOT ISOSTATICALLY PRESSED TI-6AL-4V**

THESIS

Kevin D. Rekedal, Captain, USAF  
AFIT-ENY-MS-15-M-212

**DEPARTMENT OF THE AIR FORCE  
AIR UNIVERSITY**

***AIR FORCE INSTITUTE OF TECHNOLOGY***

**Wright-Patterson Air Force Base, Ohio**

DISTRIBUTION STATEMENT A. APPROVED FOR PUBLIC RELEASE;  
DISTRIBUTION UNLIMITED.

The views expressed in this thesis are those of the author and do not reflect the official policy or position of the United States Air Force, the Department of Defense, or the United States Government.

This material is declared a work of the U.S. Government and is not subject to copyright protection in the United States.

AFIT-ENY-MS-15-M-212

INVESTIGATION OF THE HIGH-CYCLE FATIGUE LIFE OF SELECTIVE LASER  
MELTED AND HOT ISOSTATICALLY PRESSED TI-6AL-4V

THESIS

Presented to the Faculty

Department of Aeronautics and Astronautics

Graduate School of Engineering and Management

Air Force Institute of Technology

Air University

Air Education and Training Command

In Partial Fulfillment of the Requirements for the  
Degree of Master of Science in Aeronautical Engineering

Kevin D. Rekedal, BS

Captain, USAF

March 2015

DISTRIBUTION STATEMENT A. APPROVED FOR PUBLIC RELEASE;  
DISTRIBUTION UNLIMITED.

AFIT-ENY-MS-15-M-212

INVESTIGATION OF THE HIGH-CYCLE FATIGUE LIFE OF SELECTIVE LASER  
MELTED AND HOT ISOSTATICALLY PRESSED TI-6AL-4V

Kevin D. Rekedal, BS  
Captain, USAF

Committee Membership:

Maj David Liu, PhD  
Chair

Timothy Radsick, PhD  
Member

Alan L. Jennings, PhD  
Member

### **Abstract**

Experimental research was conducted on the effectiveness of Hot Isostatic Pressing (HIP) to improve the high-cycle fatigue life of Selective Laser Melted Ti-6Al-4v (SLM Ti-64). A thorough understanding of the fatigue life performance for additively manufactured parts is necessary before such parts are utilized in an operational capacity in Department of Defense (DoD) systems. Such applications include the rapid, on-demand fabrication of replacement parts during contingency operations or the production of light-weight topology-optimized components. This research assesses the fatigue life of SLM Ti-64 test specimens built directly to net dimensions without any subsequent surface machining. The configuration is designed as representative of end-use parts where further surface machining is unavailable or undesirable. Past research suggests utilization of HIP as a densification process to reduce the negative impact on fatigue life from internal porosity within SLM Ti-64. The impact of HIP on the rough surface of SLM Ti-64 to remove stress concentrations on the surface is not addressed in literature. The experimental data from this research demonstrates HIP improves high-cycle fatigue-life of un-machined test specimens by 61.4% at a maximum stress level of 500 MPa and 102% at a maximum stress level of 300 MPa.

## **Acknowledgments**

I would like to express my appreciation to the Aircraft Survivability Program for sponsoring this research. I would also like to thank my research advisor, Major David Liu, for the guidance and support provided throughout this effort and my thesis committee members Dr. Alan Jennings and Dr. Timothy Radsick. I greatly appreciate Dr. Radsick's willingness to see this effort through and remain on the committee even after his retirement from active duty military service while serving on the faculty at the Air Force Institute of Technology.

I would also like to express my appreciation to Mr. Barry Page for providing support with the government purchasing process and laboratory facilities management, Mr. Wilbur Lacy for providing outstanding technical support throughout multiple testing machine breakdowns, and Dr. Heath Misak for providing guidance on material testing and equipment operation. Additionally, I would to thank the Air Force Research Laboratory Materials Directorate for providing open access to their Materials Characterization Laboratory (MCL). Dr. Kathleen Shugart and Mr. Michael Velez from UES, Inc. provided a great deal of support at the MCL. Dr. Shugart provided several hours of exceptional training on the FEI Quanta scanning electron microscope and Mr. Velez provided numerous hours of support, instruction, and oversight to assist with the preparation of metallographic specimens.

Kevin D. Rekedal

# Table of Contents

	Page
Abstract .....	iv
Acknowledgments.....	v
List of Figures .....	viii
List of Tables .....	xii
Nomenclature .....	xiii
Abbreviations .....	xv
I. Introduction.....	1
1.1. Motivation for Research.....	1
1.2. Research Scope .....	4
1.3. Problem Statement .....	5
1.4. Research Objectives .....	6
1.5. Assumptions and Limitations.....	7
II. Background Information and Previous Research .....	9
2.1. Additive Manufacturing Overview .....	9
2.2. Overview of Powder Bed Fusion Processes.....	15
2.3. Material Properties and Microstructure of SLM Ti-64 .....	18
2.4. Hot Isostatic Pressing .....	23
2.5. High-Cycle Fatigue .....	25
2.6. Previous Ti-6Al-4v Fatigue Life Research .....	30
III. Test Methodology and Procedures .....	37
3.1. Applicable Standards and Guidance .....	37
3.2. Test Specimen Design.....	38
3.3. Test Specimen Manufacturing .....	42
3.4. Post-Processing Heat Treatment .....	52
3.5. Summary of Final Specimen Configurations .....	53
3.6. Tensile Testing .....	54
3.7. Fatigue Testing.....	59
3.8. Fracture Surface Examination.....	64
3.9. Surface Metallographic Examination.....	66

IV. Results and Analysis.....	68
4.1. Inspection of Manufactured Test Specimens .....	68
4.2. Tensile Test Results .....	76
4.3. Fatigue Test Results .....	81
4.4. Examination of Fracture Surfaces .....	88
4.5. Metallographic Results.....	98
4.6. Fatigue Life Results of HIP Specimens with Machined Edges .....	102
V. Conclusions and Recommendations .....	106
5.1. Review of Research Objectives.....	106
5.2. Discussion of Results .....	109
5.3. Recommendations for Future Work.....	113
Bibliography .....	116

## List of Figures

Figure	Page
1. Sample of possible stress-life fatigue behaviors. ....	26
2. ISO/ASTM 5291:2013 Orthogonal Orientation Coordinate System. ....	38
3. Tensile specimen design dimensions utilized for this study. ....	40
4. Fatigue specimen design dimensions utilized for this study. ....	42
5. EOSINT M 280 used for test specimen fabrication. ....	44
6. Photograph of first build plate consisting of 10 tensile and 19 fatigue specimens. ....	46
7. Photograph of second build plate (left) consisting of 18 fatigue specimens and third build plate (right) consisting of 10 tensile and 28 fatigue specimens. ....	47
8. Cutting path of the wire-EDM to remove specimens from the substrate plate. ....	48
9. Depiction of the stair-step effect on inclined surfaces resulting from the layered build process. ....	48
10. Optical microscope images taken with 0.63× objective lens showing a comparison of the surface quality between the as-built edge and the edge cut by wire-EDM along the uniform gauge section of a tensile specimen. ....	49
11. Photograph of Build 2 showing the reduced-density support material underneath the parts. ....	50
12. MTS Landmark Servo-Hydraulic Test System. ....	55
13. MTS model 632.53E-14 extensometer installed during tension test. ....	56
14. Sample elongation at break measurement using optical microscope as viewed at 5× magnification through a 0.63× objective lens. ....	57
15. Sample stress vs. strain curve. ....	58
16. Zeiss Discovery V12 Optical Microscope. ....	64

Figure	Page
17. FEI Quanta 600F SEM.....	65
18. Polished and etched metallographic specimen. ....	67
19. Zeiss Observer.Z1m inverted microscope. ....	67
20. Tensile specimen measurement points.....	69
21. Fatigue specimen measurement points. ....	69
22. Photograph of fatigue specimens illustrating the asymmetric shape of the Build 2/3 specimen (shown in front) grip areas against the profile of a Build 2 specimen (shown in rear) resulting from the removal of residual support material and machining of a flat reference plane.....	71
23. Photographs of Build 1 fatigue specimens stacked together to illustrate asymmetry in the specimen geometry resulting from warped substrate plate.....	73
24. Optical microscope image taken with a 0.63× objective lens of fatigue specimens illustrating the reduced stair-stepping effect in a Build 2/3 specimen (bottom) with 30 μm layers compared to a Build 1 specimen (top) with 60 μm layers.....	74
25. Photographs of tool mark from wire-EDM (A) and surface pitting (B) remaining after removal of support material. ....	75
26. Original stress vs. strain data for Build 1 (60 μm layer thickness) stress-relieved configuration. ....	77
27. Corrected stress vs. strain data for Build 1 (60 μm layer thickness) stress-relieved configuration with strain values adjusted for calibration error.....	77
28. Stress vs. strain plot for the as-built (Build 2/3, 30 μm layer thickness), stress-relieved (Build 2/3, 30 μm layer thickness), and HIP-treated (Build 1, 60 μm layer thickness) configurations.....	79
29. Staircase data for stress-relieved configuration separated by build where symbol ‘X’ denotes a failure and ‘O’ denotes a run-out.....	82
30. S-N plot for stress-relieved configuration with Build 1 (60 μm layers) and Build 2/3 (30 μm layers) presented as separate populations.....	84

Figure	Page
31. Staircase data for HIP-treated configuration where symbol ‘X’ denotes a failure and ‘O’ denotes a run-out. ....	85
32. S-N Plot for stress-relieved and HIP configurations where stress-relieved specimens from Build 1 and Build 2/3 are treated as a single population. ....	87
33. Typical fatigue crack location in a stress-relieved specimen initiating from the as-built edge of the specimen. ....	88
34. Optical microscope image at 12× magnification with 0.63× objective lens showing the fatigue fracture surface of a HIP specimen (F-41) indicating the direction of crack growth, crack propagation region, and fast fracture (overload) region. ....	89
35. SEM images of the fast fracture region in a stress- relieved specimen (F-14) showing ductile dimpling. ....	90
36. SEM images of smooth fracture region in a stress-relieved specimen (F-14) showing (A) typical surface appearance without striations visible at 359 μm HFW and (B) region with visible striations at 128 μm HFW. ....	91
37. SEM images of fatigue fracture surface showing secondary cracking from fatigue damage accumulation in a stress-relieved specimen (F-11). ....	92
38. Optical microscope images of an internal defect on the fatigue fracture surface of a stress-relieved specimen (F-10). ....	93
39. SEM images of a surface defect in a stress-relieved specimen (F-11) indicating a possible fatigue crack initiation site. ....	94
40. SEM image of HIP-treated specimen F-35 where crack initiation occurred at the wire-EDM surface; areas A and B denote subsurface void locations shown in greater detail in Figure 41. ....	96
41. SEM images of subsurface voids near the wire-EDM surface of HIP-treated specimen F-35 with un-melted Ti-64 particles trapped within the voids. ....	96
42. Results of SEM/EDX analysis to identify the composition of trapped particles within subsurface defect in specimen F-35. ....	97
43. Optical micrographs of as-built, stress-relieved, and HIP configurations. ....	99

Figure	Page
44. SEM micrographs of as-built, stress-relieved, and HIP configurations.....	100
45. Optical image (A) showing dark spots resembling porosity but identified as surface contamination as shown in the SEM image (B). .....	101
46. S-N plot for stress-relieved, HIP-treated, and an additional HIP-treated configuration with machined edges to eliminate the effects of stair-stepping .....	103
47. Optical microscope image at 12× magnification with a 0.63× objective lens of the fatigue fracture surface for specimen F-65 showing crack initiation from the mid-point of the specimen's width. ....	105
48. Stress-life comparison of the experimental HCF data with previous research on stress-relieved Ti-64 specimens and the typical expected range of wrought material. ....	111

## List of Tables

Table	Page
1. AM process categories from ASTM F2792-12a.....	10
2. Comparison of typical EOS DMLS Ti-64 mechanical properties with minimum industry standard values for wrought and powder bed fusion material. ....	23
3. Summary of configurations in previous SLM Ti-64 fatigue studies. ....	31
4. ASTM E8/E8M specifications for subsize tensile specimens and the nominal design specifications utilized for this study. ....	40
5. ASTM E466-07 requirements for axial fatigue specimens and the design specifications utilized for this study. ....	42
6. Summary of specimen quantities, layer thickness, and build time. ....	51
7. Summary of specimen configurations and quantities. ....	54
8. Summary of specimen measurements.....	70
9. Static tensile properties for the as-built, stress-relieved, and HIP-treated configurations with indicated build layer thicknesses. ....	80
10. Comparison of the average number of cycles to failure for the stress-relieved and HIP configurations. ....	87
11. Comparison of the average number of cycles to failure for the HIP-treated configuration with machined edges. ....	104
12. Comparison of experimental tensile results to manufacture's data. ....	107

## Nomenclature

$A$	cross-sectional area ( $\text{mm}^2$ )
Al	Aluminum
$^{\circ}\text{C}$	degrees Celsius (temperature)
F	force (kN)
$^{\circ}\text{F}$	degrees Fahrenheit
GPa	gigapascal ( $1 \times 10^9 \frac{\text{kg}}{\text{m} \cdot \text{s}^2}$ )
$k_f$	fatigue stress factor
$k_t$	stress concentration factor
kg	kilogram (mass)
kN	kilonewton (force)
ksi	kilopounds per square inch (force)
lb	pound (weight)
m	meter (length)
MPa	megapascal ( $1 \times 10^6 \frac{\text{kg}}{\text{m} \cdot \text{s}^2}$ )
nm	nanometer ( $1 \times 10^{-9}$ m)
$q$	notch sensitivity factor
$R$	stress ratio
s	seconds (time)
$S$	stress (MPa)
$S_a$	stress amplitude (MPa)

$S_e$	equivalent stress (MPa)
$S_m$	mean stress (MPa)
$S_u$	ultimate strength (MPa)
Ti	Titanium
v	Vanadium
$\alpha'$	acicular martensitic phase
$\varepsilon_f$	elongation at break (mm/mm)
$\rho$	density
$\rho_{rel}$	relative density
$\sigma$	ultimate tensile strength (MPa)
$\mu\text{m}$	micrometer ( $1 \times 10^{-6}$ m)
%	percent

## Abbreviations

3D	three dimensional
AM	additive manufacturing
ASTM	American Society for Testing and Materials
BALD	Bleed Air Leak Detect
CAD	computer aided design
CNC	computer numerical control
DoD	Department of Defense
EBM	electron beam melting
EDS	energy dispersive spectrometer
EDM	electrical discharge machining
EOS	Electro Optical Systems GmbH
HCF	high-cycle fatigue
HFW	horizontal field width
HIP	hot isostatically pressed
GE	General Electric
ISS	International Space Station
LS	laser sintering
NAMII	National Additive Manufacturing Innovation Institute
NASA	National Aeronautics and Space Administration
PPM	part property management
PPP	part property profile
S-N	stress versus number of cycles

SEM	scanning electron microscope
SLM	selective laser melted
STD	standard deviation
STEP	standard for the exchange of product model data
Ti-64	Ti-6Al-4v titanium alloy
USAF	United States Air Force
UTS	ultimate tensile strength
YS	yield strength

# INVESTIGATION OF THE HIGH-CYCLE FATIGUE LIFE OF SELECTIVE LASER MELTED AND HOT ISOSTATICALLY PRESSED TI-6AL-4V

## I. Introduction

### 1.1. Motivation for Research

Additive Manufacturing (AM) made recent headlines in September 2014 when the National Aeronautics and Space Administration (NASA) delivered a 3D-printer to the International Space Station (ISS) to perform the first-ever demonstration of 3D-printing technology from space. NASA's interest in AM is to develop the technology for on-demand manufacturing of replacement parts from onboard a spacecraft. This is done to reduce the cost and logistics footprint for providing spare parts support for the ISS and future long-range space missions [1]. While NASA's vision is still a number of years away from realization in a space-based environment, the current state of AM technology provides several manufacturing advantages and opportunities within the United States Air Force (USAF) and Department of Defense (DoD). Such technology allows for accelerated part production times, reduction of cost and waste of manufacturing complex components, and exploiting the design flexibility of topology-optimized components which are inefficiently manufactured using traditional machining methods.

While the first thing to come to mind when hearing the term '3D-printing' is often rapid prototyping with plastics, rapid growth within the AM industry in recent years has resulted in a number of processes and machines capable of processing a variety of metal alloys [2]. Available AM alloys include high strength steels, nickel, and titanium alloys [3]. With the availability of such alloys, AM presents the opportunity to manufacture structural components for use in military air and ground-based systems. Combined with

the manufacturing flexibility afforded by 3D-printers, AM allows designers to fabricate functional components directly from a Computer Aided Design (CAD) file [2]. Two significant DoD applications of AM-technology is the fabrication of topology optimized structures to reduce the weight of components as well as rapid, on-demand manufacturing of aircraft replacement parts for contingency operations, such as Air Battle Damage Repair [4-6].

Among the metal alloys capable of processing by current commercially available AM machines, Ti-6Al-4v titanium alloy (Ti-64) is widely used in both commercial and military aircraft systems. Favorable Ti-64 material properties include a high strength-to-weight ratio, corrosion resistance, and suitability for exposure to high temperatures such as turbine engine applications [7]. A DoD-sponsored report by the Institute for Defense Analyses (IDA) identified titanium alloys a likely first application area for AM technology because of its high cost and relatively difficult machining characteristics. The IDA report notes spare parts management for DoD systems is becoming increasingly complex and expensive. As weapon systems are operated well beyond their original design life, the procurement time for out-of-production replacement parts can often exceed two years to re-make with traditional forging and machining processes. To help solve the DoD spare parts issues, the IDA report points to AM as a method to produce spare parts on-demand. However, the IDA report notes there are a number of barriers and challenges to address before such parts are qualified for use on DoD systems. Barriers and challenges include testing, certification, and procurement of digital designs for the parts produced [8].

Among the challenges to qualifying AM materials for utilization in DoD systems is a thorough understanding of an AM material's mechanical properties and structural performance under dynamic loading conditions. One approach to addressing this issue is to demonstrate the mechanical properties of an AM-produced metal alloy component can meet or exceed the minimum design requirements for a traditionally manufactured component made from wrought material [9]. In the case of Ti-64 produced by an AM process known as Selective Laser Melting (SLM), and for many other metal alloys produced by SLM, the static mechanical properties such as strength and hardness are demonstrated to meet and oftentimes exceed the typical mechanical properties of the equivalent wrought material [10, 11]. However, dynamic properties, such as the expected life under cyclic fatigue loading, are not fully characterized for Ti-64. Previous SLM Ti-64 research has demonstrated the fatigue life in the high-cycle fatigue (HCF) regime is often well below the typical life expected from an equivalent wrought Ti-64 material. Reduced HCF life is troublesome for DoD aerospace applications. HCF is cited as the number one cause of failure in military turbine engines [12]. As the result of past engine and aircraft structural failures attributed to fatigue, the USAF has adopted strict standards through its Aircraft and Engine Structural Integrity Programs to develop damage-tolerant structural designs to mitigate the risk of fatigue failures [13]. A thorough understanding of the fatigue characteristics of a material is critical to achieving a damage-tolerant design.

The fatigue life of SLM Ti-64 is influenced by characteristics of the SLM process including surface roughness, anisotropy, porosity, and microstructure. Several recent studies were conducted on HCF performance of SLM Ti-64. These studies have

indicated when SLM Ti-64 specimens are tested in their as-built state without heat-treatment, fatigue life is considerably lower than typical values expected from wrought material [9, 14, 15]. However, a study by Leuders *et al.* demonstrated heat-treatment produces a marginal increase to fatigue life and Hot Isostatic Pressing (HIP) resulted in a fatigue life nearly equivalent to typical wrought material [15]. Several past studies have attributed the lower fatigue life of SLM Ti-64 to the presence of porosity and internal voids within the material [9, 15-17]. HIP is suggested as a method to reduce the internal porosity of SLM Ti-64 to achieve fatigue strengths closer to wrought Ti-64 [9, 15]. However, limited data is available on the actual impact of HIP to the fatigue life in SLM Ti-64, and specifically, the impact of HIP when the surface is un-machined. Un-machined surfaces results in a distribution of stress concentrations caused by significant surface roughness from the SLM process.

## **1.2. Research Scope**

The purpose of this research is to further investigate the fatigue life properties of SLM Ti64. Due to the large number of processing variables involved with SLM and a high degree of data scatter in experimental results published to-date, additional fatigue life data is desired. Additional data will help develop a greater understanding of the fatigue life implications from various processing parameters and post-processing treatments [9]. Existing research has assessed the SLM Ti64 fatigue life impacts of various parameters including build orientation, surface machining, heat treatment, and HIP [9, 14, 15]. The focus of the research conducted in this study is to investigate the fatigue life impact of HIP when the surface is not machined to remove the surface

roughness. This condition is representative of the direct manufacture of an aircraft replacement part to net dimensions when surface machining during post-processing is impractical or would negate the benefits of additive manufacturing.

### **1.3. Problem Statement**

The majority of previous SLM Ti-64 fatigue testing is conducted on machined test specimens with smooth surfaces as is typical of fatigue testing conducted in accordance with American Society for Testing and Materials (ASTM) testing standards. However, parts manufactured for contingency spare part production or topology optimized structures may necessitate AM fabrication directly to net tolerances without subsequent surface machining. Parts built directly to net tolerances will have considerable surface roughness caused by the SLM process. Current experimental data does not fully characterize the impacts of surface roughness on fatigue life in SLM Ti-64 specimens. Although limited available test data suggests HIP provides increased fatigue life in smooth specimens, further research is needed to characterize the effectiveness of HIP at reducing internal porosity in SLM Ti-64. In the absence of reliable analytical models to predict fatigue life in SLM Ti-64, this research serves to determine if HIP provides a measurable increase to HCF life when stress concentrations resulting from surface roughness are not addressed by surface machining or other surface improvement methods.

#### **1.4. Research Objectives**

The overarching goal of this research is to assess the impact to the HCF life of SLM Ti-64 after performing HIP on SLM Ti-64 test specimens built directly to net-dimensions without subsequent machining of the surface. To provide an assessment of the effect of HIP on the HCF life of SLM Ti64 with un-machined surfaces, research conducted in this study will support the following objectives:

1. Verify the quality of SLM Ti-64 test specimens fabricated with a commercially available machine by verifying the static tensile properties are consistent with data published by the manufacturer.
2. Collect experimental data to generate a stress-life curve for a baseline, stress-relieved SLM Ti-64 fatigue specimen fabricated directly to net dimensions.
3. Collect experimental data to generate a stress-life curve for SLM Ti-64 fatigue specimens fabricated directly to net dimensions and then processed by HIP.
4. Conduct examination of fracture surfaces to determine whether HIP influences the location of the fatigue crack initiation sites.
5. Collect experimental data to generate a stress-life curve for a second HIP-treated configuration with machined edges to assess the impact to fatigue life after removal of stair-step ridges.

To satisfy the test objectives, experimental test data was collected on a total of four material configurations consisting of as-built, stress-relieved, HIP-treated, and HIP-treated with machined edges. All test specimens were manufactured with an EOSINT M 280 machine operated by a commercial vendor. The as-built configuration consists of

samples built directly to net-dimensions and not subjected to any form of heat treatment process or machining during post-processing beyond separation from the build plate and removal of any necessary support material from the build process. The stress-relieved configuration is the same as the as-built configuration with the addition of furnace heat-treatment at 650 °C for 4 hours in an argon atmosphere. This heat-treatment is consistent with the stress relief process outlined in the manufacturer's material data sheet. The HIP-treated configuration is the same as the as-built configuration with the addition of HIP performed at 899 °C for 2 hours at a relative pressure of 101.7 MPa. The HIP-treated with machined edges configuration is the same as the HIP-treated configuration with the narrow edges of the test specimens machined on both sides to remove stair-step ridges and produce matching surface finishes on the edges.

### **1.5. Assumptions and Limitations**

This research provides experimental test data on the HCF properties of SLM Ti-64. Due to the limited nature of the testing within time, schedule, and resource constraints, results are intended to assess the demonstrated performance of commercially-fabricated SLM Ti-64 test specimens in the HCF regime by comparison of stress-life curves for stress-relieved and HIP configurations. The accomplished testing reflects the overall condition of the test specimens in their as-fabricated state and does not attempt to quantify specific stress concentration factors resulting from surface roughness, internal voids, and other features resulting from the SLM fabrication process. All test specimens have approximately equivalent dimensions and the distribution of surface roughness features is assumed approximately equivalent allowing for a direct comparison of fatigue life results between the stress-relieved and HIP configurations. With the exception of

selecting a 30  $\mu\text{m}$  or 60  $\mu\text{m}$  build layer thickness, the processing parameters used during SLM fabrication were pre-set by the machine manufacturer; therefore, the impacts of specific processing parameters are not assessed. Likewise, all specimens were built in the same orientation precluding an assessment on the impact of build orientation.

## **II. Background Information and Previous Research**

### **2.1. Additive Manufacturing Overview**

Additive manufacturing is a method of generating solid, 3D parts using a layer-by-layer building approach [2]. AM is one of three categories of manufacturing technologies for direct production of 3D parts from a computer generated file (i.e. CAD). The layer-by-layer additive process is in contrast to subtractive CAD-to-3D part processes including machining technologies such as computer numerical control (CNC) machining, electrical discharge machining (EDM), and water jet cutting. Additive and subtractive technologies can also be combined into hybrid CAD-to-3D part processes. Collectively, these 3D fabrication categories for the direct production of parts from computer-generated files form the basis for what commonly referred to as Direct Digital Manufacturing [18].

The origins of AM trace to the early 1980s when several patents were filed in Japan, France, and the United States for concepts describing the fabrication of 3D objects using a layer-by-layer approach [2]. AM technologies were first developed to provide a method for rapid and cost-efficient production of 3D prototypes and scaled mock-ups to support the engineering design process [19]. Over the past three decades, a number of AM machines and processes were developed. These various processes permit additive fabrication with over 100 different materials including various plastics, metals, ceramics, and bioengineered organic tissues [19, 20]. As AM processes and materials have matured, the industry has expanded beyond its rapid prototyping origins and into the realm of manufacturing 3D parts intended for end-use applications [2].

Although there are several different methods of classifying AM processes using various terminology oftentimes inconsistent throughout the AM industry, ASTM International has formed a dedicated committee on AM. A primary function of this committee is to generate AM industry standards among the many international stakeholders [2, 21]. The standardized process categories and definitions from ASTM F2792-12a, Standard Terminology for Additive Manufacturing Technologies, are shown in Table 1. In accordance with the process definitions in Table 1, SLM Ti64, the exclusive focus of this research, falls within the powder bed fusion process category.

*Table 1. AM process categories from ASTM F2792-12a.*

<b>Process</b>	<b>Description</b>
<b>binder jetting</b>	process in which a liquid bonding agent is selectively deposited to join powder materials
<b>directed energy deposition</b>	process in which focused thermal energy is used to fuse materials by melting as they are deposited
<b>material extrusion</b>	process in which material is selectively dispensed through a nozzle or orifice.
<b>material jetting</b>	process in which droplets of build material are selectively deposited
<b>powder bed fusion</b>	process in which thermal energy selectively fuses regions of a powder bed
<b>sheet lamination</b>	process in which sheets of material are bonded to form an object
<b>vat photopolymerization</b>	process in which liquid photopolymer in a vat is selectively cured by light-activated polymerization

AM affords several advantages over traditional manufacturing processes. These advantages fall within four major areas: speed of production, minimization of waste, design flexibility, and reduction of logistics footprint. For relatively small-scale production quantities, AM has the potential to significantly reduce the associated

manufacturing lead time. With the production of parts directly from a CAD file, AM processes eliminate the need to fabricate or acquire specialized tooling and fixtures. In some instances, parts are printed as a single assembly reducing the complexity and eliminating time requirements for the assembly of individually manufactured parts. One example of this is the production of the fuel nozzle for General Electric's (GE) next-generation Leading Edge Aviation Propulsion (LEAP) turbofan engine. The original design for the LEAP fuel nozzle consisted of 20 individual parts welded together. Using an SLM 3D-printing process, GE was able to consolidate the design into a single part reportedly 25% lighter and five times stronger than the original design. GE reports the new design manufactured by SLM has a significantly reduced manufacturing lead time by eliminating the need to manufacture and assemble individual parts [22].

The second area of advantage of AM is minimization of waste. In contrast to a subtractive manufacturing process which cuts away on a single block of material to obtain the final geometry of a part, AM builds the part layer-by-layer either directly to net dimensions or slightly oversized for machining of the final tolerances. Depending on the particular design of a part, a purely subtractive process often results in a significant amount of waste. For example, the Bleed Air Leak Detect (BALD) bracket attached to the side of the engine on the F-35 Joint Strike Fighter is traditionally machined from a block of wrought Ti-64 material. Due to the bracket's thin cross section, subtractive CNC machining results in a 33 to 1 waste material ratio ("buy-to-fly" ratio). In a study by Dehoff *et al.*, AM production of the BALD bracket was demonstrated using an Electron Beam Melting (EBM) process. Use of EBM achieved a near 1:1 buy-to-fly ratio

with mechanical properties exceeding the minimum requirements for non-flight-critical hardware [23].

Design flexibility is perhaps the most appealing advantage of AM processes. Since AM parts are constructed layer-by-layer directly from a CAD file, AM has the ability to seamlessly produce complex geometries in topology optimized structures otherwise difficult or impossible to produce using subtractive processes [2, 20]. When employing topology optimization on a part or structure fabricated using traditional manufacturing processes, the optimization is constrained by the cost and feasibility of producing the more intricate geometry [24]. AM effectively eliminates such constraints. In a study by Tomlin and Meyer, production of a topology optimized nacelle hinge bracket for the Airbus A320 was demonstrated using AM. The optimized design reduced the weight of the bracket from 918 grams to 326 grams, a weight reduction of 64%, while maintaining the required structural properties [25]. Other complex geometries achievable through AM production include porous materials for medical implants replicating the mechanical properties of human bone, and cellular lattice structures for use as rigid, light-weight materials for aerospace and other weight-critical applications [2, 26].

The final area of advantage for AM is reduction of the logistics footprint for parts production. There are two ways in which this is achieved by AM: on-site manufacturing and/or on-demand manufacturing. Since AM provides the ability to manufacture a wide variety of parts with a single machine and without the need for retooling, AM is generally more suitable than traditional manufacturing methods for the manufacture of parts on-site and on-demand. This flexibility yields significant efficiencies in supply chain management by reducing spare part requirements, warehousing needs, and transportation

requirements [27, 28]. For the USAF, spare parts supply for deployed aircraft is a significant logistics challenge. To support deployment packages, planners must forecast spare part requirements and develop comprehensive spares kits. These large kits require transportation and storage at the forward deployed location. Part forecasts are seldom one-hundred percent accurate resulting in needed parts not included in the kit and surplus parts not required [27]. When the need arises to obtain a spare part not readily available from the supply system, remaking the part could take up to two years in some instances utilizing traditional manufacturing methods [8]. With the flexibility to manufacture parts on-site and on-demand, AM is identified as a potential solution to the spare parts challenge faced by the USAF and other DoD organizations [8, 27].

While the advantages of AM make it a very attractive process for a wide variety of applications, there are a number of limitations and challenges. While each individual AM process has its own unique set of limitations, common challenges of AM for the production of end-use items include the size limitations for parts producible within the build volume of existing machines, anisotropy in material properties based on build orientation, requirements for support structure for overhanging surfaces during the build, roughness of the as-built surfaces, internal voids or defects, and relatively slow build speeds [2, 9, 29-31]. Many of the surface quality issues, such as “stair-stepping” from the layered build process, are overcome by machining and polishing the surface to final tolerances. However, these additional processing steps diminish the “tool-less” advantage of AM and are not feasible for parts with intricate geometries [24].

In addition to the design limitations and considerations associated with AM processes, a major challenge to widespread use of AM to produce end-use products and

flyable prototypes in aerospace industry is the qualification of AM parts to meet stringent quality and reliability standards for airworthiness [8, 32]. Although AM has existed since the 1980s as a rapid prototyping tool, transition to the production of usable end-items is still in the early technical stages [27]. Qualification for aerospace use is a complex issue involving compliance with existing manufacturing standards and creation of new standards specific to AM materials and processes. Established industry standards are required to ensure products conform to material performance, processing, and quality requirements [33]. Material properties require full characterization, documentation, and understanding in terms of the effects of AM processes on microstructure, residual stresses, and other thermally-induced effects [27]. Additionally, adequate process controls and monitoring are required to ensure consistent, reliable, and repeatable production [27].

Until recently, material and process specifications for AM did not exist. To address the need for AM industry standards, ASTM International commissioned Committee F42 on Additive Manufacturing Technologies in 2009 [21]. Technical standards are currently in development by four technical subcommittees. As of 2014, these subcommittees have published standards in the areas of materials and processes, terminology, design and data formats, and test methods [33]. Additionally, in response to a 2012 presidential call for the establishment of national centers to accelerate the development of cutting-edge manufacturing technologies, a consortium of government, academic, and industry partners was established as the National Additive Manufacturing Innovation Institute (NAMII), rebranded in 2013 as America Makes [34]. As part of their mission, America Makes has established an open exchange of AM information and research, facilitates

development and deployment of AM technologies, and supports education and training of the AM workforce [35].

## **2.2. Overview of Powder Bed Fusion Processes**

There are currently two primary powder bed fusion technologies commercialized and marketed for production of parts with metal alloys: electron-beam melting and laser sintering (LS) [3, 10, 36]. The primary distinction between EBM and LS is the type of energy source providing the thermal energy to fuse the powdered feedstock material. EBM heats selected areas of a powder bed by the transfer of kinetic energy from an incoming beam of electrons. In an LS process, thermal energy is created from the absorption of photons from the laser energy source [2]. Both EBM and LS processes are capable of processing a variety of metal alloys including steel, aluminum, titanium, nickel, and many others [2, 3, 37]. When processing metals, both the EBM and LS methods provide full melting of the powder particles during the fusion process. Since the term “sintering” is most often defined as fusion between particles in their solid state at high temperatures without full melting, LS of metal alloys is not an accurate description of the process since full melting is occurring [2]. Although the terms Laser Sintering, Selective Laser Sintering, and Direct Metal Laser Sintering (DMLS) are commonly used throughout literature as synonymous terms to describe laser-based powder bed fusion processes, the term Selective Laser Melting is used in this work as a more accurate description of the process. However, the term DMLS is used when referencing the specific SLM process proprietary to Electro Optical Systems (EOS) GmbH in accordance with standard industry terminology defined in ASTM F2792-12a [38].

EBM and SLM processes share many of the same basic operating principles. Powdered metal is first deposited by a powder feedstock handling system in a thin layer spread across a solid substrate plate. An energy source is then directed by a scanning system over the desired area of the powder bed to provide the thermal energy to melt the powder particles and fuse them together. The beam of energy is scanned over the entire 2-dimensional slice of the part derived from the 3D CAD file. After each layer, the substrate plate is lowered by a distance equal to the desired layer thickness and then the next layer of powder is spread across the surface. The process continues until the entire 3D part is fabricated layer by layer [2, 3, 37, 39]. However, due to differences in the energy source and the method used to control the energy beam, EBM and SLM processes have their own advantages and disadvantages in terms of production efficiency and part quality. As described in Gibson, Rosen, and Stucker, the electron beam in EBM is comprised of negatively charged electrons. This allows magnetic focusing and controlling of the beam by magnetic coils. Since magnetic coils have a nearly instantaneous response, the track of the electron beam is controlled very quickly. Laser beams, on the other hand, are controlled optically by mirrors operated by galvanometer motors. The scan speed of the laser beam is therefore limited by the mechanical response of the mirrors and motors [2]. Combined with a more efficient delivery of high-energy beams compared to lasers, the faster scan speed afforded by EBM generally allows for greater build speeds compared to SLM [2, 36]. Additionally, the build chamber during EBM is held at comparatively higher temperatures than SLM processes. The elevated temperature during the build minimizes thermally-induced stresses which results in parts generally not requiring post-processing stress relief [9, 36, 40].

Despite having slower build speed, SLM offers several advantages over EBM in terms of feature resolution, tolerances, and surface finish [2, 36, 40]. SLM generally utilizes smaller layer thicknesses on the order of 20-60  $\mu\text{m}$  versus the 70-100  $\mu\text{m}$  layers typical of EBM [10, 36]. SLM also typically utilizes smaller particle sizes in the raw feedstock powder. As a result of the smaller layer thickness, particle size, and the slower scanning strategy employed by typical SLM processes, SLM is capable of achieving higher build tolerances, replication of finer features, and reduced surface roughness compared to EBM [10, 36, 39, 40]. Data reported in Frazier indicates the average surface roughness of components produced by SLM is approximately one half of those components produced by EBM with an average surface roughness for vertical surfaces (with respect to the build direction) ranging from 7.8 to 8.4  $\mu\text{m}$  for SLM and an average of 15.1  $\mu\text{m}$  for EBM [39]. Although the specific material properties for both SLM and EBM are highly dependent on specific processing parameters and post-processing heat treatment, a study by Koike *et al.* found the mechanical properties for Ti-64 produced by SLM and EBM are generally comparable to wrought Ti-64. Furthermore, SLM Ti-64 was found to have slightly higher strengths than EBM Ti-64 [10]. While the choice of specific AM process is driven by the desired objectives and end-use of an intended component, based on the improved surface finish and ability to achieve higher tolerances, SLM is potentially better suited when compared to EBM for the direct manufacturer of components to net-tolerances when surface machining is not performed.

### **2.3. Material Properties and Microstructure of SLM Ti-64**

As described in Gibson, Rosen, and Stucker, the machine processing parameters for SLM are grouped into four categories: 1) laser-related, 2) scan-related, 3) powder-related, and 4) temperature-related. Laser-related parameters include the laser power, spot size, pulse duration, and pulse frequency. Scan-related parameters include scan speed, scan spacing, and scan pattern. Powder-related parameters include particle shape, size, distribution, powder bed density, layer thickness, and elemental composition. Finally, temperature-related parameters include the powder bed temperature, powder feeder temperature, temperature uniformity, and heat dissipation characteristics of the build assembly [2]. The effects of individual processing parameters on SLM Ti-64 material properties is not completely understood and is an active research area [16, 41-45].

Processing parameters are adjusted and optimized to perform tradeoffs among different design goals such as dimensional accuracy, mechanical strength, processing time, surface roughness, and production cost [46]. As discussed in greater detail in section 3.3, the specimens for this study were manufactured using pre-defined processing parameters optimized by the machine manufacturer to achieve a balance between part quality and build time. The EOSINT M 280 machine used to manufacture test specimens for this study utilizes a proprietary process with limited user control over the specific processing variables. Material properties are therefore generally consistent between each build and only influenced by the user-selected layer thickness and the build orientation of the parts.

During the SLM process, large temperature gradients occur as the result of rapid melting and cooling. Rapid melting occurs within the melt pool under the laser spot followed by rapid cooling as the melt pool transforms to solid state after the laser passes

by. The rate of cooling and the geometry of the melt pool influence the grain growth in the resulting microstructure [43]. A previous study by Thijs *et al.* on the microstructure of SLM Ti-64 reports the material exhibits a martensitic microstructure dominated by an acicular martensitic phase ( $\alpha'$ ) [45]. Data from a previous study by Edwards and Ramulu shows the grain structure for as-built SLM Ti-64 has lamellar colonies of  $\alpha'$  within long, thin, columnar-shaped prior-beta grains oriented perpendicular to the build direction [9]. Data published by Simonelli reported prior-beta grain boundary sizes ranging from 1-3 mm in length and an average width of 103  $\mu\text{m}$  [29].

Two commonly noted issues with SLM Ti-64 are residual stresses and porosity. As discussed in Kruth *et al.*, residual stresses are the result of the high temperature gradients caused by the localized heating and cooling of the melt pool. Repeated thermal expansion and contraction experienced during the build process generates significant residual stresses in the material. Residual stresses can result in distortion of the manufactured part as well as decreases in strength [43]. Simonelli reported several long, slender tensile specimens manufactured in a horizontal orientation experienced significant curling as the result of residual stresses in the material [29]. During fatigue specimen preparation by Edwards and Ramulu, specimens built in a horizontal orientation experienced curling after machining on one side as a result of the redistribution of residual stresses [9]. To combat residual stresses, it is recommended SLM Ti-64 components contain sufficient material support structures during fabrication to maintain the geometry of the part during the build followed by heat-treatment during post-processing to provide stress relief [2]. A study by Leuders *et al.* reported surface tensile residual stresses in as-built samples ranged from 90 MPa to as high as 775 MPa.

Post-processing stress relief at 800 °C effectively eliminated the surface residual stresses with measurements ranging from -5 to +10 MPa [15].

Although SLM reportedly produces fully-dense components with densities approaching 100%, micro-porosity was observed in several past SLM Ti-64 studies [9, 15, 42, 47]. Pores in SLM Ti-64 are caused by several process-induced factors such as impurities in the powder and gas entrapment from the argon atmosphere in the build chamber [15]. As described in Sallica-Leva *et al.*, porosity can have a detrimental effect on the strength of a material [48]. A theoretical relationship between the mechanical properties of a material and its relative porosity is expressed by the Ashby and Gibson model shown in equation (1).

$$\sigma_{\max} = \sigma_{\max 0} \times \rho_{rel}^{\frac{3}{2}} \quad (1)$$

In equation (1),  $\sigma_{\max}$  is the effective ultimate tensile strength (UTS) of the porous material with respect to the UTS of the fully dense bulk material,  $\sigma_{\max 0}$ , and relative density of the material,  $\rho_{rel}$ . According to the Ashby and Gibson model, the strength of a material decreases by a factor of the relative density raised to the  $\frac{3}{2}$  power. This model assumes porosity is randomly distributed and the pores have a smooth, spherical shape. A study by Leuders *et al.* reported a relative density for SLM Ti-64 of 99.77% [15]. Even when the relative density is rounded down to 99.5%, the Ashby and Gibson model predicts a decrease in UTS by only 0.75%. Porosity is therefore likely to have a negligible impact on the strength properties of SLM Ti-64. However, as discussed in greater detail in section 2.4, porosity is potentially a significant contributing factor to reduced fatigue performance.

Due to the large number of processing parameters influencing the microstructure and material properties of Ti-64, reported mechanical properties in previous SLM Ti-64 studies vary due to differences in the machine, processing parameters, and post-processing heat treatments. However, a sampling of SLM Ti-64 data published in literature indicates as-built SLM Ti-64 tensile strength properties generally meet or exceed the typical values for wrought Ti-64 by an order of 1-5% [9, 10, 14, 29, 36, 47]. Previous studies also show as-built SLM Ti-64 exhibits a brittle behavior with a study by Leuders *et al.* reporting an elongation at break ( $\epsilon_f$ ) of just 1.6% for as-built specimens manufactured with an SLM 250 machine by SLM Solutions GmbH. Post-processing heat treatment at 800 °C increased  $\epsilon_f$  to 5% and heat treatment at 1050 °C increased  $\epsilon_f$  to 11.6% [15]. Additionally, previous studies indicate SLM Ti-64 exhibits anisotropy based on the build direction. A study by Simonelli on the effect of build orientation on the mechanical properties of SLM Ti-64 reported a UTS of 1199 MPa and yield strength (YS) of 1075 MPa for specimens built in the horizontal orientation. For specimens built in the vertical orientation, UTS decreased by 6.8% to 1117 MPa and YS decreased 10.0% to 967 MPa. However, the data from Simonelli shows heat treatment at 730 °C reduced the amount of variation in strength between build directions. For heat-treated specimens built in the horizontal orientation, the UTS was 1065 MPa and the YS was 974 MPa. In the vertical orientation, UTS decreased only 1.2% to 1052 MPa and YS decreased 3.8% to 937 MPa. Based on metallographic examination, Simonelli states the likely cause of the anisotropy is the directionality of the prior-beta grain boundaries which have a tendency to align with the layer-wise build direction. Heat-treatment altered the phase

composition of the microstructure to a more balanced ratio of alpha and beta phase which both increased ductility and reduced the degree of anisotropy [29].

To provide an expected baseline of material properties for the SLM Ti-64 specimens manufactured in this study, typical values based on data published by the manufacturer in a material data sheet are utilized. This provides a more reliable baseline comparison since the data published by EOS in their Ti-64 data sheet is based on the same machine, powder, and processing parameters used to manufacture specimens for this study. EOS indicates the data in the material data sheet is valid for both the EOSINT M 270 and M 280 using any of the pre-defined Ti-64 parameter sets. The data sheet does not distinguish between the 30  $\mu\text{m}$  and 60  $\mu\text{m}$  layer thickness available in the EOS Ti-64 parameter sets on the EOSINT M 280 machine. The data sheet does however publish a separate set of values based on horizontal or vertical build direction for both as-built and stress-relieved material heat-treated at 800 °C for 4 hours in an argon atmosphere. Table 2 shows a comparison of the EOS data sheet values with the minimum values required for wrought, annealed Ti-64 in aerospace applications governed by AMS 4911 and Ti-64 produced by powder bed fusion governed by ASTM F2924. Additionally, data is shown from a previous study by Rafi *et al.* for as-built specimens manufactured in the horizontal direction using an EOSINT M 270 with 30  $\mu\text{m}$  layer thicknesses.

**Table 2. Comparison of typical EOS DMLS Ti-64 mechanical properties with minimum industry standard values for wrought and powder bed fusion material.**

	AMS 4911 Wrought Annealed	ASTM F2924 Powder Bed Fusion	EOS As-built	EOS Stress-Relieved	Rafi <i>et al.</i> As-Built
<b>UTS ± STD (MPa)</b>	920 (min)	895 (min)	1230 ± 50 (typ)	1050 ± 20 (typ) 930 (min)	1269 ± 9
<b>YS ± STD (MPa)</b>	866 (min)	825 (min)	1060 ± 50 (typ)	1000 ± 20 (typ) 860 (min)	1195±19
<b>ε<sub>f</sub> (%)</b>	10 (min)	10 (min)	10 ± 2 (typ)	10 (min)	5 ± 0.5
<b>E ± STD (GPa)</b>	NA	NA	110 ± 10 (typ)	116 ± 10 (typ)	Not Reported

From the data in Table 2, it is seen typical material properties reported by EOS exceed the ASTM F2924 minimum values required for Ti-64 components manufactured by powder bed fusion as well as the minimum values required by AMS 4911 for wrought and annealed material used in aerospace applications. Of note, the strength values reported by Rafi *et al.* for specimens manufactured with an EOSINT M 270 exceed the typical average values published by EOS by 17% for UTS and 16% for YS. However, the elongation at break noted by Rafi *et al.* was only one-half the average of the typical value reported by EOS.

#### **2.4. Hot Isostatic Pressing**

As defined by ASTM, HIP is the process of subjecting a powder, compact, or sintered object to an elevated temperature and pressure equal from every direction. The combined heat and pressure results in densification of the material through the actions of diffusion and creep [49]. As described in Akinson and Davies, HIP is widely used for a variety of applications including interfacial bonding, casting of solid components by the

consolidation of powders, and the densification of pre-cast or pre-sintered components [50]. While densification by HIP is traditionally applied to castings, the application of HIP for purposes of this study is the densification of SLM material by reduction of micro-porosity and other voids within the microstructure caused by SLM. When sufficient heat and temperature is applied to the surface of a solid in all directions, the solubility of gas entrapped within the microstructure is increased. Under the applied heat and pressure, the gases diffuse through the grain boundaries to reach the surface. The surfaces of the pores are then forced together at which point bonding results in complete closure of the pores. The combined effects of porosity removal and preferential grain growth from the elevated temperature generally improve the microstructure and mechanical properties of the material. Additionally, HIP improves the consistency of the microstructure throughout the various regions of the material which reduces the amount of local variation or scatter in material properties [50].

The primary appeal of HIP with respect to SLM Ti-64 is the potential to improve high-cycle fatigue life by reducing or eliminating the stress risers caused by internal pores and defects [9]. At least two previous studies have identified the presence of internal porosity as a likely contributor of reduced fatigue life in SLM Ti-64 [9, 15]. Leuders *et al.* notes the build chamber during SLM is filled with an argon protective atmosphere. As a result, argon gas is entrapped within pores making complete closure of the pores difficult to during HIP. However, experimental data in Leuders *et al.* demonstrated a measurable reduction in porosity in HIP specimens by reducing pores with diameters up to 50  $\mu\text{m}$  as measured in as-built specimens to below the detection limit of 22  $\mu\text{m}$  after HIP.

## 2.5. High-Cycle Fatigue

Fatigue occurs when damage accumulates in a material due to cyclic loading at stresses below the ultimate strength of the material [7]. With each cycle, the accumulating damage degrades the microstructure. If the applied stresses are sufficient, a crack will initiate and propagate through the material under the continued cyclic loading. Once the crack reaches a critical length such the remaining material is unable to support the applied load, complete failure of the material occurs [51]. When the stress level of the cyclic loading is above the yield stress of the material, the resulting strains have a non-recoverable plastic component. Under these conditions, failure of the material occurs within a relatively low number of load cycles. This failure regime is known as low-cycle fatigue and typically occurs within  $10^4$  cycles. In contrast, HCF typically occurs beyond  $10^4$  cycles at stress levels well below the yield strength in the elastic region of the material [13, 51].

The fatigue life of a material in the HCF regime is often characterized in terms of the relationship between the applied stress level and the number of cycles until failure. When the stress versus cycles to failure data is shown graphically, the resulting figure is known as a stress-life (S-N) curve [52]. S-N curves are commonly referred to as Wöhler diagrams in honor of the German railway engineer, August Wöhler, who pioneered the first systematic fatigue investigations on railway axles between 1852 and 1870 [53]. Depending on the type of material and specific loading conditions, the shape exhibited by the S-N curve may vary as shown in Figure 1.

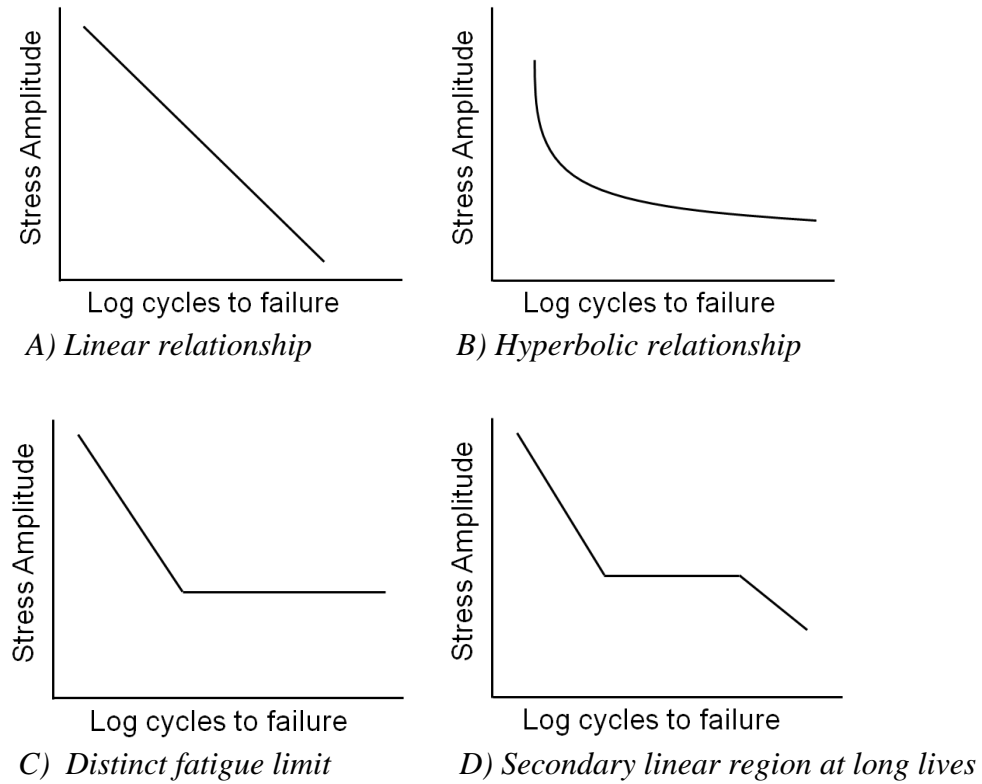


**Figure 1. Sample of possible stress-life fatigue behaviors.**

When constructing S-N curves, the stress amplitude is typically the independent variable and shown on the vertical axis in either a normal or logarithmic scale. The number of cycles to failure is the dependent variable shown on the horizontal axis in a logarithmic scale [52]. In Figure 1, several possible shapes of the S-N curve are shown. Figure 1A depicts a material with a purely linear relationship between the applied stress level and the expected number of cycles to failure. Figure 1B depicts a material with a hyperbolic relationship gradually approaching a horizontal asymptote. This asymptote corresponds to an endurance fatigue limit which represents the theoretical stress level under which a material will never fail or survive to a prescribed maximum number of cycles treated as infinite life. Some materials exhibit a linear relationship in the finite-life

region at stress levels above the fatigue limit as shown in Figure 1C. This linear relationship can occur when the data is presented in a linear-log scale or may become linear when presented in a log-log scale [54]. In Figure 1C, the linear finite-life region is determined primarily by fractures originating at the material's surface. At long lives, the failures in some materials transitions to subsurface initiation and results in a second distinct linear region as shown in Figure 1D [13]. Based on S-N data published in the Metallic Materials Properties Development and Standardization (MMPDS), solution-treated and aged (wrought) Ti-64 exhibits an approximately linear behavior in the finite-life region and then approaches a horizontal asymptote at longer lives consistent with the behavior depicted in Figure 1C [55].

A commonly used method for determining the S-N curve experimentally is by load-control axial fatigue testing. Under typical load-control testing, each test specimen is subjected to a constant-amplitude cyclic load at an established frequency. The cyclic loading is described by the shape of the waveform, the stress amplitude, the mean stress level, and the ratio of minimum to maximum stress [53]. For load-control fatigue testing conducted in accordance with ASTM E466-07, the waveform is typically sinusoidal [56]. The stress amplitude, mean stress, and stress ratio are defined by the relationships in equations (2-4) [53] .

$$S_a = \frac{S_{\max} - S_{\min}}{2} \quad (2)$$

$$S_m = \frac{S_{\max} + S_{\min}}{2} \quad (3)$$

$$R = \frac{S_{\min}}{S_{\max}} \quad (4)$$

In equations (2-4),  $S_a$  is the stress amplitude,  $S_{max}$  is the maximum stress,  $S_{min}$  is the minimum stress,  $S_m$  is the mean stress value, and  $R$  is the ratio of minimum to maximum stress. Full reversal of the stress amplitude for a mean stress of zero is assigned a stress ratio of  $R = -1$  [53]. To generate an experimental S-N curve, testing is accomplished on a series of test samples where each sample is tested at a selected maximum stress level and a prescribed stress ratio. Each specimen is then subjected to a continuous cyclic loading condition until the specimen either fails or survives until a pre-determined number of cycles defined as the test run-out. The experimental test data is then plotted in terms of  $S_{max}$  and the corresponding number of applied cycles at which failure of the specimen occurred.

HCF failure of a material is influenced by a number of factors including mean stress, surface finish, surface notches, residual stresses, internal voids or defects, and environmental factors such as temperature [13, 51, 53]. As defined in equation (3), mean stress has a significant impact on the fatigue life of a material. A positive, or tensile, mean stress provides an additional crack-opening force on the specimen while a negative, or compressive, mean stress produces a crack-closing force which slows crack propagation [53]. Since mean stress is a controllable factor during testing, S-N results are segregated by the value of  $R$  during testing. The S-N curves for various  $R$  values are either displayed as separate curves on a single figure or resolved into a single equivalent stress model representing a fully reversed value of  $R = -1$  [55]. Several empirical models of varying complexity have been developed to relate mean stress to equivalent stress. A simplified model known as the Goodman relationship is shown in equation (5) where the equivalent stress ( $S_e$ ) is defined in terms of the stress amplitude ( $S_a$ ), mean

stress ( $S_m$ ), and ultimate strength ( $S_u$ ) of the material [53]. A higher fidelity equivalent stress is determined with other empirical models when sufficient experimental S-N data is available at various  $R$ -values to estimate model parameters.

$$S_e = \frac{S_a}{1 - \frac{S_m}{S_u}} \quad (5)$$

Surface roughness, surface notches, and internal voids or defects act as stress concentration factors amplifying the value of localized stresses experienced within the material under the presence of a nominally applied load [13, 53]. The stress concentration factor,  $k_t$ , is defined in Nichols as the ratio between the peak stress at a notch root to the average, or nominal, stress over the net cross section [13]. In other words, the true maximum stress experienced by the small localized region at the tip of a notch or defect is equal to the applied nominal stress at the cross section multiplied by  $k_t$ . However, for a material subjected to cyclic loading, the reduction in fatigue strength from notches and defects does not always directly correspond to a multiplicity of  $k_t$ . Instead, the fatigue strength is reduced by a factor defined as  $k_f$  equal to the ratio between the un-notched (smooth) fatigue limit and the resulting fatigue limit of the notched material. In general, the value of  $k_f$  is less than  $k_t$ . According to the Lee and Taylor [53], this occurs for two reasons. The first is the occurrence of cyclic yielding at the notch root which reduces the effective stress concentration factor under fatigue. The second reason is based on the theory of stress field intensity which suggests the fatigue strength of a notched material is determined by the average stress in a localized damage zone as opposed to the maximum value of the peak stress. Although many empirical models of

varying complexity exist to predict the relationship between  $k_f$  and  $k_t$ , in general,  $k_f$  and  $k_t$  are related by a factor  $q$  as shown in equation (6).

$$k_f = 1 + q(k_t - 1) \quad (6)$$

In equation (6), the factor  $q$  is known as the notch sensitivity factor and is a function of the notch or defect geometry and the properties of the material's microstructure [13, 53]. The significance of equation (6) suggests it is possible to reduce the value of  $k_f$  to obtain an increase in fatigue strength by reducing the notch sensitivity of a material. A reduction in notch sensitivity can be obtained through changes in the microstructure, such as those resulting from heat-treatment processes, without necessarily decreasing the geometrical stress concentration factor  $k_t$ .

## 2.6. Previous Ti-6Al-4v Fatigue Life Research

A considerable amount of previous research is published on SLM Ti-64. Among the published research, several studies have addressed HCF in SLM Ti-64 with experimental data. These studies are published in journal articles by Edwards and Ramulu [9], Gong *et al.* [31], Thöne *et al.* [17], Rafi *et al.* [36], Van Hooreweder *et al.* [47], and a doctoral dissertation by Marco Simonelli on the microstructure evolution and mechanical properties of SLM Ti-64 [16]. Each study utilized various SLM machines, both commercial and non-commercial, to study various test article configurations of SLM Ti-64. A summary of these previous studies and their respective test specimen configurations is shown in Table 3. The bottom three rows in Table 3 indicate specific design variables controlled in an attempt to assess the impact of build orientation, internal defects, and surface notches on HCF. As seen in Table 3, the present study will address a

gap in existing published research to provide HCF data on the effect of HIP in test articles built directly to net-tolerances.

**Table 3. Summary of configurations in previous SLM Ti-64 fatigue studies.**

	Edwards & Ramulu	Gong et al	Thone et al	Rafi et al	Van Hooreweder et al	Simonelli	CURRENT STUDY
Direct Net-Shape	X	X			X		X
Machined Surface	X		X	X		X	
Furnace Heat-Treat		X	X	UNK	X	X	X
HIP			X				X
Designed Internal Defects		X					
Multiple Build Orientations	X						
Designed Surface Notch					X		

The study by Edwards and Ramulu addressed the effects of surface roughness and build orientation on the HCF of SLM Ti-64 specimens [9]. Test articles in this study did not receive any form of post-processing stress relief or heat-treatment to comply with the researchers’ stated goal of minimizing production costs and carbon emissions. Test specimens were fabricated using an SLM 250 machine manufactured by MTT Technologies Group. The machine was equipped with a 200 watt laser and specimens were manufactured with a 50 µm layer thickness. Flat, dog-bone shaped test specimens were built in three different build orientations including vertical, x-direction horizontal, and y-direction horizontal. Half of the specimens for each build orientation were tested as-built and the other half were machined and polished on all sides to a surface finish of 2.5 µm or better. HCF testing was conducted at room temperature at 20 Hz and  $R = -0.2$ . Based on S-N curves, Edwards and Ramulu concluded the fatigue life of SLM Ti-64 samples was over 75% lower than typical wrought material due to the effects of

porosity and residual stresses in the SLM material. The researchers also concluded machining the surfaces had no apparent benefit to increasing fatigue life based on their experimental data. Fatigue failures in this study were shown to have initiated from internal voids and porosity. Additionally, the experimental data shows an apparent difference in the S-N curves based on build direction. Specimens manufactured in the x-direction performed the highest with a maximum stress of 240 MPa to achieve a target design life of 200,000 cycles. Specimens manufactured in the z-direction (vertical) performed the lowest with a maximum stress of 100 MPa for a target life of 200,000 cycles. Edwards and Ramulu suggest fatigue life is improved by post-processing heat-treatment to relieve residual stresses and HIP to decrease porosity [9].

The study by Gong *et al.* addressed the effects of internal defects on the HCF of SLM Ti-64 on un-machined test specimens [31]. Specimens were manufactured using an EOSINT M 270 machine with a 200 watt laser and a layer thickness of 30  $\mu\text{m}$ . Specimens were cylindrical shaped and built in the vertical direction. To assess the impact of internal defects, some specimens were designed with either a cylindrical shaped void with 0.5 mm diameter and height of 0.4 mm or a double-conical void measuring 0.05 mm diameter and 0.8 mm total height located in the geometric center of the reduced-area test section. All specimens were stress-relieved at 650  $^{\circ}\text{C}$  for 4 hours in an argon atmosphere. Fatigue testing was conducted at room temperature at 50 Hz and  $R = 0.1$ . Results demonstrated SLM Ti-64 specimens built directly to net tolerances and without designed defects have a mean fatigue strength of approximately 500 MPa with no reported failures below this stress level at a test run-out of  $10^7$  cycles. The presence of the cylindrical or double-conical designed defect greatly increased the scatter of the

fatigue data results and reduced the mean fatigue life to approximately 350 MPa. For specimens without the designed defects, all fatigue fractures initiated from the surface. Gong *et al.* concluded although designed defects show a drastic reduction in the fatigue life of SLM Ti-64, further study is needed to characterize the microstructure and surface morphology to better understand the specific effects of the defects [31].

The study by Thöne *et al.* addressed the effect on fatigue life by various furnace heat-treatments and HIP [17]. The results of this study were first published in a journal article by Thöne *et al.* followed by a second journal article by Leuders *et al.* [15]. Specimens were fabricated using an SLM 250 HL manufactured by SLM Solutions GmbH equipped with a 400 watt laser. Cylindrical shaped fatigue test specimens were built in the vertical direction with a layer thickness of 30  $\mu\text{m}$  and then machined to final tolerances. A total of four configurations were tested for fatigue: 1) as-built (no heat-treatment, 2) heat-treated at 800 °C for 2 hours in argon atmosphere, 3) heat-treated at 1050 °C for 2 hours in a vacuum furnace, and 4) HIP-treated at 920 °C for 2 hours at 1000 bar pressure in an argon atmosphere. Fatigue testing at room temperature was conducted at a frequency of 40 Hz with  $R = -1$ . All fatigue tests were performed at a maximum stress level of 600 MPa. A total of 5 specimens were tested for each configuration. Based on the results of this testing, specimens had a mean fatigue life of 28,900 cycles at the 600 MPa stress-level. Heat-treatment at 800 °C increased the mean fatigue life to 93,000 cycles and heat-treatment at 1050 °C further increased the mean fatigue life to 290,000 cycles. None of the HIP specimens failed at the 600 MPa stress level with a test run-out of  $2 \times 10^6$  cycles [17]. The mean fatigue life of the HIP specimens was determined using a staircase testing method on a total of 18 samples.

Analysis of the staircase data using the Dixon-Mood method resulted in a mean fatigue strength of 630 MPa with a standard deviation of 5.3 MPa [15]. The study by Leuders *et al.* included the results of residual stress measurements and porosity measurements. Reported data indicated residual stress measurements ranging from +90 to +775 MPa in the as-built specimens where the positive value represents a tensile stress. Heat-treatment at 800 °C reduced measured residual stresses to a range of -5 to +10 MPa where the negative value represents a compressive stress. Pore sizes were measured using computed tomography from data collected using microtomography scans. As-built specimens indicated a distribution of pores and voids throughout the material with diameters up to 50 µm. HIP-treated specimens did not indicate the presence of any pores above the minimum detection size limit of 22 µm. Leuders *et al.* concluded fatigue test data suggests stress concentrations from internal pores and defects has a much greater impact on fatigue strength than the influence of the microstructure. HIP was demonstrated to delay the fatigue crack initiation phase by reducing the measured porosity within the specimens [15].

The study by Rafi *et al.* addressed the differences in microstructure, mechanical properties, and fatigue life between Ti-64 produced by SLM versus those produced by EBM [36]. SLM specimens were fabricated with an EOS M 270 machine with a 30 µm layer thickness. Fatigue specimens were cylindrical-shaped but the build orientation and surface finish for the fatigue specimens are not specified. Fracture surface images suggest the surface was machined due to the smooth appearance of the edge circumference. It is also unspecified as to what, if any, heat-treatment or stress relief was performed. Room temperature fatigue testing was conducted at a frequency of 50 Hz at

$R = 0.1$ . Fatigue results indicate the fatigue life of the SLM specimens is near expected values for wrought Ti-64 material with a mean fatigue strength in the range of 500-550 MPa. Rafi *et al.* notes all fatigue failures initiated from within the internal region of the test specimens but did not attribute the failures to voids or porosity. Rafi *et al.* suggests the relatively good fatigue life observed in their study for the SLM Ti-64 samples was the result of the predominately martensitic phase in SLM Ti-64. The martensitic phase improves fatigue strength by impeding dislocation motion [36].

The study by Van Hooreweder *et al.* addressed the impact of a surface notch on the fatigue life of SLM Ti-64 [47]. Specimens were fabricated using an in-house developed SLM machine at the University of Leuven in Belgium. Flat, rectangular cross-section specimens were manufactured in the horizontal direction with a laser power of 250 watts, 30  $\mu\text{m}$  layer thickness, and processing parameters configured to minimize the amount of porosity. Notched specimens were created by using a wire electrical discharge machining process to cut notches with a designed  $k_t$  of 1.75 and 2.5. An elliptical shaped radius was used on the un-notched specimens to minimize the amount of stair-stepping from the SLM process. Fatigue testing was conducted at a frequency of 75 Hz with  $R = 0$ . Results of the fatigue testing indicate a mean fatigue strength of 126.2 MPa for a test run-out established at  $10^7$  cycles. The presence of a notch with  $k_t = 1.75$  reduced the mean fatigue life to 90.3 MPa and a notch with  $k_t = 2.5$  further reduced the mean fatigue life to 72.9 MPa [47]. The fatigue life results from the Van Hooreweder *et al.* study represent the lower range of SLM Ti-64 fatigue life data published in literature. However, this study utilized an in-house SLM machine versus a commercial machine where processing parameters are not pre-optimized by the manufacturer.

Finally, a doctoral dissertation by Simonelli [16] on the microstructural evolution and mechanical properties of SLM Ti-64 included limited fatigue testing on a single configuration. Flat, rectangular cross-section fatigue specimens were fabricated in the horizontal direction using a Renishaw AM250 machine with a 200 watt laser and 50  $\mu\text{m}$  layer thickness. Specimens were stress-relieved at 730  $^{\circ}\text{C}$  for 2 hours in a nitrogen atmosphere and then machined to improve the surface finish. Room temperature fatigue testing was conducting at a frequency of 10 Hz with  $R = 0.1$ . A total of five samples were tested at the same maximum stress level of 500 MPa. The results indicate the average fatigue life at 500 MPa is 24,775 cycles. Simonelli notes crack initiation sites were near the external surface of the specimens and appear to have originated from internal porosity close to the surface [29].

### **III. Test Methodology and Procedures**

#### **3.1. Applicable Standards and Guidance**

ASTM Standard F2924-14 was published in 2014 as the overarching standard for AM Ti-64 produced by powder bed fusion. This standard addresses terminology, manufacturing, powder feedstock, machine processing, mechanical properties, thermal processing, quality, inspection and other requirements [57]. To the extent possible, test specimens used in this study were manufactured and tested in accordance with the guidelines and requirements of ASTM F2924-14. Per ASTM F2924-14, mechanical properties are determined following the procedures of ASTM E8/E8M, Standard Test Methods for Tension Testing of Metallic Materials, and fatigue testing is conducted in accordance with ASTM E466, Standard Practice for Conducting Force Controlled Constant Amplitude Axial Fatigue Tests of Metallic Materials, and/or ASTM E606, Standard Test Method for Strain-Controlled Fatigue Testing.

The coordinate system used herein to describe the orientation of test specimens follows the coordinate system defined in ISO/ASTM 52921:2013 [58]. This coordinate system is based on the initial build orientation with respect to the build chamber using orthogonal orientation notation. The ISO/ASTM 5291:2013 orthogonal orientation coordinate system is depicted below in Figure 2. From Figure 2, the Z-axis is normal to the layers added by the build process. The X-axis is perpendicular to the Z-axis and parallel to the front of the machine's build volume and the Y-axis is the remaining orthogonal direction. The origin of the coordinate system (0,0,0) is defined by the geometric center of the build plate surface and positive X, Y, and Z directions are as shown in Figure 2. Following the convention in ISO/ASTM 5291:2013, when a part on

the build plate is aligned parallel to the defined XYZ axes, it is described with a 3-axis designation. The first letter corresponds to the axis parallel to the longest dimension of the part, the second letter corresponds to the axis parallel to the second longest dimension, and the third letter corresponds to the axis parallel to the shortest dimension. For the sample part shown in Figure 2, the build orientation is described as XZY. The position of a part on the build plate is described by the three-dimensional location of the part's centroid with respect to the origin of the build plate. Additionally, for parts placed on the build plate with orientations not parallel to the build plate's XYZ axes, a description of the part's rotation with respect to the build plate's axes is needed. The details of defining such part rotations are found in ISO/ASTM 52921 [58].

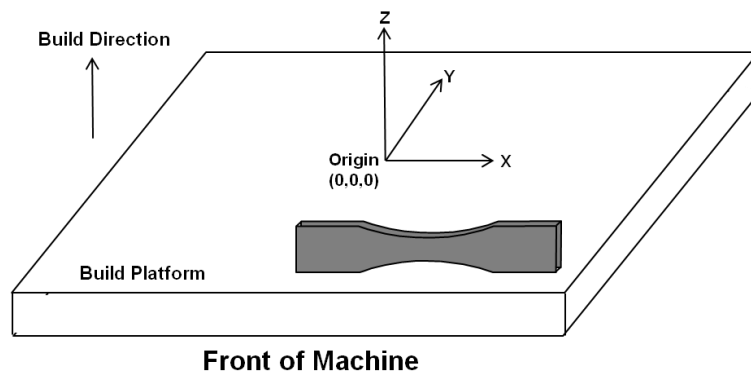


*Figure 2. ISO/ASTM 5291:2013 Orthogonal Orientation Coordinate System.*

### **3.2. Test Specimen Design**

The tensile specimens for this study were designed in accordance with ASTM E8/E8M. Since the load cell on the MTS Landmark test machine used in this study has a maximum force limit of 25 kN, the cross-sectional area of the test specimens is limited by the required maximum applied stress to exceed the UTS of the material. Allowance of a 10% margin for the maximum load capacity restricts the maximum available force to

22.5 kN. As shown in equation (7), the applied stress ( $S$ ) is found by dividing the applied force ( $F$ ) by the cross-sectional area ( $A$ ).

$$S = \frac{F}{A} \quad (7)$$

Based on the material data sheet for EOS Ti-64 published by the manufacturer, the expected UTS is 1250 MPa for the as-built material [59]. Using equation (7) to solve for the cross-sectional area with a force equal to 22.5 kN and stress equal to 1250 MPa, the maximum allowable area is 18 mm<sup>2</sup>. To minimize material costs and stay within the maximum applied tensile load limit, tensile specimens were designed to the ‘subsize specimen’ criteria defined in ASTM E8/E8M. The grips installed in the available test equipment could not accommodate round specimens, therefore flat specimens were required to permit adequate gripping. In accordance with the specifications in ASTM E8/E8M and given a maximum cross-sectional area limit of 18 mm<sup>2</sup>, the tensile specimens were designed to a gauge length of 25 mm, 3 mm thickness, 6mm width, and overall length of 100 mm as shown in Figure 3. The full list of dimensions for a subsize specimen specified by ASTM E8/E8M and the nominal values of the design specifications utilized for this study are presented in Table 4.

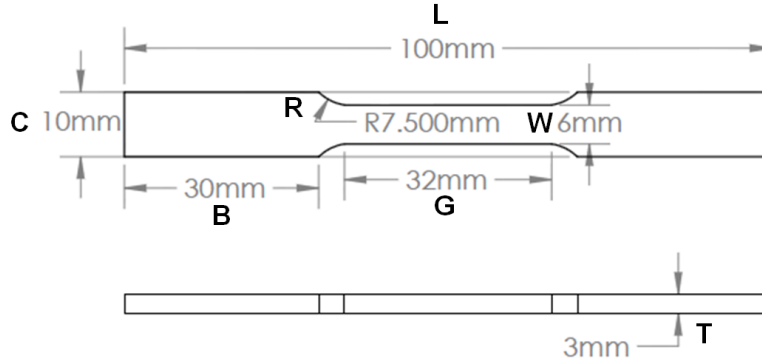


**Figure 3. Tensile specimen design dimensions utilized for this study.**

**Table 4. ASTM E8/E8M specifications for subsize tensile specimens and the nominal design specifications utilized for this study.**

	<b>ASTM E8/E8M Specification</b>	<b>Design Specification</b>
<b>W – Width (mm)</b>	6.0 ± 0.1	6.0
<b>T – Thickness (mm)</b>	6.0 (maximum)	3.0
<b>R –Radius of fillet (mm)</b>	6.0 (minimum)	7.5
<b>L – Overall Length (mm)</b>	100	100.0
<b>A – Length of reduced section (mm)</b>	32	32.0
<b>B – Length of grip section (mm)</b>	30	30.0
<b>C – Width of grip section (mm)</b>	10	10.0

Fatigue specimens with  $k_t \approx 1$  were designed in accordance with the requirements specified in ASTM E466-07 [56]. As was the case for the tensile specimens, flat specimens were required for compatibility with the gripping surfaces on the available test equipment. ASTM E466-07 provides the option for either a uniform test section of a specified gauge length with tangentially blended fillets between the gripping ends or a continuous radius between the ends. In a previous SLM Ti-64 study by Simonelli, thin, rectangular cross-section HCF testing specimens were built slightly oversized and then machined to a 65 mm uniform gauge length with a fillet transition to the grip areas at the

ends of the specimen. Simonelli reported each of the five samples tested at 10 Hz,  $R = 0.1$ , and stress level of 500 MPa all had failure points at the end of the necking region along the fillet. These failures were attributed to a stress concentration at the base of the necking region [16]. On account a stress concentration at the base of a necking region is potentially intensified by the effect of stair-stepping along the edge surfaces of the un-machined samples in this study, a continuous radius between the gripping ends was chosen in an attempt to keep the fatigue failure location near the center of the test specimens.

For fatigue specimens with a rectangular cross section and continuous radius between the ends, ASTM E466-07 specifies the radius of curvature between the ends is at least eight times the minimum width of the test section to minimize  $k_t$ . Additionally, the ratio of the test section width to thickness has a specified range between two and six and the cross-sectional area of the test section at the location of minimum width has an allowable range of 19.4 mm<sup>2</sup> to 645 mm<sup>2</sup> [56]. Similar to the limitation experienced with the tensile specimens, the cross-sectional area of the fatigue specimens is limited by the maximum stress level at which fatigue loading is accomplished with respect to the maximum load capacity of the testing equipment. Based on HCF data from previous SLM Ti-64 studies, the maximum desired stress level for this study was 700 MPa. Using equation (7) to solve for the cross-sectional area with force equal to a maximum load limit of 22.5 kN and stress equal to 700 MPa results in a maximum cross-sectional area of 32.1 mm<sup>2</sup>. To achieve a target cross-sectional area of 30 mm<sup>2</sup> at the location of minimum width, the fatigue specimens were designed with a reduced width of 10 mm at the center of the test section, 3 mm thickness, 20 mm maximum width, and 125 mm

overall length as shown in Figure 4. This resulted in a width to thickness ratio of 3.3 and radius of curvature of 108.1 mm to comply with the requirements of ASTM E466-07 as shown in Table 5.

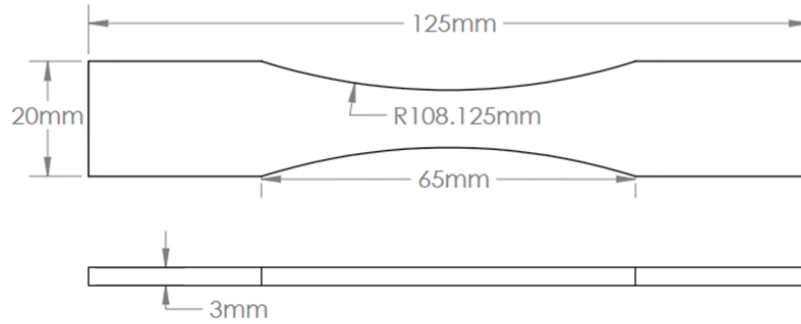


**Figure 4. Fatigue specimen design dimensions utilized for this study.**

**Table 5. ASTM E466-07 requirements for axial fatigue specimens and the design specifications utilized for this study.**

	<b>ASTM E466-07 Requirement</b>	<b>Design Specification</b>
<b>Allowable Cross-Sectional Area (mm<sup>2</sup>)</b>	19.4 – 645	30.0
<b>Radius of curvature to width*</b>	≥8.0	10.8
<b>Range of width* to thickness ratio</b>	2 - 6	3.3

\* width at point of minimum reduced area

### 3.3. Test Specimen Manufacturing

The fatigue and tensile testing specimens for this study were fabricated using an EOSINT M 280 machine. A photograph of the EOSINT M 280 is shown in Figure 5. The EOSINT M 280 utilizes the EOS proprietary DLMS process. The following equipment description is adapted from the EOSINT M 280 Technical Description published by the manufacturer [60]. The primary components of the M 280 are a 250 mm × 250 mm × 250 mm build chamber, recoating system to distribute the powder

material over the build surface, powder dispenser, laser system to melt the powder, optical system to direct the laser, inert gas management system, and a processing computer with process control software. The basic model is equipped with a 200 watt Ytterbium fiber laser with a 1060 to 1100 nm wavelength or optionally equipped with a 400 watt laser as was the case for the machine used in this study. Cooling to the laser is supplied by a water-air cooler. The diameter of the laser beam on the build surface is controlled by a focusing objective and is variable from 100 – 500  $\mu\text{m}$ . The build platform has a surface area of 250 mm  $\times$  250 mm. For this study, the build platform was constructed of Ti-64 to match the material of the fabricated parts and had a thickness of 25 mm. The build platform is mounted to a platform carrier which raises the build platform vertically with each successive layer. The platform carrier is equipped with a heating module to maintain the operating temperature of the build plate between 40 and 100  $^{\circ}\text{C}$ . The heated platform helps to reduce internal stresses and ensure adequate bonding of the first several layers by reducing the temperature gradients between the fabricated parts and the building platform. An inert gas system maintains a nitrogen or argon atmosphere within the build volume to allow processing of metals reactive to air. For processing of Ti-64, an argon atmosphere is utilized. The M 280 utilized in this study was equipped with an automated powder re-capturing system to recycle un-melted powder from the build volume.



*Figure 5. EOSINT M 280 used for test specimen fabrication.*

The tensile and fatigue specimen geometries from Figures 3 and 4 were first modeled in SolidWorks to produce a 3D CAD model. The model was then exported from SolidWorks in a STEP file format and provided to the vendor. The vendor utilized the EOS proprietary RP-Tools software application to arrange the individual parts on the build plate and process the STEP file into an EOS SLI file format used for the DMLS process. The SLI format slices the 3D model into printable 2D layers. The RP-Tools application automatically identifies and fixes any data errors resulting from the file conversion process [60].

The EOSINT M 280 utilizes standardized parameter sets controlled by a part property management (PPM) module in the EOS software. From the EOSINT M 280 Technical Guide, the PPM consists of a collection of Part Property Profiles (PPP) each tailored to a specific material and performance objective. The purpose of a PPP is to standardize the properties of manufactured parts and ensure consistency from build to build. PPPs are established by the manufacturer and are not altered by a standard user.

Four categories of PPPs are available including ‘Surface’, ‘Performance’, ‘Speed’, and ‘TopSpeed’. Although the manufacturer reports all PPPs deliver fully-dense parts with comparable mechanical properties, each PPP sets the layer thickness, laser power, scan strategy, and other parameters to manage tradeoffs between surface quality, material properties, accuracy, and detail resolution [61]. The available parameter sets are dependent on the specific build material and the configuration of the EOSINT machine. For Ti-64, EOS offers a ‘Performance’ parameter set with 30  $\mu\text{m}$  layer thickness, and a ‘Speed’ parameter set with 60  $\mu\text{m}$  layers available on machines equipped with a 400 watt laser. Per the EOSINT M 280 Technical Description, the ‘Speed’ parameter set offers an optimal compromise between production speed and surface quality. To minimize production costs, all builds for this study were intended to use the ‘Ti64 Speed version 1.03’ parameter set.

To produce desired quantity of 20 tensile and 65 fatigue specimens, a total of three separate builds were required. The number of required builds was driven by the maximum number of parts fitting on a single build plate. Sufficient spacing between parts is necessary to allow adequate heat dissipation during the build process and facilitate removal of the parts from the build plate. It was initially desired to fabricate the test specimens in the Z, or vertical, orientation to collect test data accounting for the worst-case material properties and maximize the number of specimens which could fit on a single build plate. However, pricing for fabrication in the Z-orientation was approximately three times the cost of manufacturing in the XY-orientation. The cost increase is primarily driven by the additional machine time requirements on account the DMLS process manufactures material faster in the horizontal plane in terms of material

volume per unit of time compared to the speed of adding successive layers in the vertical direction. To stay within available budget, an XY-orientation was elected and specimens were allocated among three separate build plates. The individual specimens were arranged on the build plates in the XZY-orientation when described using the ISO/ASTM 5292 orthogonal orientation notation. The first build consisted of 10 tensile and 19 fatigue specimens as shown in Figure 6. The second build consisted of 18 fatigue specimens and the third build consisted of 10 tensile specimens and 28 fatigue specimens as shown in Figure 7.

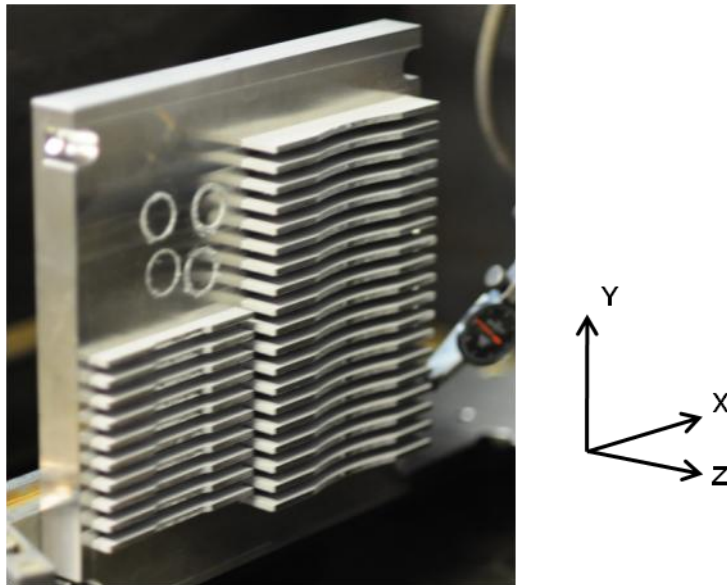


***Figure 6. Photograph of first build plate consisting of 10 tensile and 19 fatigue specimens.***

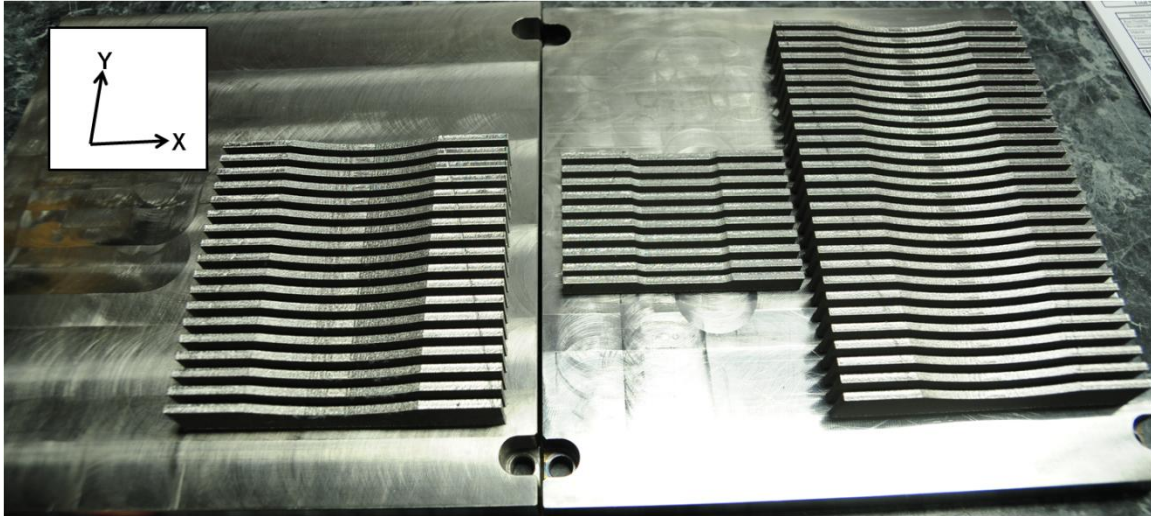


**Figure 7. Photograph of second build plate (left) consisting of 18 fatigue specimens and third build plate (right) consisting of 10 tensile and 28 fatigue specimens.**

After each build was completed, the build plate assembly was removed from the EOSINT M 280 machine and allowed to cool to room temperature under ambient conditions. Next, the build plate was installed in a separate machine to cut the parts from the build plate using a wire electrical discharge machining (EDM) process. Wire-EDM is a common machining process for high strength alloys where electrical current discharged between a small wire electrode and the work piece melts and vaporizes small amounts of material. Cut material is flushed away by a dielectric liquid medium in which the work piece is immersed [62]. The wire-EDM traces a path along the boundary of the part to cut the part from the build plate. In addition to removal from the build plate, the wire-EDM also removed support material as shown in Figure 8. Support material was required underneath the reduced area section of the test specimens to prevent the center of the specimen from collapsing during the layered build process.

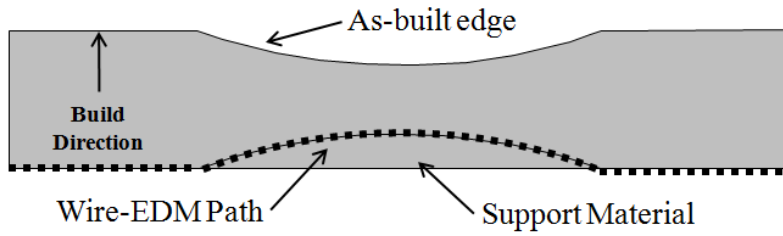


**Figure 8. Cutting path of the wire-EDM to remove specimens from the substrate plate.**

Use of the wire-EDM created two distinct surface finishes on the edges of each specimen. One surface was cut relatively smooth by the wire-EDM while the opposing surface was left in its as-built state. Since the specimens were manufactured using a layer-by-layer process, inclined surfaces not aligned parallel with the XYZ build axes results in a stair-stepping effect along the surface [4]. This stair step effect is illustrated in Figure 9.

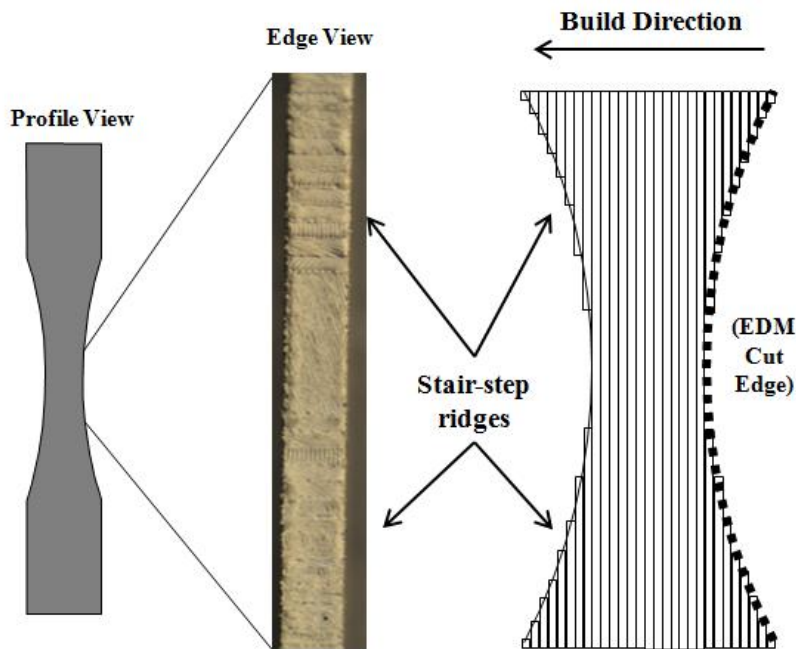


**Figure 9. Depiction of the stair-step effect on inclined surfaces resulting from the layered build process.**

A comparison between the wire-EDM and as-built edge surfaces is shown in the optical microscope images in Figure 10. The wire-EDM surface in Figure 10A is characterized by small craters on the surface caused by the electrical discharges emitted between the electrical diode and material during the wire-EDM process [63]. As discussed in Liao, proper control of discharge energy during wire-EDM results in a process capable of precise cutting and produces a fine textured surface finish resistant to corrosion and wear [63]. As shown in Figure 10B, the as-built edge surface has a slightly rougher surface appearance. Note the edge surface shown in this image is from the uniform gauge section of the tensile specimen and therefore no stair-stepping is present since the surface is a flat, horizontal surface in the XY plane. The angled striations visible on the as-built surface result from the hatch-spacing and scanning direction of the laser as it rasters across the build surface.

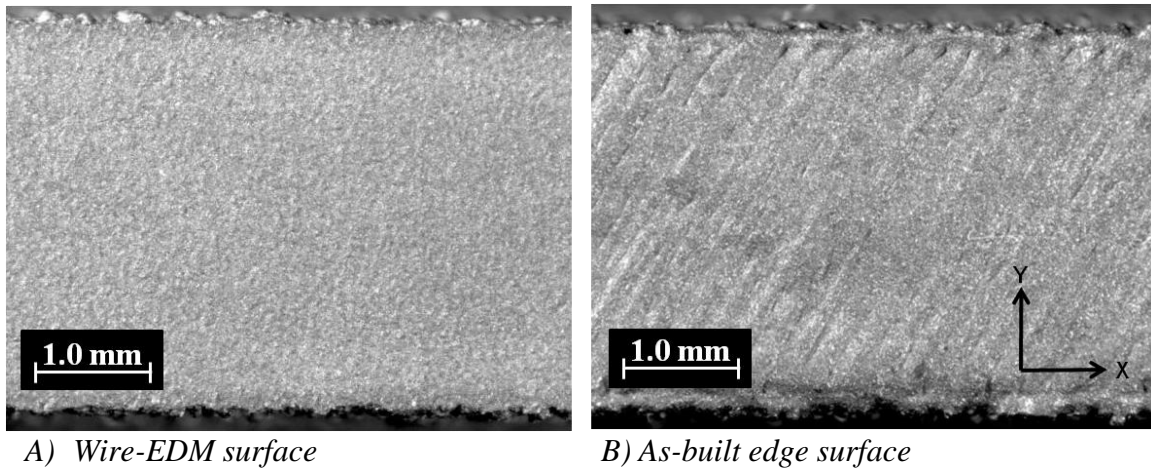


***Figure 10. Optical microscope images taken with 0.63 × objective lens showing a comparison of the surface quality between the as-built edge and the edge cut by wire-EDM along the uniform gauge section of a tensile specimen.***

Due to ordering delays, the second and third builds were performed just over three months after completion of the first build. A single order was placed for the first build and a second order was later placed for the second and thirds builds. Two unintended configuration differences resulted between builds one, two, and three. The first difference is the composition of the support material beneath the center of the reduced area section of the test specimens. In the first build, the material support was built with solid, fully dense material matching the rest of the specimen. The wire-EDM then cut through the solid material to trace the lower profile of the specimen. In the second and third builds, reduced density support material with a foam-like structure was utilized in for material support as shown in the photograph in Figure 11.

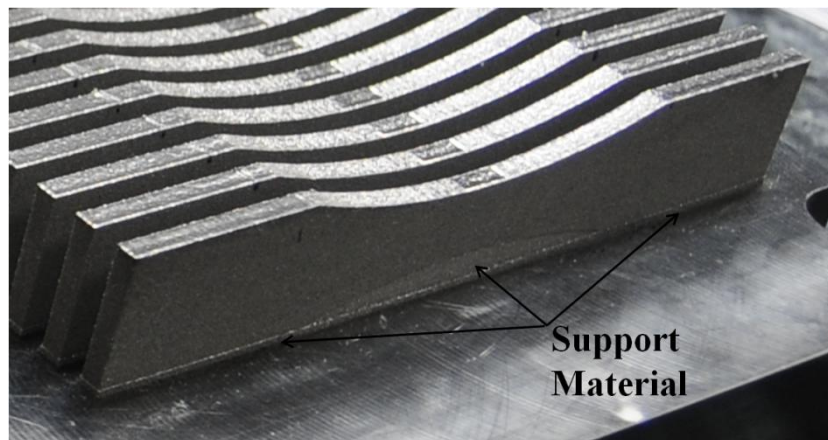


*Figure 11. Photograph of Build 2 showing the reduced-density support material underneath the parts.*

Although the use of lower-density support consumes a smaller volume of feed material, it creates a boundary between the fully dense part and the lower-density support material. Due to a small amount of warpage occurring in the build plate during the build process, the wire-EDM, guided by CNC based on the original CAD file for the parts, was unable to precisely trace the boundary between the fully dense part and the support

material. As a result, a small amount of support material was left behind after removal of the specimens from the build plate with the wire-EDM. This required additional machining by the vendor using a CNC mill to remove the remaining support material.

The second configuration difference between the specimens is the processing parameters of the EOSINT M 280 machine. As previously noted, the original intent was to use the ‘speed’ parameter set with 60  $\mu\text{m}$  layer thickness. However, incorrect processing parameters were used in the second and third builds. These builds were performed using the ‘performance’ parameter set with 30  $\mu\text{m}$  layer thickness. Per the job control and quality reports produced by the EOSINT M 280 software application, 350 layers were utilized to construct the 21.0 mm Z-height of the first build which consisted of the 20 mm part height plus an additional 1.0 mm layer of solid material beneath the parts to provide spacing for the wire-EDM process. The second and third builds were built with 667 layers to construct the 20.0 mm Z-height which excludes additional layers of reduced-density support material beneath the parts. In terms of build duration, the first build required 9.73 hours, the second build required 12.33 hours, and the third build required 20.57 hours. The quantities of specimens, build parameters, and build times are summarized in Table 6. As shown in Table 6, the average build time per specimen approximately doubles when the layer thickness is reduced to 30  $\mu\text{m}$ .

***Table 6. Summary of specimen quantities, layer thickness, and build time.***

<b>Build</b>	<b>Tensile Qty</b>	<b>Fatigue Qty</b>	<b>Total Qty</b>	<b>Layer Thickness</b>	<b>Build Time</b>	<b>Avg Time per Specimen</b>
1	10	19	29	60 $\mu\text{m}$	9.73 hrs	20.1 mins
2	18	0	18	30 $\mu\text{m}$	12.33 hrs	41.1 mins
3	10	28	38	30 $\mu\text{m}$	20.57 hrs	44.1 mins

### 3.4. Post-Processing Heat Treatment

After receipt of the specimens from the SLM vendor, the specimens were cleaned with a 90% isopropyl alcohol solution to ensure the surfaces were free of debris and oils prior to heat treatment. The process parameters used for the stress relief in this study followed the heat treatment parameters of 800 °C for 4 hours in an argon atmosphere specified in the EOS Ti-64 Material Data Sheet [59]. According to this data sheet, this heat treatment is recommended to produce material properties which exceed the minimum requirements of ASTM F1472-08 (Standard Specification for Wrought Titanium-6Aluminum-4Vanadium Alloy for Surgical Implant Applications), ASTM B348-09 (Standard Specification for Titanium and Titanium Alloy Bars and Billets), and ISO 5832-3:2000 (Implants for surgery - Metallic materials). In response to an inquiry to the manufacturer to provide further clarification on the rationale behind the recommended heat treatment parameters, EOS responded the primary intent is to increase the elongation at break which is desirable for medical applications [64]. The heat-treatment vendor accomplished the stress relief in a vacuum furnace with an argon backfill at a temperature ramp rate of 20-30 °F (11.1-16 °C) per minute, 4 hour soak time at 1470 °F +/- 25 °F (798.9 °C +/- 13.9 °C), followed by fan cooling to room temperature.

Specimens identified for HIP were sent to a separate vendor for processing. ASTM F2924-14 specifies HIP is conducted under an inert atmosphere at pressure equal to or greater than 100 MPa at a temperature range of 895 to 955 °C for 2 to 4 hours following by cooling under the inert atmosphere to below 425 °C. The process parameters used by the vendor were 1650 °F +/- 25 °F (898.9 °C +/- 13.9 °C) for 2 hours at a relative pressure of 14.75 ksi +/- .25 ksi (101.7 MPa +/- 1.7 MPa).

### **3.5. Summary of Final Specimen Configurations**

A summary of the specimen configurations and build traceability is shown in Table 7. For purposes of specimen tracking, the specimens produced in builds two and three are treated as a single lot on account the specimens were intermixed and indistinguishable from each other upon receipt from the vendor. The original intent was to produce a total of 15 tensile specimens to determine the static material properties of the as-built, stress-relieved, and HIP configurations using five test specimens per configuration. However, post-test data analysis of the stress-relieved specimens produced in Build 1 indicated a calibration issue with the extensometer. An additional quantity of 5 tensile specimens was added to the second build to re-accomplish the stress-relieved tensile tests. This decision was made without prior knowledge the specimens in builds two and three were produced at a different layer thickness than the first build. The UTS values obtained for the Build 1 stress-relieved specimens with 60  $\mu\text{m}$  build layer thickness are valid despite the incorrect extensometer data. Therefore, the additional Build 2/3 stress-relieved tensile specimens provided data to make a comparison between the UTS of the 30  $\mu\text{m}$  and 60  $\mu\text{m}$  build layer thicknesses of the stress-relieved configuration. Specimens produced in builds two and three are designated as the Build 2/3 specimens herein to denote the specimens produced with a build layer thickness of 30  $\mu\text{m}$ .

*Table 7. Summary of specimen configurations and quantities.*

Configuration	Build	Layer Thickness	Tensile Qty	Tensile Total	Fatigue Qty	Fatigue Total
As-Built	1	60 $\mu\text{m}$	-	5	-	None
	2/3	30 $\mu\text{m}$	5		-	
Stress-Relived	1	60 $\mu\text{m}$	5	10	19	30
	2/3	30 $\mu\text{m}$	5		11	
HIP	1	60 $\mu\text{m}$	5	5	-	25
	2/3	30 $\mu\text{m}$	-		25	
HIP + Machined Edges	2/3	30 $\mu\text{m}$	-	-	10	10

As shown in Table 7, a second HIP-treated configuration was added using 10 of the 35 HIP-treated fatigue specimens produced in Build 2/3. The purpose of this additional HIP-treated configuration is to assess the impact on fatigue life from removing the stair-step ridges from the edge of the specimen. In this second HIP configuration, the narrow edges of the specimen were machined to a smooth finish with a CNC mill. The as-built edge was machined to remove the stair-step ridges and the wire-EDM edge was machined to match the surface finishes of both edges. The remaining sides along the wider width of the specimens were not machined and left in their as-built state.

### **3.6. Tensile Testing**

Tensile testing was conducted in accordance with ASTM E8/E8M [65]. Testing was accomplished with an MTS Systems Landmark Servo-Hydraulic Test System equipped with a 25 kN force-capacity load cell as shown in Figure 12. The test machine was controlled with an MTS Flex Test 40 controller utilizing the MTS 793 Station Manager control software. Specimens were mounted using MTS model 647 hydraulic wedge grips. Axial and concentric alignment of the grips was performed prior to testing

using the MTS 709 Alignment System software application with a sample specimen. The sample specimen was instrumented with strain gauges to determine the bending moments. Appropriate alignment adjustments were made to achieve minimum bending moments on a gripped specimen. The 25 kN force-capacity load cell had an up-to-date calibration certificate for a force-verification calibration performed within the past 24 months by a factory-trained technician.

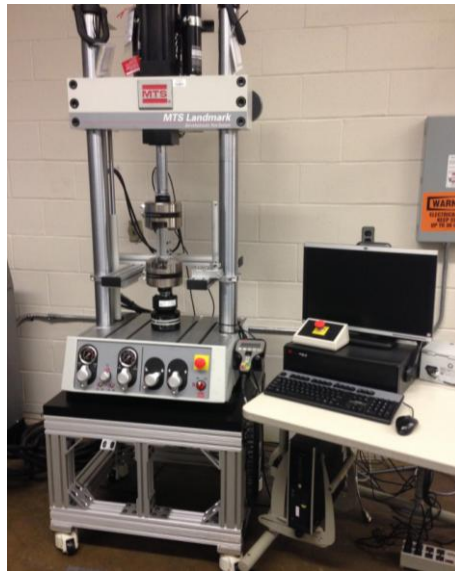


***Figure 12. MTS Landmark Servo-Hydraulic Test System.***

Strain data was measured with an MTS model 632.53E-14 extensometer with a 12.7 mm gauge length as shown in Figure 13. ASTM F2924-14 specifies the strain rate during tension testing of SLM Ti-64 is between 0.003 to 0.007 mm/mm/min through the yield point of the material [57]. To stay within this range, a target strain rate of 0.005 mm/mm/min was selected. However, the MTS Station Manager application software used to control the test was not configured to control testing via strain rate control. Control was limited to force or displacement only. Using the displacement control mode,

it was found the target strain rate of 0.005 mm/mm/min was approximately achieved by using a constant crosshead displacement rate of 0.5 mm/min.



***Figure 13. MTS model 632.53E-14 extensometer installed during tension test.***

Since the elongation at break indicated by an extensometer is often unreliable due to the dynamic behavior of testing at the time of fracture, ASTM E8/E8M provides procedures for determining the elongation at break using manual measurements of gauge marks. For elongations greater than 3%, ASTM E8/E8M specifies the gauge-length is measured to the nearest 0.01 inch (0.25 mm) [65]. Prior to each tensile test, a 1.0 inch (25.4 mm) gauge length was placed on each specimen using light ink markings. Gauge-lengths were obtained using the measurement feature in a software application connected to an optical microscope. Measurements were recorded from images of test specimens obtained at a 5× level of magnification. An example of gauge-length measurements obtained before testing and after tensile failure is shown in Figure 14.

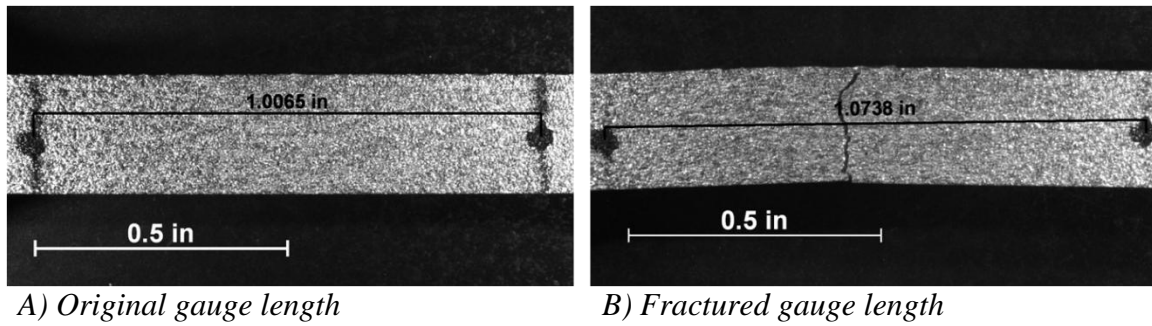


**Figure 14. Sample elongation at break measurement using optical microscope as viewed at  $5\times$  magnification through a  $0.63\times$  objective lens.**

Throughout each tensile test, applied force, displacement, and strain data were recorded at an acquisition rate of 60 Hz. To produce plots of stress versus strain, the applied force is converted to engineering stress. Engineering stress is the nominal stress applied to the original cross-sectional area of the test specimen without accounting for the instantaneous increase in true stress occurring as a result of the decrease in cross-sectional area as necking occurs [66]. The engineering stress is calculated using equation (7). The original cross-sectional area of each specimen was determined from measurements of the test section dimensions taken prior to each test. ASTM E8/E8M specifies dimensions greater than 0.200 inch (5 mm) are measured to the nearest 0.001 inch and dimensions between 0.100-0.200 inches (2.5-5 mm) are measured to the nearest 0.0005 inch [65]. In accordance with the ASTM guidelines, test section width and thickness measurements were obtained with a micrometer to the nearest 0.0001 inch. All measurements were recorded in inches and then converted to millimeters for stress calculations. The value of the cross-sectional area used for engineering stress calculations was the average of dimensional measurements taken at the top, middle, and bottom regions along the length of the uniform test section.

Engineering stress versus strain plots were generated to determine the UTS, YS, and E. UTS is the maximum value of stress applied to the specimen prior to fracture. The YS was determined using the 0.2% offset method described in ASTM E8/E8M [65]. Although the 0.2% offset YS procedure in ASTM E8/E8M is described graphically, the value is found more accurately by determining the equation of a line with a slope equal to the slope of linear elastic portion of the stress-strain curve and then offset by a strain value of +0.2%. An equation for the stress-strain curve is then approximated using a logarithmic curve fit. The 0.2% offset YS occurs at the intercept of the offset line with the stress versus strain curve. Determining the slope of the offset line requires the calculation of E. To calculate E, a linear fit was determined for the linear region of the stress versus strain curve using the method of least squares linear fit model. A sample tensile test plot illustrating the relationship of UTS, YS, and E with the stress versus strain curve is shown in Figure 15.

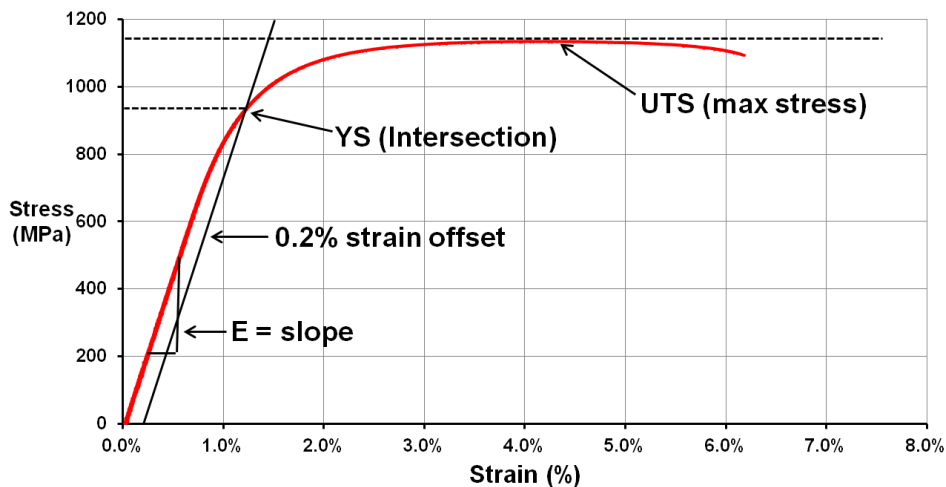


*Figure 15. Sample stress vs. strain curve.*

### 3.7. Fatigue Testing

High-cycle fatigue testing was conducted in accordance with the procedures for force-controlled, constant amplitude testing described in ASTM E466-07 [56]. Testing was performed using the same MTS Landmark system used for tensile testing. All tests were conducted at room temperature. The independent HCF testing variables are the stress ratio and maximum stress level. To limit the scope of testing within available time and resource constraints, the stress ratio was fixed at  $R = 0.1$  and the maximum stress level became the single independent variable. To perform testing efficiently, it was desired to conduct testing at the highest appropriate frequency. ASTM E466-07 indicates the fatigue strength of metallic materials is generally unaffected by testing frequencies in the range of 0.01 to 100 Hz [56]. The MTS Landmark testing system used for this study has a maximum frequency limit of 100 Hz. However, system performance data from the manufacture indicates the usable dynamic performance range is slightly diminished as the amplitude of displacements and/or the force of applied loads are increased [67]. Based on the system performance chart from MTS, a frequency of 60 Hz was selected to provide satisfactory system performance at  $R = 0.1$ . Cyclic loads were applied with a sinusoidal waveform as recommended by ASTM E466-07 [56]. The failure criteria for test termination were established as full separation of the specimen or test run-out at  $10^7$  cycles.

Previously published SLM Ti-64 data indicates when HCF stress-life data is plotted with the number of cycles to failure presented in a logarithmic scale, the data follows a linear trend in a finite-life region followed by a horizontal asymptote corresponding to a

mean fatigue life as the maximum applied stress is reduced [9, 31, 47]. Based on this trend, the expected stress-life curve is modeled by equation (8) [4].

$$\log N = A_1 + A_2(S_{\max} - \bar{\mu}) \quad (8)$$

In equation (8),  $N$  is the number of cycles,  $S_{\max}$  is the maximum applied stress,  $A_1$  and  $A_2$  are the curve fitting parameters, and  $\bar{\mu}$  is the mean fatigue strength.

The mean fatigue strength,  $\bar{\mu}$ , was determined using the up-and-down staircase method described in ASTM STP 588 [68]. The first specimen in a staircase test is tested at a maximum stress level corresponding to the expected mean fatigue strength of the material. Since limited research is published on HCF life of SLM Ti-64 when the surface is un-machined, the mean fatigue life is not reliably estimated prior to testing. To approximate the mean fatigue life, specimens from the stress-relieved configuration were first run at higher stress levels in the finite life region to provide insight into the HCF life. Based on the number of cycles to failure, the stress level was reduced in various increments until a run-out occurred at  $10^7$  cycles. The approximate mean fatigue life was then estimated from the initial data points. For the HIP configuration, a more efficient means of estimating the mean fatigue life was accomplished through accelerated stress testing. Using the accelerated method, a single specimen was tested at a stress level below the expected mean fatigue strength for a duration of  $10^6$  cycles. After each set of  $10^6$  cycles, the maximum stress was increased by 10 MPa. The same specimen was re-tested at increasing stress levels until a failure occurred. The highest stress level at which the specimen survived to  $10^6$  cycles was then used as the first data point in the staircase. The remaining points in the staircase are conducted based on the outcome of the

preceding test. When a specimen fails, the next specimen is tested at a lower stress level. If the specimen survives to  $10^7$  cycles, the next specimen is tested at a higher stress level. Stress values for each level of the staircase were established at uniform increments of 10 MPa.

The staircase testing data was analyzed using the Dixon-Mood approach. The Dixon-Mood approach is a common method for statistical analysis of staircase data [53]. As discussed in Pollack, the primary advantage of staircase testing is the nature of the test concentrates data near the mean which increases the accuracy of the estimate of the true population mean [7]. A second advantage is the relative simplicity of calculating the mean and standard deviation using algebraic equations. These simplified equations may be used when step sizes between stress levels are uniform increments. The most commonly used equations to analyze staircase data were first introduced in 1948 by explosives researchers Dixon and Mood [7]. The Dixon-Mood equations are based on maximum likelihood estimation [69]. Maximum likelihood theory is a method of statistically estimating the parameters of a mathematical model by using a sample of experimentally collected data points. If the shape of the true distribution is assumed, the mean and variance of the distribution is estimated in a manner to provide the maximum likelihood of producing the experimental data points [70]. The Dixon-Mood equations are shown in equations (9-11).

$$\bar{\mu} = S_0 + s \times \left( \frac{B}{A} \pm 0.5 \right) \quad (9)$$

$$\bar{\sigma} = \begin{cases} 1.62 \times s \times \left( \frac{A \times C - B^2}{A^2} + 0.029 \right), & \text{for } \frac{A \times C - B^2}{A^2} \geq 0.3 \\ 0.53 \times s, & \text{for } \frac{A \times C - B^2}{A^2} < 0.3 \end{cases} \quad (10)$$

$$A = \sum_{i=0}^{i_{\max}} m_i, B = \sum_{i=0}^{i_{\max}} i m_i, C = \sum_{i=0}^{i_{\max}} i^2 m_i \quad (11)$$

In equations (9-11), the symbol  $i$  represents an integer corresponding to the stress level. The highest stress level in the staircase is denoted  $i_{\max}$ . In equation (9), the use of a positive or negative value inside the brackets is dependent on whether the majority of specimens in the staircase are survivals or failures. The negative value is used when the majority of specimens in the staircase are survivals after  $10^7$  cycles. Likewise, the positive value is used when the majority of specimens in the staircase are failures. For the case where the majority of specimens are survivals,  $i = 0$  corresponds to the minimum stress level at which a failure was observed. The symbol  $m_i$  denotes the number of specimens failing at each stress level. For the case where the majority of specimens are failures,  $i = 0$  corresponds to the minimum stress level at which a survival was observed and  $m_i$  denotes the number of specimens surviving at each stress level. The variable  $S_0$  denotes the value of stress corresponding to the stress level  $i = 0$ . The variable  $s$  denotes the size of the uniform stress increment.

To provide reliable estimates of the mean and standard deviation using maximum likelihood, the Dixon-Mood equations rely on three general conditions and assumptions [7]. The first condition is the underlying data is assumed to have a normal distribution.

The second condition is the sample size is large with 40 to 50 specimens or more. However, Pollack cites research by Brownlee *et al.* which concluded the Dixon-Mood equations provide a reasonably accurate estimate of the mean and standard deviation with sample sizes as small as five. Pollack also notes current fatigue testing procedures employed by the Japan Society of Mechanical Engineers utilize a six-specimen sample size to perform staircase testing [7]. The final condition of the Dixon-Mood equations is the step size used between each stress level in the staircase is between 50 to 200% of the true standard deviation [7]. Therefore, estimation of the standard deviation is required prior to testing to determine the appropriate step size. Based on previous SLM Ti-64 research by Van Hooreweder *et al.* which reported  $\bar{\sigma} = 8.3$  MPa for a similar test set-up with machined specimens, a uniform step size of 10 MPa was selected for this study [47].

### 3.8. Fracture Surface Examination

Fracture surfaces from tensile and fatigue specimens were examined under both optical and scanning electron microscopes (SEM). The optical microscope used for fracture surface examination in this study was a Zeiss Discovery V12 shown in Figure 16. The microscope was equipped with PlanApo S lenses with objectives of 0.65 $\times$ , 1.0 $\times$ , and 1.5 $\times$ . The optics on the camera adapter provided 10 $\times$  magnification and was coupled with a motorized zoom providing additional magnification of 0.8 $\times$  to 10 $\times$ . Images were captured with an AxioCam HRc digital camera attached to the microscope and operated by AxioVision software.



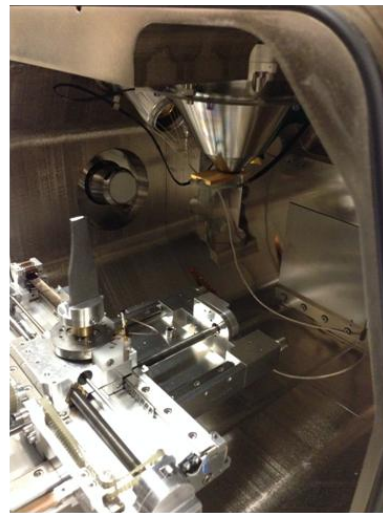
*Figure 16. Zeiss Discovery V12 Optical Microscope.*

The SEM utilized was an FEI Quanta 600F equipped with several detectors including secondary electron, electron backscatter diffraction, and energy dispersive spectrometer. An SEM emits an electron beam within a vacuum chamber. The beam is focused through an optics system onto a small spot on the specimen's surface. As the focused electron beam is rastered over the specimen, interactions between the electron beam and the specimen's surface are captured by the secondary electron detector and

processed into an image by mapping the variations of intensity. The result is a high resolution image at magnifications in excess of 20,000× with resolution as small as one nanometer. An elemental composition of an areas or specific point on a surface is obtained using an energy dispersive spectrometer (EDS) to characterize the presence and relative quantity of specific elements by measuring the x-ray spectrum emitted by the surface [71]. A photograph of the FEI Quanta 600F SEM utilized in this study is shown in Figure 17.



*A) Quanta 600F exterior view*



*B) Chamber interior*

***Figure 17. FEI Quanta 600F SEM.***

### **3.9. Surface Metallographic Examination**

Polished metallographic samples were prepared to obtain optical micrographs of the microstructure. Spare tensile bars for each material configuration were first sectioned with an Allied TechCut4 low-speed saw equipped with a high-composition diamond blade. Specimens were water-cooled during the sectioning process to prevent excess heat to the surface which may impact the microstructure. Samples were then mounted in PolyFast phenolic hot mounting resin with carbon filler by hot-pressing the sample and resin with a 1-inch diameter Struers CitoPress mounting press.

After mounting, the metallographic specimens were wet-sanded beginning with 240 grit paper and ending with 600 grit paper. The samples were then polished on a rotating polishing surface with a solution of 9  $\mu\text{m}$  polycrystalline diamond suspension and silica solution containing 20% hydrogen peroxide ( $\text{H}_2\text{O}_2$ ). This was followed by polishing with 3  $\mu\text{m}$  diamond suspension and 10%  $\text{H}_2\text{O}_2$  solution and then 1  $\mu\text{m}$  diamond suspension. Final polishing was performed with a Vibromet vibratory polisher for a period of 12-16 hours. After a thorough cleaning with distilled water followed by a rinse with a 90% ethanol solution, the specimens were lightly etched with Keller's Etch containing 2.5% nitric acid ( $\text{HNO}_3$ ), 1.5% hydrochloric acid ( $\text{HCl}$ ), and 1% hydrofluoric acid ( $\text{HF}$ ) in a solution of distilled water. The purpose of the etching is to increase the visibility of the grain boundaries within the microstructure when viewed under an optical microscope. A photograph of a polished and etched metallographic specimen is shown in Figure 18.

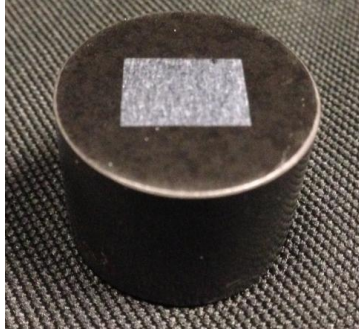


***Figure 18. Polished and etched metallographic specimen.***

Optical micrographs from the polished and etched metallographic specimens were obtained with a Zeiss Observer.Z1m inverted microscope shown in Figure 19. The Observer.Z1m was equipped with a 6-position rotating turret with Epiplan objective lenses ranging from 1.25 $\times$  to 20 $\times$  magnification. Internal optics provided an additional 10 $\times$  magnification allowing for an overall magnification range of 12.5 $\times$  to 200 $\times$ . Optical micrographs for this study were obtained at 50 $\times$  and 100 $\times$  magnifications using the 5 $\times$  and 10 $\times$  objective lenses. Images were captured with an AxioCam MRc5 digital camera attached to the microscope. In addition to optical micrographs, SEM micrographs were obtained with secondary electron detection by the FEI Quanta 600F SEM.



***Figure 19. Zeiss Observer.Z1m inverted microscope.***

## IV. Results and Analysis

### 4.1. Inspection of Manufactured Test Specimens

A total 20 tensile and 65 fatigue specimens were produced on three separate build plates. In addition to the variation in layer thickness of 60  $\mu\text{m}$  in Build 1 and 30  $\mu\text{m}$  for builds 2 and 3, there was variation in the dimensional accuracy of the as-manufactured specimens with respect to the nominal dimensions specified by the CAD drawing. For builds 2 and 3, dimensional accuracy was further affected by the need to remove additional material along one edge of the specimens with a CNC mill during post-processing. The CNC machining was required to remove residual support material remaining after the initial removal from the build plate by the wire-EDM process.

Widths and thicknesses of each specimen were measured to the nearest 0.0001 inch using a micrometer. Lengths were measured to the nearest 0.0005 inch using digital calipers. Measurements on tensile specimens were collected at 18 points labeled A through R in Figure 20. Measurements on fatigue specimens were collected at 16 points labeled A through P in Figure 21. Each specimen was tracked with a unique 2-digit identification number hand-engraved at the top and bottom of each specimen. A summary of the dimensional measurements is shown in Table 8. Units in Table 8 are shown in millimeters (mm). Measurements of width and thicknesses are reported to the nearest 0.005 mm to stay within the 0.00254 mm (.0001 inch) precision of the micrometer. Measurements of length are reported to the nearest 0.01 mm in accordance with the 0.0127 mm (0.0005 inch) precision of the digital calipers.

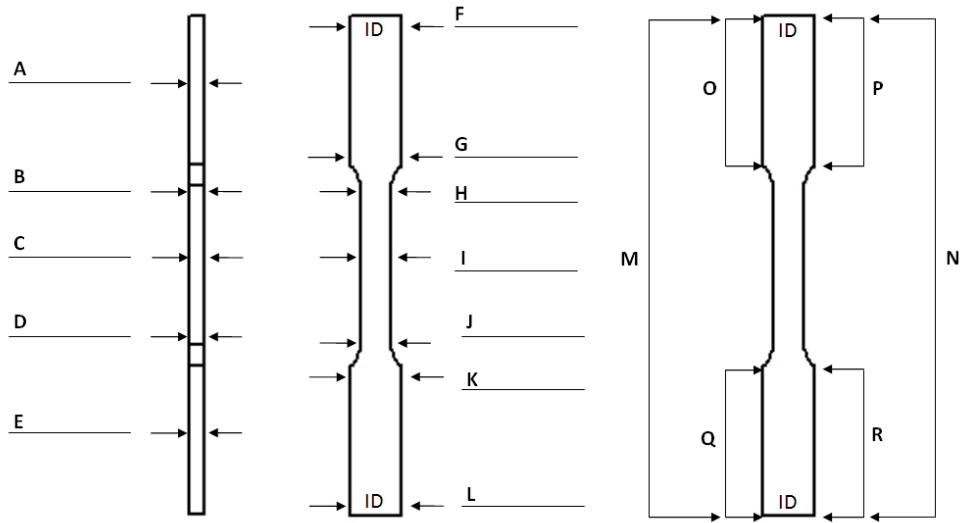


**Figure 20. Tensile specimen measurement points.**

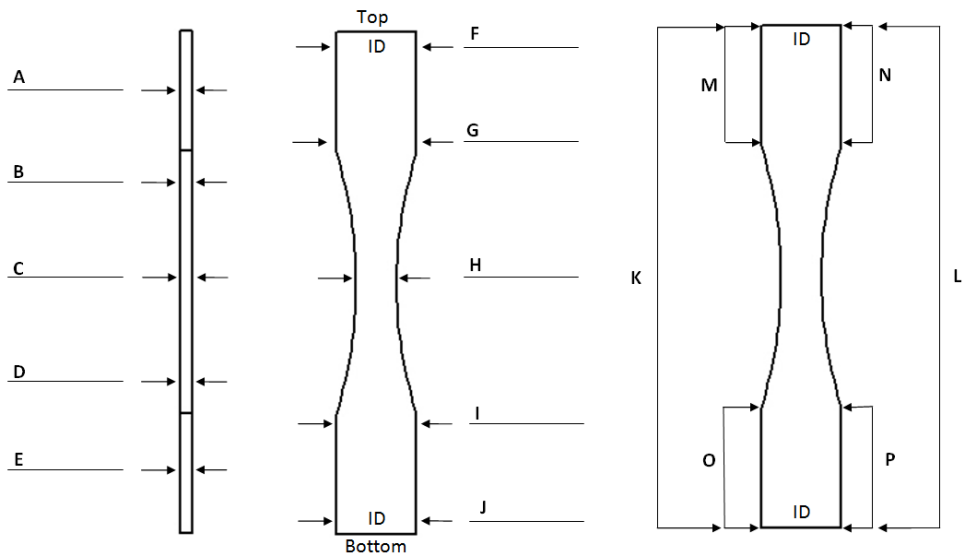


**Figure 21. Fatigue specimen measurement points.**

Table 8. Summary of specimen measurements.

		Fatigue Specimens		Tensile Specimens	
		Build 1	Build 2/3	Build 1	Build 2/3
Overall Length (mm)	<i>Nominal</i>	125	125	100	100
	<i>Min</i>	125.62	124.82	100.55	99.94
	<i>Max</i>	125.72	124.96	100.65	99.97
	<i>Avg</i>	125.68	124.91	100.58	99.96
	<i>StdDev</i>	0.03	0.05	0.03	0.02
Grip Width (mm)	<i>Nominal</i>	20	20	10	10
	<i>Min</i>	19.120	18.595	9.970	8.980
	<i>Max</i>	20.170	19.005	10.165	9.170
	<i>Avg</i>	19.800	18.815	10.075	9.070
	<i>StdDev</i>	0.295	0.090	0.065	0.025
Reduced Width (mm)	<i>Nominal</i>	10	10	10	10
	<i>Min</i>	9.650	10.185	6.075	6.085
	<i>Max</i>	9.955	10.365	6.175	6.135
	<i>Avg</i>	9.855	10.285	6.125	6.070
	<i>StdDev</i>	0.065	0.070	0.020	0.015
Thickness (mm)	<i>Nominal</i>	3	3	3	3
	<i>Min</i>	3.495	3.335	3.485	3.325
	<i>Max</i>	3.570	3.355	3.550	3.385
	<i>Avg</i>	3.530	3.350	3.515	3.355
	<i>StdDev</i>	0.015	0.015	0.015	0.015

From Table 8, the average lengths of the as-manufactured Build 1 fatigue specimens are within 0.7 mm of the nominal 125 mm length. Average grip widths of the Build 1 fatigue specimens are within 0.2 mm, average reduced widths are within 0.15 mm, and average thicknesses are within 0.53 mm of their nominal dimensions. The Build 2/3 fatigue specimens show slightly improved dimensional accuracy in the length and thickness dimensions compared to the Build 1 specimens with average overall lengths within 0.1 mm and average thicknesses within 0.35 mm. Although the data for the Build 2/3 fatigue specimens indicates a 1.185 mm average variation from the nominal grip width, the reduced accuracy is primarily attributed to the additional material

removed by the CNC mill during post-processing. Due to slight warpage of the specimens, additional solid material was removed from the wire-EDM side of the grip areas to machine a flat reference plane. The reference plane was then used to guide light sanding applied to the wire-EDM side of the reduced area region to remove residual support material while preserving the same radius of curvature for the reduced width profile. Figure 22 shows a visual reference of the amount of material removed by the CNC mill with respect to the as-manufactured profile of a fatigue specimen from Build 1.



***Figure 22. Photograph of fatigue specimens illustrating the asymmetric shape of the Build 2/3 specimen (shown in front) grip areas against the profile of a Build 2 specimen (shown in rear) resulting from the removal of residual support material and machining of a flat reference plane.***

In Figure 22, it is shown the removal of material from only one side of the specimen resulted in an asymmetrical shape of the grip areas with respect to the line of symmetry for the reduced area test section. Since the radius of curvature for the reduced area was preserved, the symmetry of the reduced area test section was minimally affected. As seen in Figure 22, the geometry of the test section in the Build 2/3 fatigue specimen approximately matches the as-manufactured geometry of the Build 1 specimen mated immediately behind the Build 2/3 specimen in the photograph. However, it is apparent a greater amount of material was removed from the left side of the specimen in the photograph compared to the amount of material removed from the right side. This

resulted because the reference plane established by the CNC mill was designed as parallel to the nominal axis of symmetry for the test section. Due to warpage of the substrate plate occurring during the SLM process, the as-manufactured axis of symmetry was not a straight line. Therefore, the CNC mill removed a disproportional amount of material along the length of the specimen as seen in Figure 22. During tensile and fatigue testing, specimens were carefully aligned with the axis of symmetry for the reduced area test section to minimize the effects of the asymmetrical grip area of the Build 2/3 specimens. While the asymmetry increased the amount of effort to ensure proper alignment, the design of the reduced area test section is intended to create a uniform stress distribution over the cross section during axial loading. Therefore, the asymmetrical grip areas are not expected to impact the test results since the reduced area test section remained symmetrical and relatively consistent between individual specimens.

The warpage of the substrate plate occurred in all three builds. During removal of the specimens from the substrate plate, the CNC of the wire-EDM presumes the surface of the substrate plate is true (i.e. not warped). Since the degree of warpage was not consistent across the length and width of the substrate plate, the specimens were cut from the substrate plate at slightly varying widths due to asymmetry. A visual reference of the variation of the as-manufactured widths resulting from the warpage of the substrate plate is shown in Figure 23. In Figure 23A, the Build 1 fatigue specimens are stacked in a random order. From this image, it is seen the widths of the grips have a small degree of variation. From the measurement data in Table 8, the Build 1 fatigue specimens have a range of 0.97 mm between the minimum and maximum recorded grip widths with a standard deviation of 0.295 mm. This relatively large standard deviation indicates the

variability of the grip width dimensions are several orders of magnitude larger compared to variation in the length and thickness dimensions which have standard deviations ranging from 0.015 mm to 0.05 mm. When the specimens are rearranged by minimum to maximum width at the tips, the relative position of the specimens on the substrate plate is reproduced as shown in Figure 23B.



A) Randomly stacked specimens



B) Specimens arranged by grip width

**Figure 23. Photographs of Build 1 fatigue specimens stacked together to illustrate asymmetry in the specimen geometry resulting from warped substrate plate.**

Additional discrepancies in the as-manufactured specimens include the difference in build layer thickness between Build 1 and Build 2/3, tool marks from the wire-EDM process, and minor pitting present on the surface of the wire-EDM edge on a limited number of specimens produced in Build 2/3. The Build 1 specimens were produced with a 60  $\mu\text{m}$  layer thickness which exhibits a greater degree of stair-stepping along the curved radius of the reduced area section compared to the degree of stair-stepping observed in the Build 2/3 specimens produced with 30  $\mu\text{m}$  layers. A visual comparison of the stair-stepping in the Build 1 and Build 2/3 fatigue specimens is shown in the optical microscope image in Figure 24. From Figure 24, the Build 2/3 fatigue specimen in the lower half of the photograph has a slightly finer surface appearance than the Build 1

specimen directly above it. Note the darker color of the Build 1 specimen is the result of color distortion and oxidation from the furnace heat treatment.

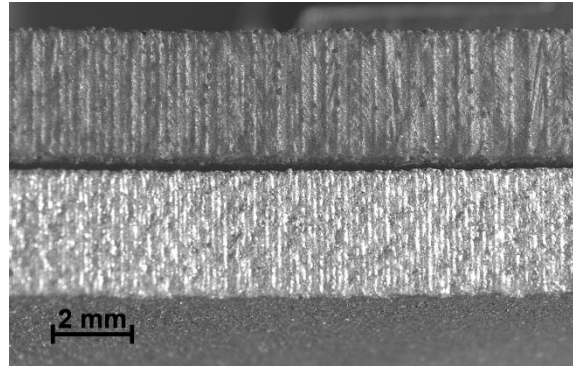


***Figure 24. Optical microscope image taken with a 0.63× objective lens of fatigue specimens illustrating the reduced stair-stepping effect in a Build 2/3 specimen (bottom) with 30 μm layers compared to a Build 1 specimen (top) with 60 μm layers.***

Aside from the difference in stair-stepping effect between the Build 1 and Build 2/3 fatigue specimens, the as-built edges of the fatigue specimens had a uniform appearance with no major defects observed by unaided visual inspection. However, the fatigue specimens from all three builds exhibited tool markings on the wire-EDM edge. An example of a wire-EDM tool mark is shown in Figure 25A. Nearly all fatigue specimens had a characteristic tool mark at the center of the test section at the point of minimum specimen width. Approximately one-half of the fatigue specimens had one to four additional tool markings at other locations along the length of the reduced area curvature. However, none of the fatigue fracture locations corresponded directly with the location of a wire-EDM tool mark. Therefore, these tool markings did not appear to impact the fatigue testing results.

Approximately 25% of the Build 2/3 fatigue specimens exhibited varying degrees of surface pitting on areas of the wire-EDM surface. An example of surface pitting is shown in the photograph of the fractured specimen in Figure 25B. Surface pitting was only observed on the specimens produced in Build 2/3; pitting was not observed on any of the Build 1 specimens. It is suspected the pitting resulted from an interaction with the lower-density support material layers utilized in builds 2 and 3 as opposed to the Build 1 specimens which utilized fully-dense material for support. Two of the HIP-treated fatigue specimens experience cracked initiations originating from the wire-EDM side of the specimen whereas all other fatigue cracks initiated from the as-built edge. In both cases of crack initiation from the wire-EDM side, surface pitting was observed in the vicinity of the crack location as shown in Figure 25B.

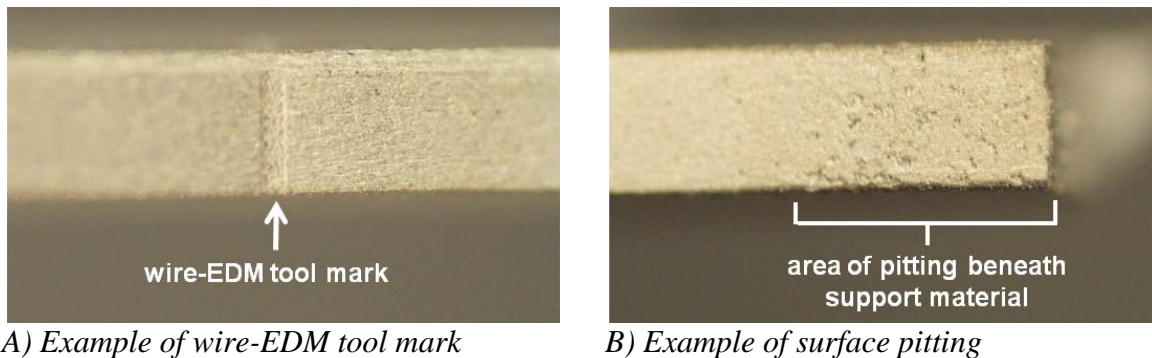


**Figure 25. Photographs of tool mark from wire-EDM (A) and surface pitting (B) remaining after removal of support material.**

#### 4.2. Tensile Test Results

A total of 20 tensile test specimens were produced to determine the static material properties of the SLM Ti-64 produced by the EOSINT M 280. As shown in Table 7, a quantity of 5 tensile specimens from Build 1 were left as-built, 5 specimens from Build 2/3 were HIP-treated, and a total of 10 specimens from Build 1 and Build 2/3 were stress-relieved. Of the 10 stress-relieved specimens, 5 were produced in Build 1 with a 60  $\mu\text{m}$  layer thickness and 5 were produced in Build 2/3 with a 30  $\mu\text{m}$  thickness. Of the 20 total tensile specimens, three were designated for sectioning to provide material for the polished metallographic samples. This reduced the available quantity of tensile specimens to 4-each for the as-built and HIP configurations, and 9 for the stress-relieved configuration (5 from Build 1 and 4 from Build 2/3).

The five stress-relieved specimens from Build 1 were tested first (specimens T-06 through T-10). The results of these tests are shown in the stress versus strain figure in Figure 26. The average modulus of elasticity calculated from this data is 167.2 GPa. Since the expected range of the modulus based on the manufacture's data is 106-126 GPa, a value of 167.2 GPa was suspected as erroneous. Upon further examination of the test setup, it was determined the extensometer was incorrectly calibrated. However, the force values in the test data were determined to be a correct and provide a valid measurement of UTS. To account for the calibration error, a reasonable approximation of the 0.2% offset yield strength was obtained by applying a linear correction factor to the strain data. To provide a data correction, the experimental strain data was multiplied by a factor of 1.49 to obtain an average modulus of 112 GPa in the corrected stress versus

strain curve. The corrected stress versus strain curves for the Build 1 stress-relieved configuration are shown in Figure 27.

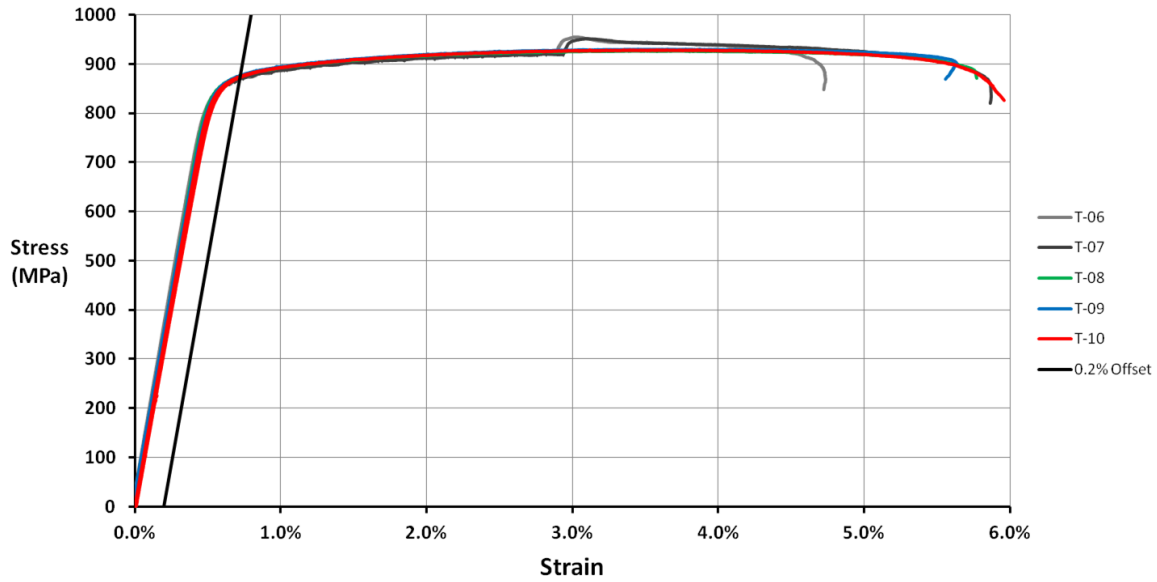


**Figure 26. Original stress vs. strain data for Build 1 (60 μm layer thickness) stress-relieved configuration.**

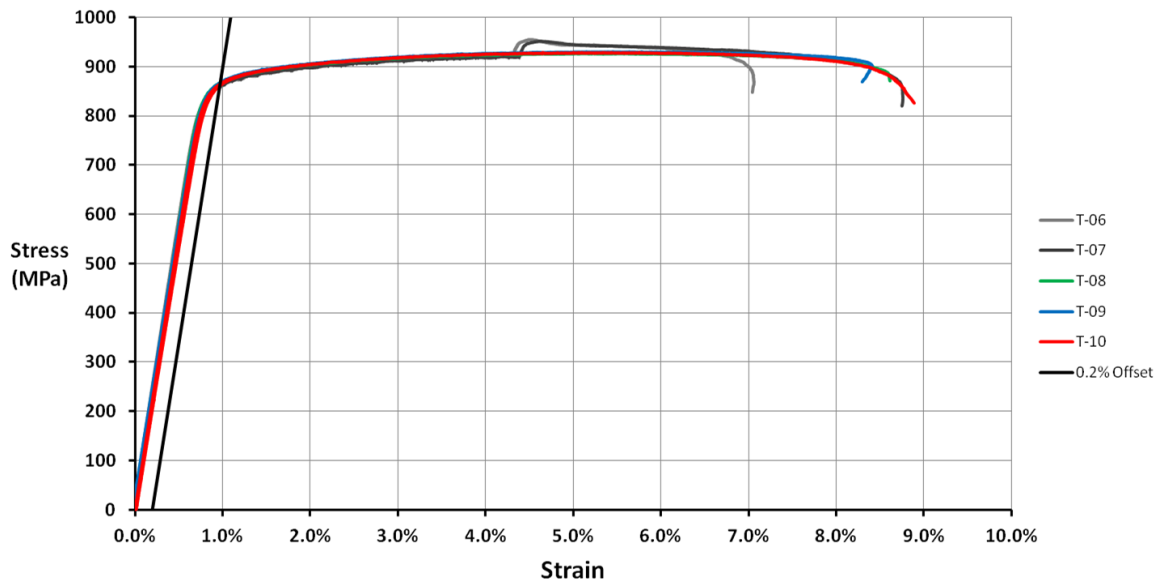


**Figure 27. Corrected stress vs. strain data for Build 1 (60 μm layer thickness) stress-relieved configuration with strain values adjusted for calibration error.**

During testing of specimens T-06 and T-07, the MTS testing machine was programmed to increase the crosshead speed upon reaching a value of 3% strain. The intent of the crosshead speed increase was to shorten the amount of time to achieve complete fracture in accordance with the guidance in ASTM E8/E8M to produce failure within one minute after reaching the yield point of the material. However, as seen in Figures 26-27, the stress versus strain curves for specimens T-06 and T-07 exhibit irregular behavior corresponding to the timing of the rapid increase in strain rate. This behavior resulted in a “bump” in the stress versus strain curve and appears to overstate the indicated UTS. The programmed increase in crosshead speed was removed for all subsequent tests to prevent this occurrence. Since the crosshead speed was consistent between all individual tests prior to reaching 3% strain, the data for the linear-elastic region of specimens T-06 and T-07 remains a valid test of the stress versus strain behavior through the yield point. Therefore, the data from specimens T-06 and T-07 are included in the calculation of the average yield strength and excluded from calculation of the average UTS for the Build 1 stress-relieved configuration.

The tensile testing results for the remaining specimens are shown in Figure 28 and Table 9. Prior to these tests, the extensometer was re-calibrated and therefore correction of the experimental strain data was not required. Four tests were accomplished for each of the as-built, stress-relieved, and HIP-treated configurations. Inspection of the experimental data indicated each configuration had one of the four tests exhibit inconsistent stress versus strain behavior compared to the consistency of the three remaining tests. The observed inconsistencies were the result of excessive noise in the recorded force data. To eliminate the inconsistent tests during data analysis,

experimental data from specimens T-02 (HIP), T-12 (stress-relieved), and T-17 (as-built) were discarded due to the excessive noise in the recorded force data during these tests. As seen in Figure 28, the three remaining tests for each configuration produced consistent results with nearly superimposed stress versus strain curves produced by the specimens within a single configuration. Due to unreliable indications of the elongation at break recorded by the extensometer, the data range in Figure 28 is limited to a strain value of 6%. Values for the average UTS, YS,  $\epsilon_f$ , and E are shown in Table 9. Percent elongation reported in Table 9 is based on the gauge length after fracture measured from optical microscope images of the gauge-length markings. The UTS and YS data for the Build 1 stress-relieved specimens are included in Table 9 for a comparison of material properties between 30  $\mu\text{m}$  and 60  $\mu\text{m}$  build layer thicknesses.

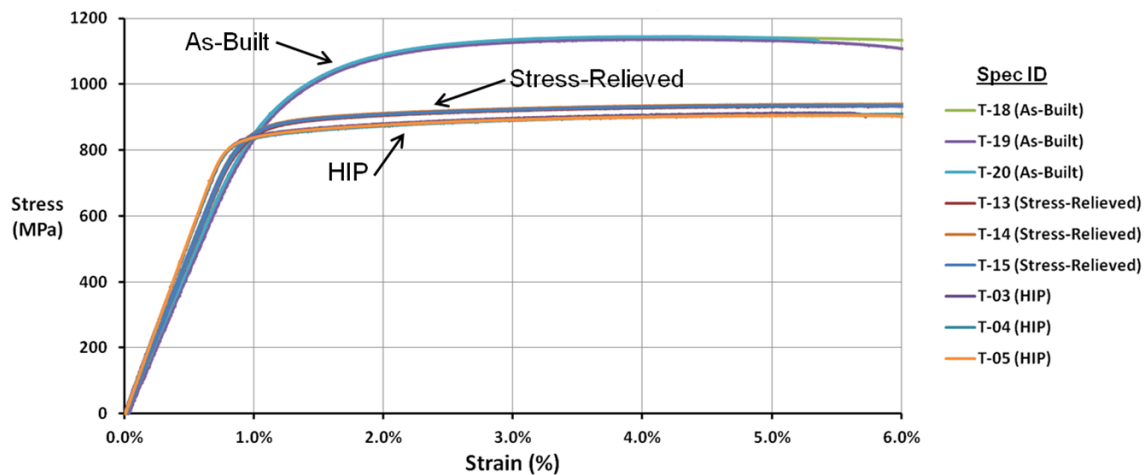


**Figure 28. Stress vs. strain plot for the as-built (Build 2/3, 30  $\mu\text{m}$  layer thickness), stress-relieved (Build 2/3, 30  $\mu\text{m}$  layer thickness), and HIP-treated (Build 1, 60  $\mu\text{m}$  layer thickness) configurations.**

**Table 9. Static tensile properties for the as-built, stress-relieved, and HIP-treated configurations with indicated build layer thicknesses.**

	<b>As-Built (30 <math>\mu\text{m}</math> layers)</b>	<b>Stress-Relieved (30 <math>\mu\text{m}</math> layers)</b>	<b>Stress-Relieved (60 <math>\mu\text{m}</math> layers)</b>	<b>HIP (60 <math>\mu\text{m}</math> layers)</b>
<b>UTS <math>\pm</math> STD (MPa)</b>	1140.7 $\pm$ 5.0	936.9 $\pm$ 3.6	928.3 $\pm$ 2.3	910.1 $\pm$ 2.9
<b>YS <math>\pm</math> STD (MPa)</b>	938.2 $\pm$ 7.7	862.4 $\pm$ 3.1	862.0 $\pm$ 4.0	835.4 $\pm$ 3.8
<b><math>\epsilon_f</math> (%)</b>	6.7 $\pm$ 1.0	11.4 $\pm$ 0.8	9.6 $\pm$ 0.6	7.2 $\pm$ 1.0
<b>E <math>\pm</math> STD (GPa)</b>	91.8 $\pm$ 0.5	98.0 $\pm$ 1.2	NA	106.8 $\pm$ 1.3

Based on the tensile results in Table 9, stress relief reduced the UTS by approximately 18%, reduced YS by 8%, and increased  $\epsilon_f$  by 2.9% in the Build 2/3 material compared to the as-built material. HIP had a slightly greater impact with a reduction in UTS of approximately 20%, reduction in YS of 11%, and increase in  $\epsilon_f$  by 0.5% compared to the as-built material. Based on the data for the stress-relieved configuration, a change in layer thickness from 30  $\mu\text{m}$  to 60  $\mu\text{m}$  had a marginal impact of less than 1% on UTS and YS. However, the experimental data indicates the average elongation at break for specimens with 60  $\mu\text{m}$  build layers was only 9.6% compared to the average of 11.4% elongation at break for the specimens with 30  $\mu\text{m}$  build layers. The difference in observed elongation at break between the 30  $\mu\text{m}$  and 60  $\mu\text{m}$  layer thicknesses may result from a combination of contributing factors including variation within the experimental data, potential differences in processing between the two separate lots of furnace heat-treatments, or microstructural effects of the different layer

thicknesses. Based on the experimental data, the difference in build layer thickness of 30  $\mu\text{m}$  or 60  $\mu\text{m}$  has a marginal effect on static material properties.

### **4.3. Fatigue Test Results**

The results of fatigue testing were used to produce stress-life curves for the stress-relieved and HIP-treated configurations. Since the stress-relieved specimens are divided among three separate build plates manufactured with a 60  $\mu\text{m}$  layer thickness in Build 1, and 30  $\mu\text{m}$  layer thickness in Build 2/3, the Build 1 and Build 2/3 stress-relieved specimens were initially treated as separate populations. Treating the Build 1 and Build 2/3 specimens as separate populations allows for a comparison of stress-life behavior to determine if a difference in behavior is present in the data. However, when treated separately, the stress-life curve for each population is determined with a reduced number of specimens. Additionally, the quantity of stress-relieved specimens is not evenly divided between the builds with 19 stress-relieved specimens produced in Build 1 and only 11 produced in Build 2/3. As a result of the reduced and uneven population sizes for the stress-relieved specimens, the stress-life comparison for the individual populations of Build 1 and Build 2/3 specimens has a reduced statistical confidence.

The mean fatigue life was determined using staircase data consisting of seven data points for the Build 1 (60  $\mu\text{m}$  build layer thickness) stress-relieved configuration and five data points for the Build 2/3 (30  $\mu\text{m}$  build layer thickness) stress-relieved configuration. The staircase data for the Build 1 and Build 2/3 stress-relieved configuration is shown in Figure 29. Although seven data points are shown in Figure 29B for the Build 2/3 specimens, the first two data points at 240 MPa and 230 MPa were excluded from the mean and standard deviation calculations. This exclusion was made on the basis the

initial two failures occurred outside the range of the subsequent staircase data points. The staircase data was analyzed using the Dixon-Mood equations shown in equations (9-11). For the Build 1 stress-relieved configuration, the majority of specimens in the staircase data are survivals. Therefore,  $i = 0$  corresponds to the lowest stress-level at which a failure was observed as shown in Figure 29A. For the Build 2/3 stress-relieved configuration, the majority of specimens in the staircase data are failures, and  $i = 0$  corresponds to the lowest stress-level at which a run-out was observed as shown in Figure 29B. Although only a single run-out was observed for the Build 2/3 stress-relieved configuration, additional test specimens were not available to perform more staircase tests. From equations (9-11),  $\bar{\mu} = 232$  MPa and  $\bar{\sigma} = 5.3$  MPa for the Build 1 stress-relieved specimens and  $\bar{\mu} = 218$  MPa and  $\bar{\sigma} = 5.3$  MPa for the Build 2/3 stress-relieved specimens. Based on these results, the mean fatigue life of Build 2/3 is approximately 6% lower than Build 1.

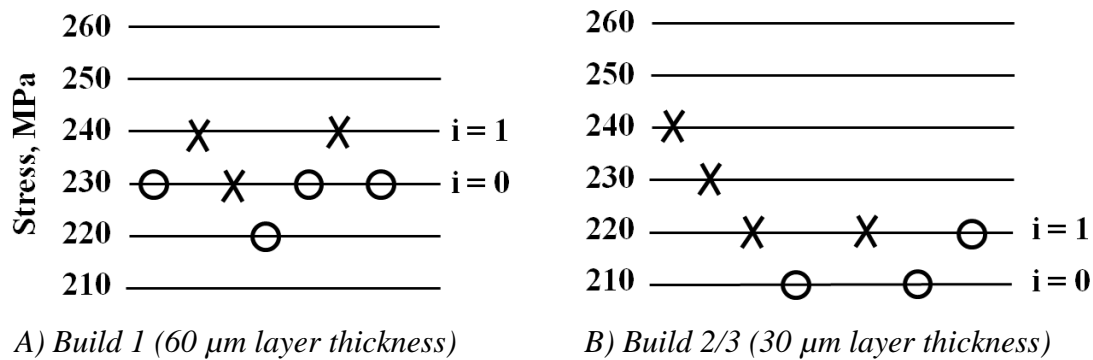


**Figure 29. Staircase data for stress-relieved configuration separated by build where symbol 'X' denotes a failure and 'O' denotes a run-out.**

The fatigue testing data points for the stress-relieved configuration are shown in the stress-life plot in Figure 30. In Figure 30, the Build 1 and Build 2/3 stress-relieved specimens are segregated as separate populations. Stress-life curves were generated from a linear regression of the data points at maximum stress levels greater or equal to 300 MPa. The horizontal asymptote corresponds to the mean fatigue life calculated from the staircase data. The stress-life curves in Figure 30 show minimal differences between the Build 1 and Build 2/3 stress-relieved specimens in the finite-life region at stress levels above the mean fatigue life. Although the Build 1 specimens have a slightly steeper stress-life slope of -108.7 MPa per log cycle compared to the Build 2/3 stress-life slope of -98.0 MPa per log cycle based on the linear regression, the data points follow the same general linear trend. Additionally, the perceived difference in slopes is potentially influenced by the fact experimental data was not collected at the 500 MPa maximum stress level for the Build 2/3 specimens. Since both the finite-life region and the mean fatigue life are similar between the Build 1 and Build 2/3 specimens, it is reasonable to treat the stress-relieved experimental data as a single population.

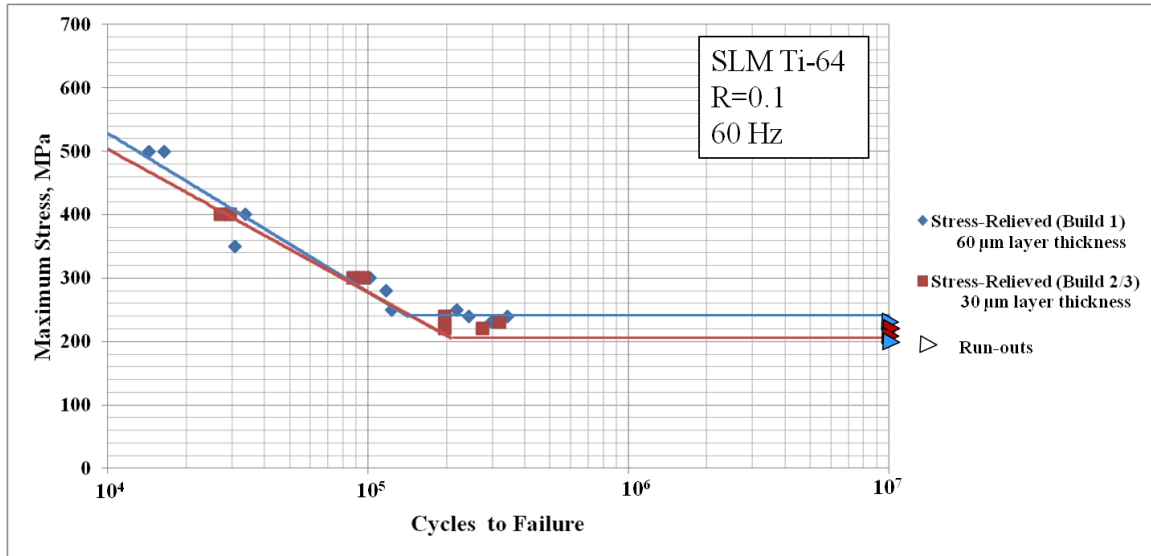


**Figure 30. S-N plot for stress-relieved configuration with Build 1 (60 μm layers) and Build 2/3 (30 μm layers) presented as separate populations.**

The finite-life region of the stress-life curve for the HIP-treated configuration was determined by testing a series of three specimens each at 300 MPa, 400 MPa, and 500 MPa maximum stress levels. To provide an initial estimate of the mean fatigue life for the starting stress level of the staircase testing, an accelerated test method was performed on a single specimen. Under the accelerated test method, a specimen was run at a starting maximum stress level of 230 MPa for a shortened test run-out of  $10^6$  cycles. After completion of each set of  $10^6$  cycles, the maximum stress level was increased by 10 MPa and the same specimen was re-run for an additional  $10^6$  cycles. This specimen was run for  $10^6$  cycles at maximum stress levels from 230 MPa to 260 MPa and then failed after 468,000 cycles at the 270 MPa stress level. The staircase testing was then continued with a new specimen at 260 MPa using the full test run-out of  $10^7$  cycles. The staircase data points for the HIP-treated configuration are shown in Figure 32. Applying equations (9-11) to the staircase data in Figure 31 results in  $\bar{\mu} = 235$  MPa and  $\bar{\sigma} = 13.4$  MPa.

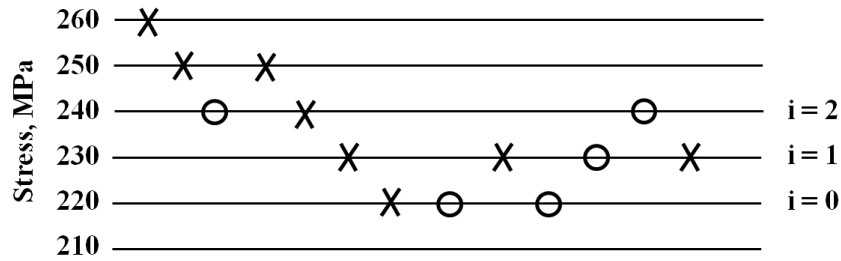


**Figure 31. Staircase data for HIP-treated configuration where symbol ‘X’ denotes a failure and ‘O’ denotes a run-out.**

After completion of 13 staircase data points, survivals to  $10^7$  cycles were not observed above 240 MPa. For the staircase data points, failure of specimens occurred within  $10^6$  cycles in all but a single case which failed at  $1.41 \times 10^6$  cycles. Therefore, the specimen surviving to  $10^6$  cycles at a stress level of 260 MPa using the accelerated test method is likely an anomaly. It is possible the repeated cycles at lower stress levels influenced the results. Additional testing using the accelerated method is required to confirm whether there is an impact on fatigue life when specimens are first subjected to fatigue loads at lower stress levels for several million cycles. To eliminate the possibility of influencing the data analysis with an inconsistent data point obtained using the accelerated test method, this data point was removed from the data set.

The stress-life data for the HIP-treated configuration and the stress-relieved configuration are shown in Figure 32. In Figure 32, the Build 1 and Build 2/3 stress-relieved specimens are treated as a single population. The linear region of the stress-life curves are determined by linear regression of the data points greater or equal to 300 MPa. The horizontal asymptote corresponds to the mean fatigue life calculated from the staircase data. For the combined stress-relieved configuration staircase data, applying equations (9-11) results in  $\bar{\mu} = 226$  MPa and  $\bar{\sigma} = 11.7$  MPa. From these results, the

experimental mean fatigue life for the combined stress-relieved configuration is only 9 MPa, or 3.8%, lower than the experimental mean fatigue life of the HIP-treated configuration. From Figure 32, it is seen the slopes for the stress-life curves in the finite-life region are approximately equal. From the linear-regression, the combined stress-relieved specimens have a slope of -106.4 MPa per log cycle and the HIP-treated specimens have a slope of -99.0 MPa per log cycle. However, the stress-life curve for the HIP-treated specimens is shifted to the right indicating the HIP-treated specimens have a higher fatigue life at stress levels above the mean fatigue life. A comparison of the average number of cycles to failures based on the experimental data points at 300 MPa, 400 MPa, and 500 MPa is provided in Table 10. From Table 10, HIP-treated specimens exhibited an average fatigue life increase of 61.4% at 500 MPa and a 102% average increase at 300 MPa.

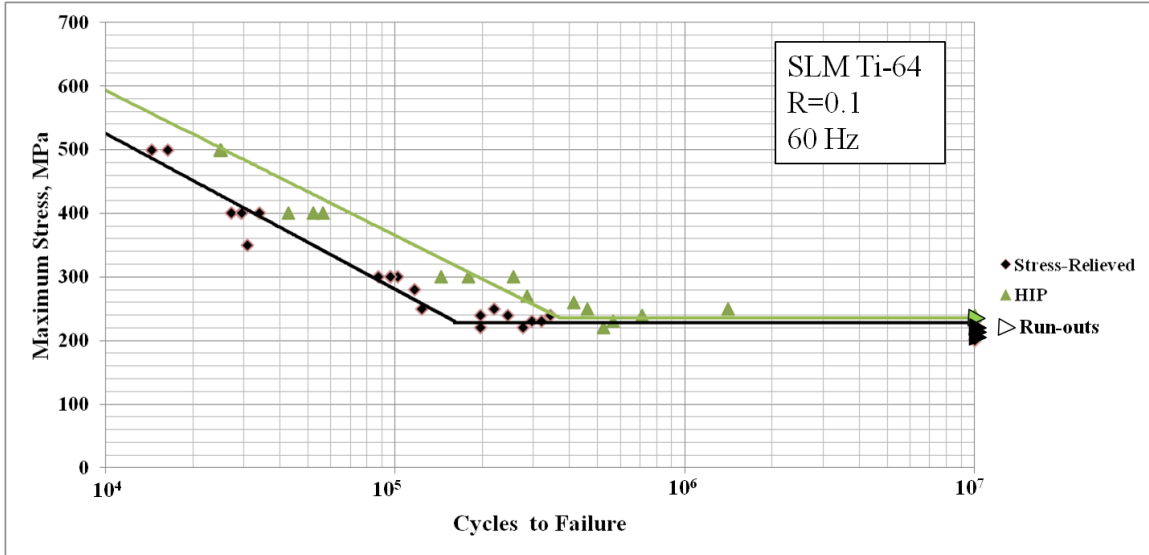


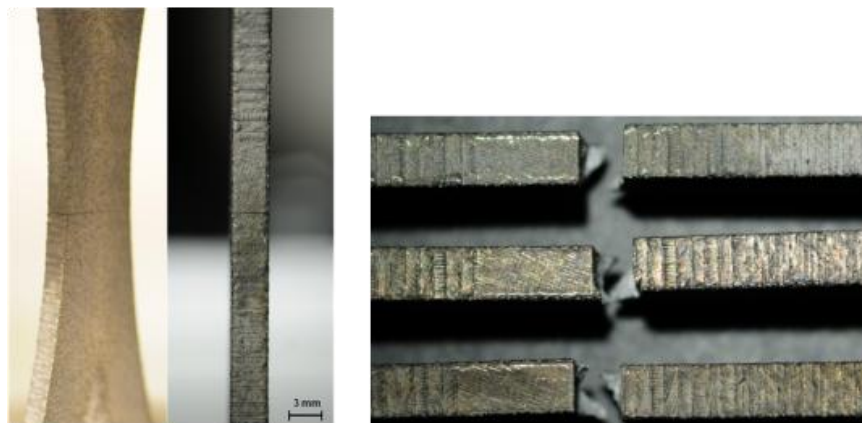
**Figure 32.** S-N Plot for stress-relieved and HIP configurations where stress-relieved specimens from Build 1 and Build 2/3 are treated as a single population.

**Table 10.** Comparison of the average number of cycles to failure for the stress-relieved and HIP configurations.

Max Stress (MPa)	Average #Cycles to Failure		% Increase
	Stress-Relieved	HIP	
300	95,550	193,143	102 %
400	30,173	50,326	66.8 %
500	15,449	24,929	61.4 %

#### 4.4. Examination of Fracture Surfaces

With the exception of two HIP-treated specimens, fatigue failures were observed to initiate from the as-built edge of the specimens. An example of a typical fatigue crack location is shown in the photograph of a partially-cracked specimen in Figure 33A. As shown in Figure 33B, the crack location coincides with the boundary of the small flat area at the center of test section and the first ridge of the stair-step region. The highest value of nominal stress occurs at the center of the test section where the area of the cross-section is at a minimum. However, stress concentrations created by the stair-step ridges increases the localized stresses experienced by the material surrounding these ridges. Depending on the magnitude and location of the stress concentration factor, the maximum value of localized stress may occur at a different location from the expected location of maximum nominal stress. None of the specimens were observed to have a crack initiation within the small flat region at the center of the specimen corresponding to the location of minimum cross-section. This suggests the stress concentrations created by the stair-step ridges are a significant influence on the location of crack initiation.



A) Partially-cracked specimen B) Series of specimens with same crack location

**Figure 33. Typical fatigue crack location in a stress-relieved specimen initiating from the as-built edge of the specimen.**

A representation of a typical fatigue fracture surface is shown in the optical microscope image in Figure 34. From Figure 34, the crack-propagation region is seen on the right-hand side of the image as the crack propagates over the cross-sectional plane of the specimen from right to left in the orientation shown. As the crack plane propagates, the remaining un-cracked material ahead of the crack must support the applied axial loads. Therefore, the effective applied stress in the un-cracked region increases as the crack length increases. As the applied stress approaches the ultimate strength of the material, an overload condition causes the material to yield resulting in a ductile failure of the material.

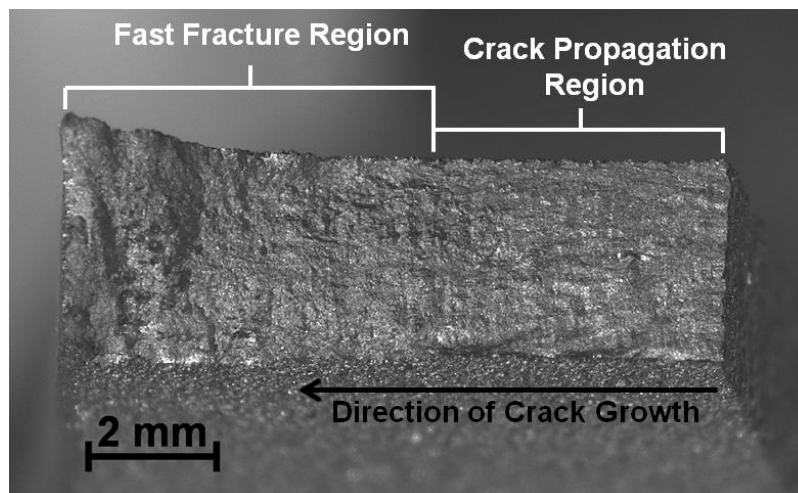


***Figure 34. Optical microscope image at 12 $\times$  magnification with 0.63 $\times$  objective lens showing the fatigue fracture surface of a HIP specimen (F-41) indicating the direction of crack growth, crack propagation region, and fast fracture (overload) region.***

In Figure 34, the smoother crack propagation region transitions to the fast fracture, or overload, region as the crack front approaches the midpoint of the cross section. The point at which this transition occurs is dependent on the maximum applied stress level of the cyclic loading. Lower stress levels near the endurance limit results in a longer crack

propagation region whereas at higher stress levels, transition to fast fracture occurs at shorter crack lengths. SEM imaging of the fast fracture region reveals the presence of ductile dimples indicative of plastic deformation during final failure. SEM images of ductile dimples observed in the overload region are shown in Figure 35.

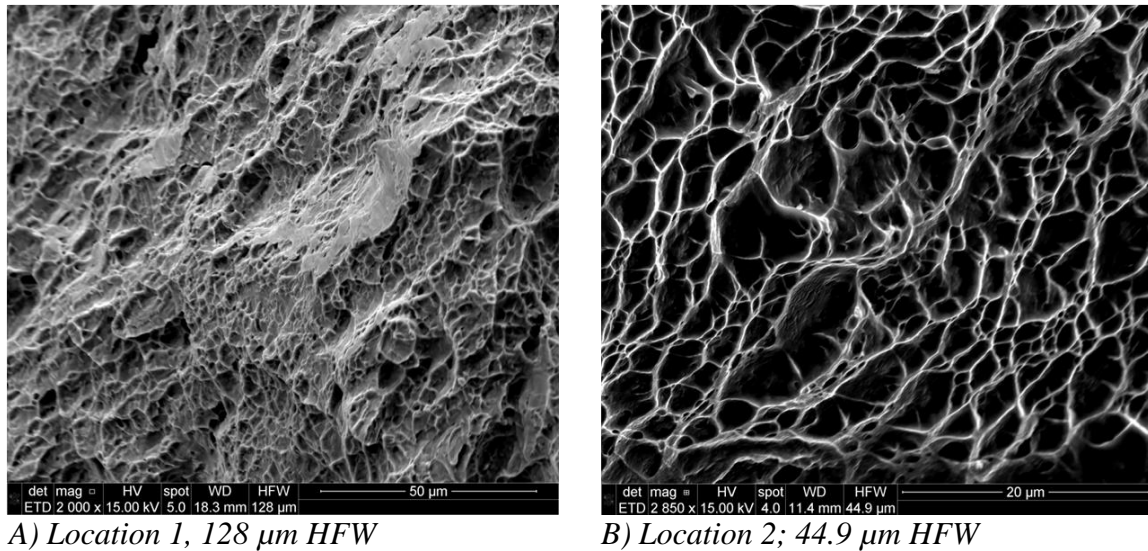
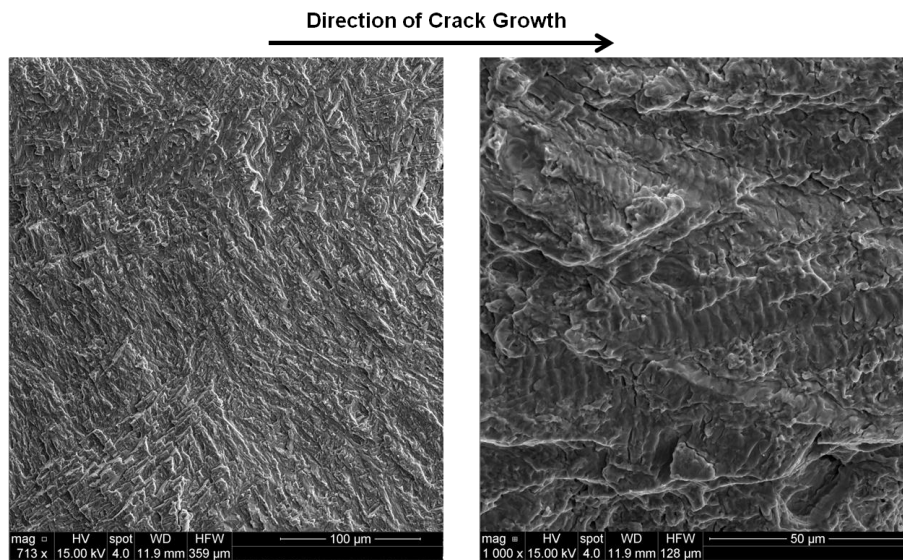


**Figure 35. SEM images of the fast fracture region in a stress-relieved specimen (F-14) showing ductile dimpling.**

The crack propagation region has a smoother surface appearance than the surface of the fast fracture region as shown in Figure 36. The typical appearance of the crack propagation surface is shown in the SEM image in Figure 36A. The appearance of the crack propagation surface was generally uniform in appearance between individual specimens and configurations. Most areas of the crack propagation surface lacked visible fatigue striations. Fatigue striations are markings often visible on fatigue fracture surfaces when the surface is viewed at high magnification such as by SEM. Striations are formed by plastic deformations caused by the blunting and re-re-sharpening of the crack tip during each cycle of loading and unloading [72]. Such striations are indicative of

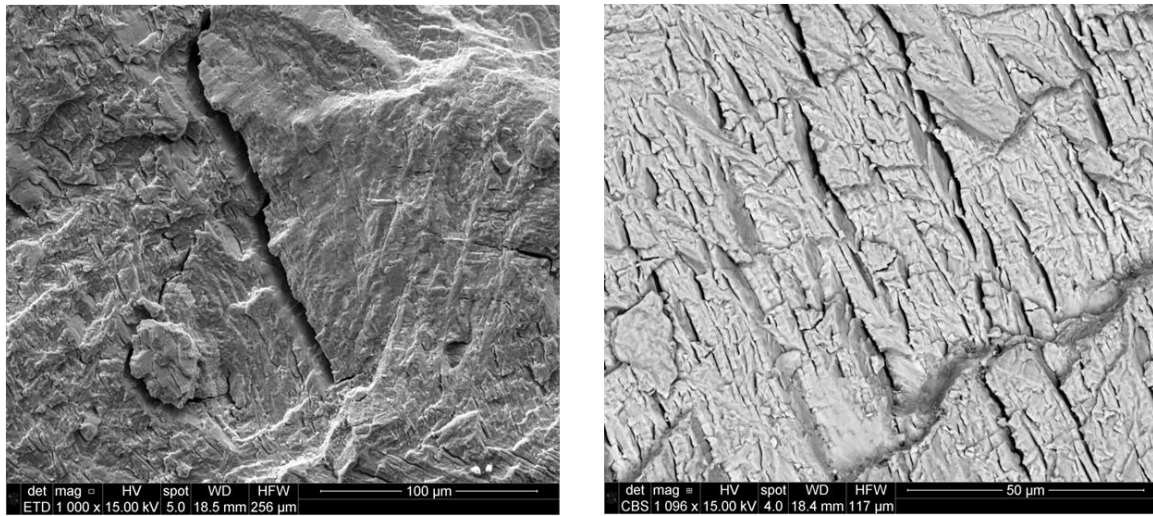
fatigue crack growth in many metal materials. Due to their typical bowed appearance, striations are used to identify the direction and origin of crack growth. However, as noted in Milella, it is common for Ti-64 fatigue surfaces to exhibit only small areas of striations separated by regions lacking any typical signs of fatigue [72]. An example of a region where striations are visible is shown in Figure 36B. As seen from this image, the striations correspond to the direction of crack growth. Since the majority of the fracture surfaces lacked visible striations, it was not possible to rely on striations to trace the origin of the crack initiation. However, based on the macroscopic surface appearance, all fatigue cracks appear to have originated from the surface of the specimen. No visible signs were observed indicating crack initiation from internal voids or pores such as those observed in previous studies by Rafi *et al.* and Leuders *et al.* [15, 36].



A) Typical surface with no visible striations      B) Region with visible striations

**Figure 36. SEM images of smooth fracture region in a stress-relieved specimen (F-14) showing (A) typical surface appearance without striations visible at 359  $\mu\text{m}$  HFW and (B) region with visible striations at 128  $\mu\text{m}$  HFW.**

Areas of secondary cracks on the fracture surface were observed on several of the examined fatigue fracture surfaces. Two examples of secondary cracks observed in fatigue specimens are shown in the SEM images in Figure 37. Figure 37A shows a larger secondary crack measuring several micrometers in width whereas Figure 37B shows an area of multiple smaller secondary cracks. The image in Figure 37B was captured using an electron back-scatter detector which enhances the visibility of the secondary cracks. As discussed in Milella, secondary cracks are formed by local stress states on a plane perpendicular to the direction of the primary crack propagation [72].



A) Location 1; secondary electron image

B) Location 2; electron back-scatter image

**Figure 37. SEM images of fatigue fracture surface showing secondary cracking from fatigue damage accumulation in a stress-relieved specimen (F-11).**

In several of the examined specimens, defects were observed both on the surface of the specimen and within the internal region of the fracture surface. Figure 38 shows an internal defect noted during optical examination of specimen F-10 (stress-relieved configuration). The defect measures approximately 0.1 mm in width and 0.3 mm in length. As seen in Figure 38B, the location of the defect is relatively close to the as-built

edge of the specimen. Specimen F-10 failed at a stress-level of 240 MPa after approximately 240,000 cycles. Two additional stress-relieved specimens tested at the same stress level failed after approximately 197,000 cycles and 342,000 cycles. Examination of the specimen F-10 fracture surface by SEM revealed no other abnormalities. Due to the lack of identifiable crack initiation site characteristics on the fracture surface, it was not determined whether the internal defect in specimen F-10 impacted the fatigue life of this specimen.

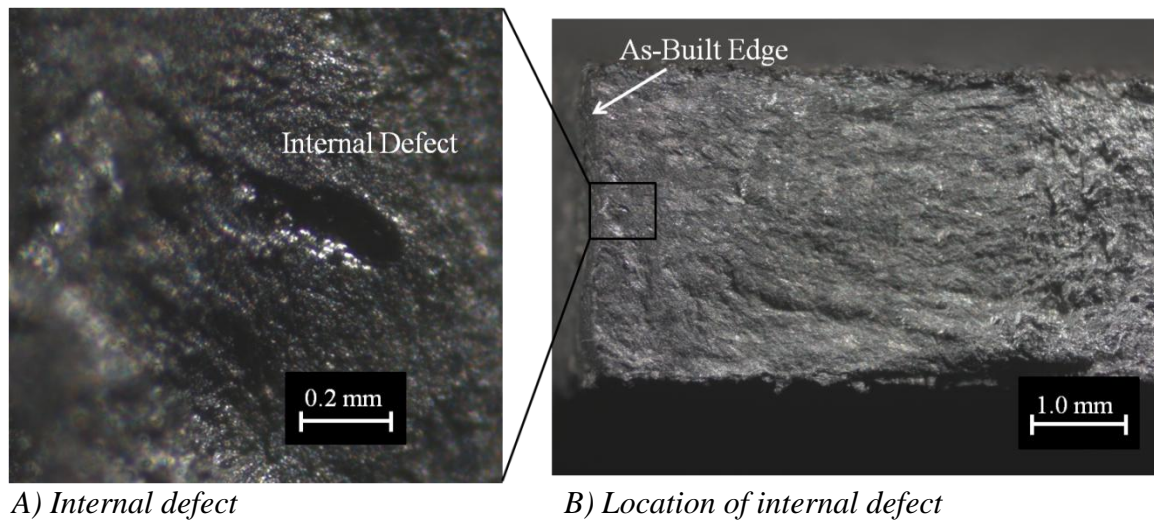


**Figure 38. Optical microscope images of an internal defect on the fatigue fracture surface of a stress-relieved specimen (F-10).**

A surface defect observed during SEM examination of specimen F-11 is shown in Figure 39. The defect has a width of 120  $\mu\text{m}$  at a depth of 60  $\mu\text{m}$  beneath the external surface of the specimen. Of note, specimen F-11 (stress-relieved) failed at a stress level of 230 MPa after 290,000 whereas the three other stress-relieved specimens from Build 1 tested at the same stress level survived until test run-out at  $10^7$  cycles. From Figure 39A, it is seen the immediate surface surrounding the surface defect has several faceted layers. The appearance of the fracture surface suggests the fatigue crack initiated from the

surface defect. It is suspected the stress concentration caused by the surface defect interacted with the stress concentration from the corner of the specimen to cause premature failure compared to the other three stress-relieved Build 1 specimens that did not fail during testing at the same stress level.

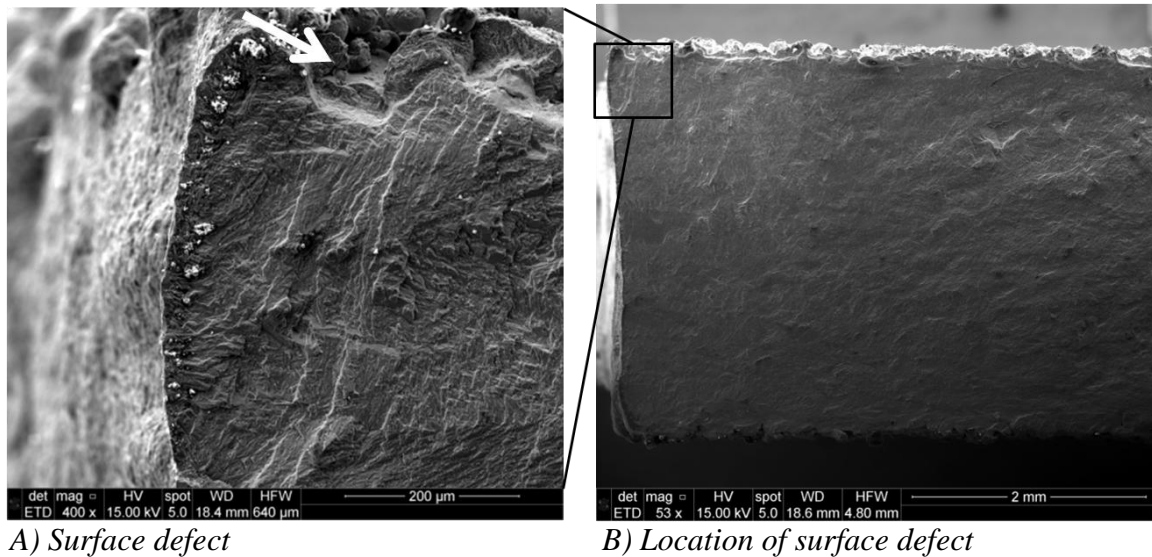


**Figure 39. SEM images of a surface defect in a stress-relieved specimen (F-11) indicating a possible fatigue crack initiation site.**

Two of the HIP-treated specimens had crack-initiation sites originating from the wire-EDM side of the specimen as opposed to the as-built side characteristic of all other failed specimens. Specimen F-35 failed from the wire-EDM edge at  $1.408 \times 10^6$  cycles at a stress level of 250 MPa. Two additional HIP-treated specimens tested at 250 MPa, both of which failed from the as-built side, failed at approximately 461,000 and 323,000 cycles. Specimen F-49 failed from the wire-EDM edge at approximately 257,000 cycles at a stress level of 300 MPa. Two additional HIP-treated specimens, with failures from the as-built edge, failed at approximately 178,000 and 144,000 cycles. In both cases of failures from the wire-EDM side, the specimens failed at a higher number of cycles

compared to the specimens failing from the as-built side at the same stress level.

Specimen F-35 had a fatigue life 3.6 times the average life of the specimens failing from the as-built side and specimen F-49 had a fatigue life 1.6 times the average of the other two specimens tested at the same stress level. This data suggests specimens F-35 and F-49 exhibited a lower sensitivity to crack-initiation from the as-built side compared to the other specimens tested at those stress levels. At the longer fatigue lives achieved by specimens F-35 and F-49, crack-initiation shifted to the wire-EDM surface suggesting the presence of a defect or other surface anomaly on the wire-EDM surface.

A macro-level view of the crack-propagation region is shown in the SEM image in Figure 40. While not readily apparent from the lower magnification image in Figure 40, the length of the fractured edge along the wire-EDM surface contains multiple regions of subsurface voids located slightly beneath the wire-EDM surface. Detailed SEM images of the locations marked 'A' and 'B' in Figure 40 are shown in Figure 41. During SEM examination of specimen F-49, regions of subsurface voids similar in appearance to the voids noted on specimen F-35 were observed along the length of the fractured edge in F-49. The SEM examination of the fracture surfaces suggests both specimens suffered from similar subsurface defects under the wire-EDM surface.

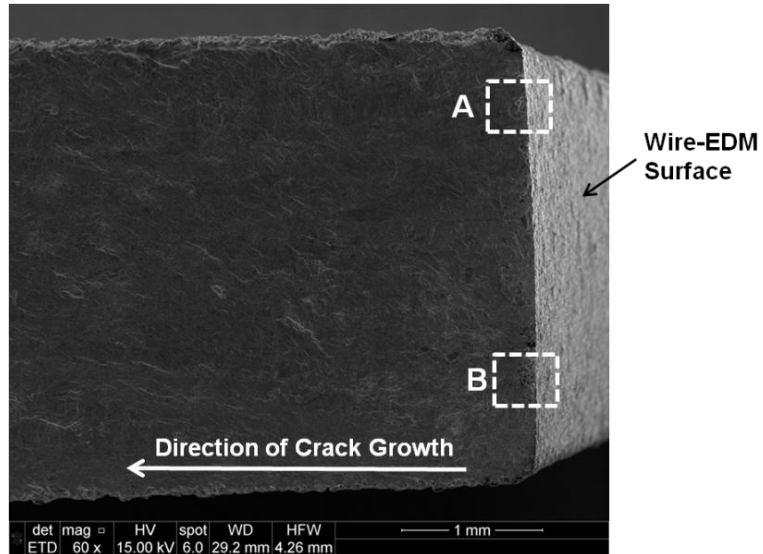
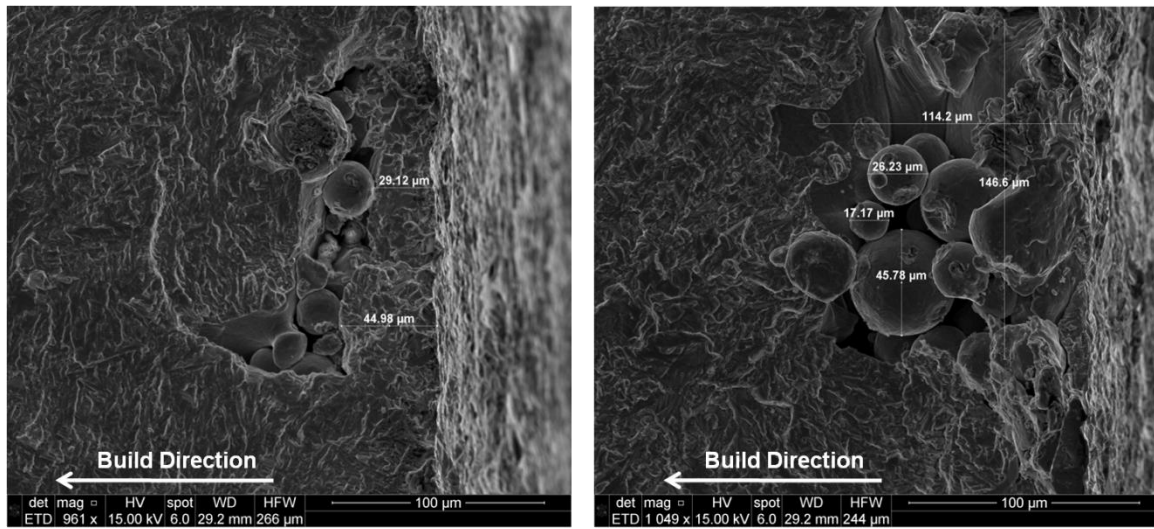


**Figure 40.** SEM image of HIP-treated specimen F-35 where crack initiation occurred at the wire-EDM surface; areas A and B denote subsurface void locations shown in greater detail in Figure 41.



**A) Location A**

**B) Location B**

**Figure 41.** SEM images of subsurface voids near the wire-EDM surface of HIP-treated specimen F-35 with un-melted Ti-64 particles trapped within the voids.

The void at location ‘A’ shown in Figure 41A is located at a depth of 29 – 45  $\mu\text{m}$  under the wire-EDM surface. This equates to the thickness of approximately a single build-layer of solid material separating the void from the wire-EDM surface. The size of the cavity at location ‘B’ measures 114.2  $\mu\text{m}$  by 146.6  $\mu\text{m}$ . The depth of the void into the plane of the fracture surface was not determined from the two-dimensional image. Within the voids, several spherical particles are seen with diameters ranging from 17.2  $\mu\text{m}$  to 45.8  $\mu\text{m}$ . A SEM/EDS scan was performed on the particles indicating that all particles had the same composition. The results of the SEM/EDS scan on the smallest particle, measuring 17.2  $\mu\text{m}$  in diameter, are shown in Figure 42. These results confirm the particles are un-melted Ti-Al particles consisting of approximately 96.7% titanium and 6.3% aluminum within a 3-5% error margin.

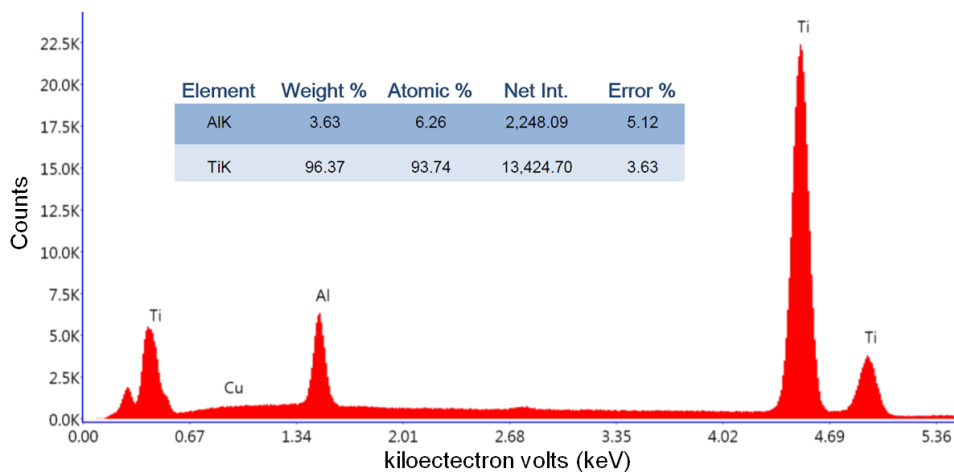


**Figure 42. Results of SEM/EDX analysis to identify the composition of trapped particles within subsurface defect in specimen F-35.**

#### 4.5. Metallographic Results

Micrographs of the as-built, stress-relieved, and HIP-treated material were obtained from polished and etched metallographic samples. The as-built and stress-relieved samples were sectioned from tensile specimens produced in Build 2/3 with a 30  $\mu\text{m}$  build layer thickness. The HIP samples were sectioned from a tensile specimen produced in Build 1 with a 60  $\mu\text{m}$  build layer thickness. Optical micrographs of the as-built, stress-relieved, and HIP-treated material are shown in Figure 43 at 50 $\times$  and 100 $\times$  magnifications. SEM micrographs are shown in Figure 44 at 154 $\times$  and 400 $\times$  magnifications. Lighter-colored areas within the image are alpha phase and darker regions correspond to the beta phase. From Figures 43-44, the microstructures of the three configurations are primarily martensitic with colonies of acicular, or thin, needle-shaped,  $\alpha'$  lathes within prior-beta grain boundaries [73]. The observed microstructure is consistent with SLM Ti-64 microstructures reported in previous studies [9, 29, 36, 42].

The overall microstructure in terms of grain size and orientation is generally similar between the as-built, stress-relieved, and HIP-treated material. This is expected since heat treatments were performed below the beta transus temperature. At temperatures below beta transus, Ti-64 remains a mixture of alpha and beta phase. A reliable quantification of the ratio of alpha to beta phase was not obtainable from the micrographs to evaluate the effect of heat treatment on the phase composition. Some of the apparent differences in appearance in the optical and SEM micrographs shown in Figures 43-44 are attributed to inconsistencies with the amount of etching. The clarity of the grain structure in the SEM images of the HIP-treated material shown in Figure 44E-F is relatively poor compared to that shown for the as-built and stress-relieved material. It is

suspected the reduction in quality of the SEM images for the HIP-treated material was due to over-etching of the polished surface.

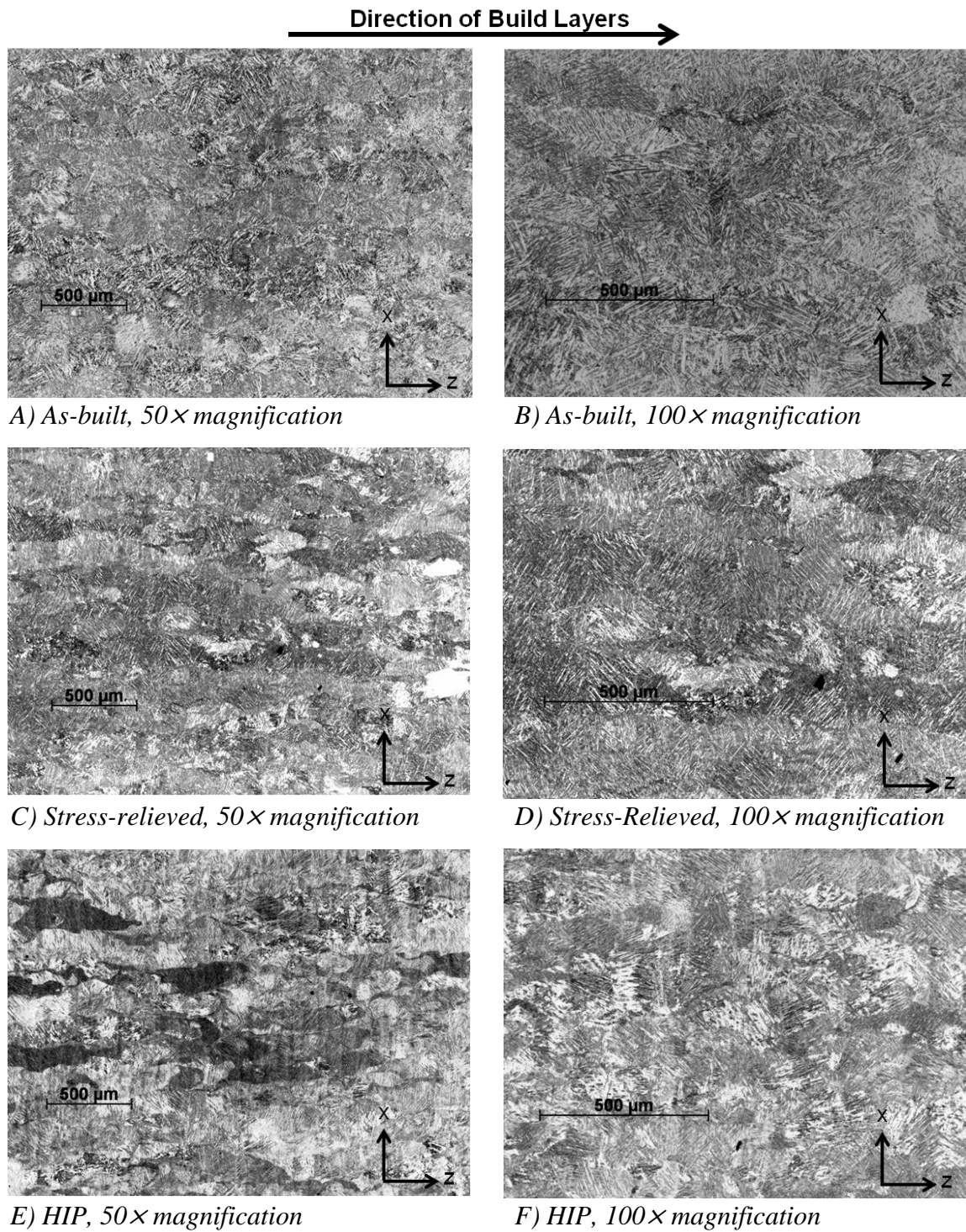
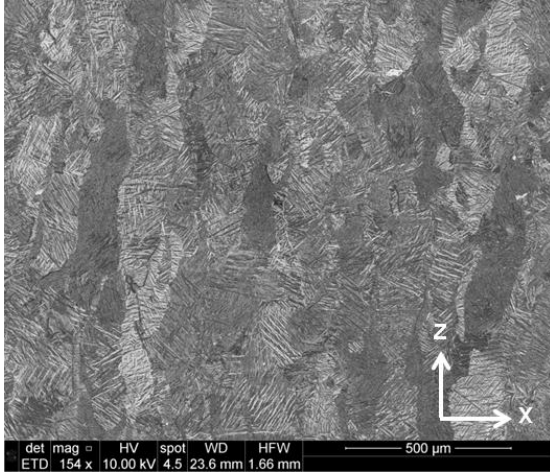
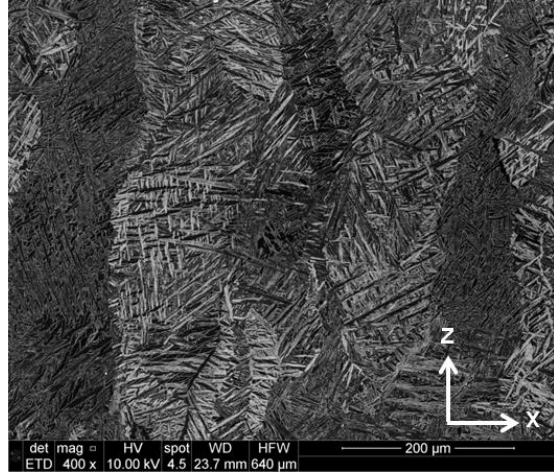


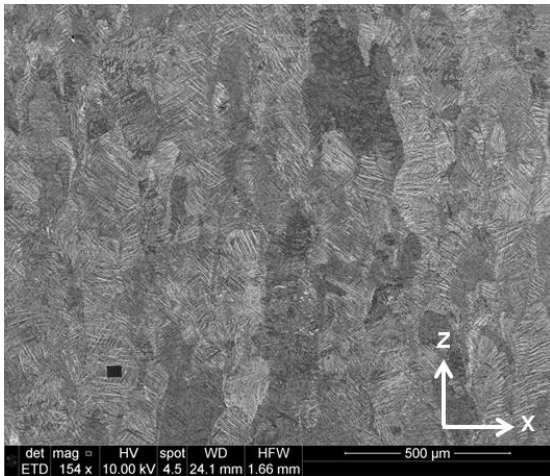
**Figure 43. Optical micrographs of as-built, stress-relieved, and HIP configurations.**



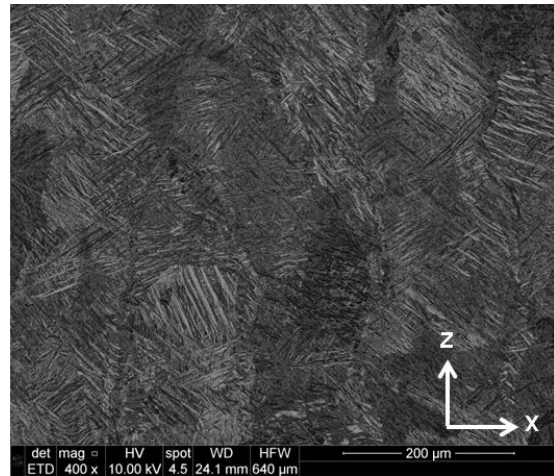
A) As-built, 1.66 mm HFW



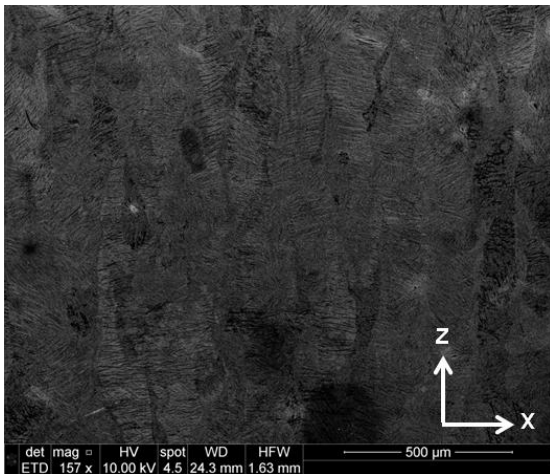
B) As-built, 640 mm HFW



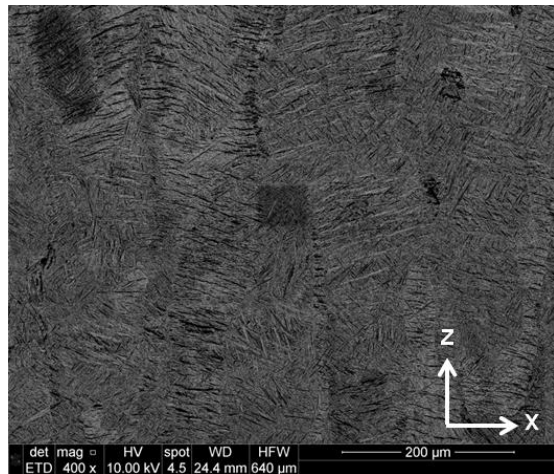
C) Stress-relieved, 1.66 mm HFW



D) Stress-relieved, 640 mm HFW



E) HIP, 1.63 mm HFW



F) HIP, 640 mm HFW

Figure 44. SEM micrographs of as-built, stress-relieved, and HIP configurations.

The primary goal of the metallographic examination was to obtain measurements of grain size and characterization of porosity. Since the prior-beta grain boundaries are not clearly distinguishable in either the optical or SEM micrographs, it is difficult to obtain precise grain-size measurements. Measurements were collected on the relatively few distinguishable grains from the SEM images of the as-built and stress-relieved materials shown in Figure 44A and Figure 44C. Grain sizes in the as-built and stress-relieved material were very similar with measurements ranging from approximately 0.57 mm to 1.0 mm in length and 0.10 to 0.13 mm in width.

Porosity was not observed in the polished and etched surfaces for any of the metallographic samples. Small, dark-colored, circular shaped features visible on some areas of the optical micrographs were initially suspected as either porosity or precipitate in the material. A region where such features were concentrated on the metallographic sample for the as-built material is shown in the optical image in Figure 45A.

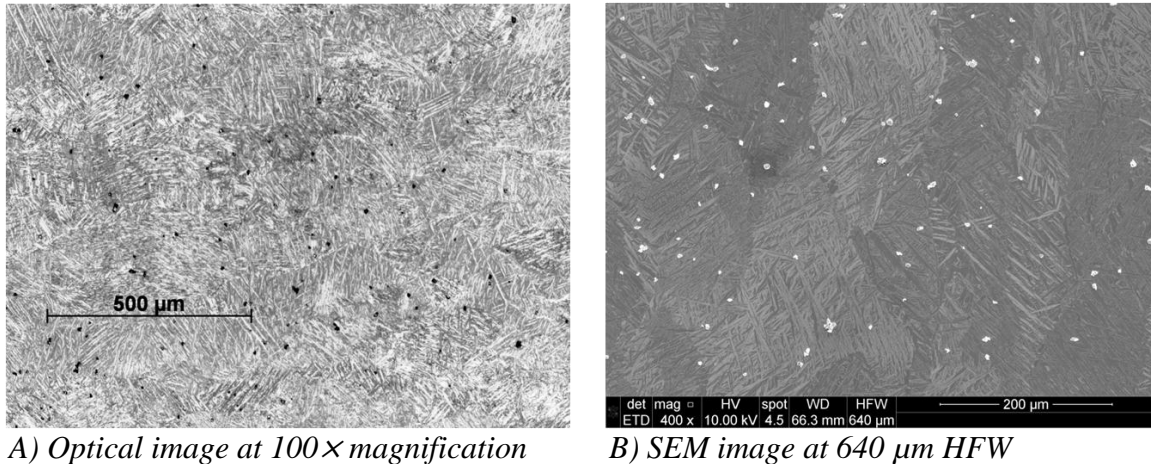


**Figure 45. Optical image (A) showing dark spots resembling porosity but identified as surface contamination as shown in the SEM image (B).**

However, when the same region is viewed with an SEM, the particles appear as flakes of a surface contaminate. EDS spectrums identified these particles as silver. It is suspected several of the metallographic samples were contaminated by silver paint during the final polishing step in the Vibromet polisher. The Vibromet polisher utilizes a fluid reservoir and was likely contaminated by silver paint commonly used in the laboratory as a surface coating. Therefore, no evidence of actual porosity was observed by the optical and SEM examinations of the polished and etched metallographic samples. Based on these results, either the as-built material has little to no porosity after SLM manufacturing by the EOSINT M 280 machine or the metallographic preparation and/or examination techniques were insufficient to identify any porosity potentially present in the material.

#### **4.6. Fatigue Life Results of HIP Specimens with Machined Edges**

To provide additional insight into the effects of stair-stepping on fatigue life, 10 HCF tests were performed on HIP-treated specimens with the edges machined to a smooth finish. The fatigue testing data for the HIP-treated specimens with machined edges are shown in the stress-life curve in Figure 46. Groups of two specimens each were tested at 300 MPa, 400 MPa, and 500 MPa to determine the slope of the finite-life region using linear regression. During testing at a maximum stress level of 300 MPa, specimen F-59 experienced a fracture within the gripped area of the specimen. Due to the test failure, the data point for specimen F-59 is not included in the stress-life data. Three staircase data points were accomplished at 260 MPa, 280 MPa, and 290 MPa to estimate the mean fatigue life. However, all three staircase data points survived until test run-out at  $10^7$  cycles providing insufficient data for analysis by the Dixon-Mood

equations. In absence of sufficient staircase data, the mean fatigue life was estimated from the available data at 295 MPa. This value was determined by the average of the lowest stress level at which a failure occurred, 300 MPa, and the highest stress level at which a test survival was observed, 290 MPa. Although the experimental data indicates a 60 MPa, or 25%, increase to the mean fatigue life as the result of machining the edges of the specimens, additional staircase data points are needed to generate a more accurate estimate of the mean fatigue life. As shown in Figure 46, machining the edges of the specimen increased both the fatigue life and the endurance limit of the HIP-treated configuration.

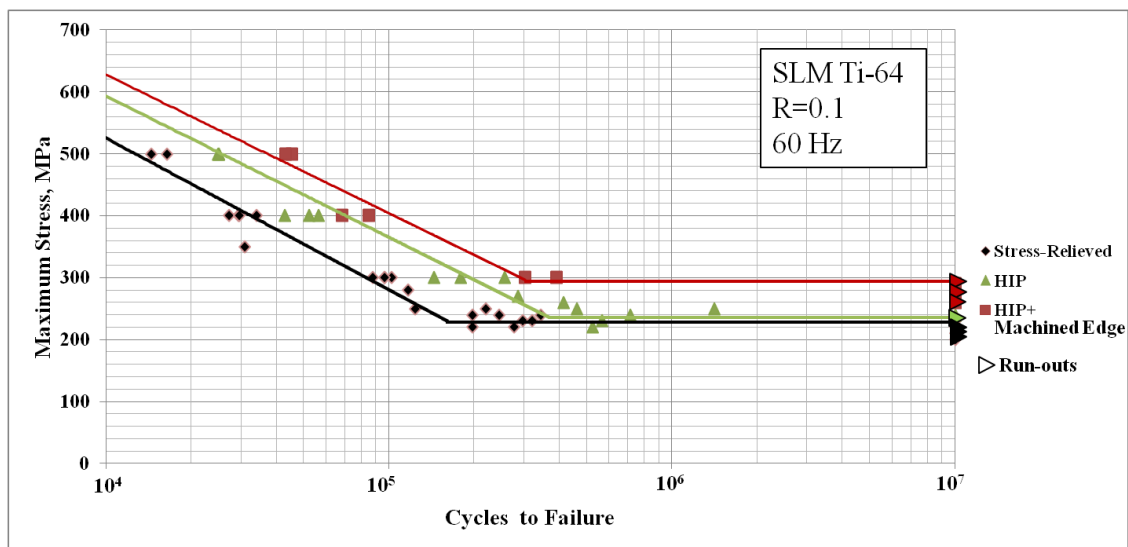


**Figure 46. S-N plot for stress-relieved, HIP-treated, and an additional HIP-treated configuration with machined edges to eliminate the effects of stair-stepping.**

A comparison of fatigue life based on the average number of cycles until failure at 300 MPa, 400 MPa, and 500 MPa is shown in Table 11. From Table 11, the HIP-treated specimens demonstrated an increase in fatigue life ranging from 52.1% to 79.0% by machining the narrow edges. Of note, the specimen alignment in the testing machine was

rechecked after testing the first two specimens, F-56 and F-57, at 400 MPa. The alignment check utilized an untested specimen with a reference line marked on the specimen's surface denoting the line of symmetry through the center of the test section. This alignment check indicated the centerline of the reference specimen was approximately 0.5 mm off-center from the centerline reference marking engraved on the surface of the lower set of wedge grips. To correct the specimen alignment prior to testing of the remaining specimens, the specimen alignment guide on the lower wedge grips was adjusted. Adjustment of the specimen alignment guide on the upper wedge grips was not required. It is suspected a small degree of bending loads from the 0.5 mm misalignment during testing of specimens F-56 and F-57 resulted in reduced fatigue life for the two data points at the 400 MPa maximum stress level.

***Table 11. Comparison of the average number of cycles to failure for the HIP-treated configuration with machined edges.***

Max Stress (MPa)	Average #Cycles to Failure		
	HIP	HIP + Machined Edges	% Increase
300	193,143	345,762	79.0 %
400	50,326	76,543	52.1 %
500	24,929	44,101	76.9 %

Due to schedule constraints and equipment availability, examination of the fracture surfaces for the HIP-treated specimens with machined edges was conducted by optical methods only. Based on the macroscopic appearance of the crack propagation region and fast-fracture areas, crack initiation occurred at one of the corners of the fracture surface in

5 of the 6 failed specimens. This behavior is similar to the crack propagation behavior observed in the specimens with un-machined edges. After failure of at a maximum stress-level of 500 MPa, the fracture surface of specimen F-65 exhibited a crack initiation near the mid-point of the specimen's width. A macroscopic-level view of the fracture surface from specimen F-65 is shown in Figure 47. The black, dashed-line in Figure 47 represents the approximate boundary between the crack propagation region and fast-fracture or overload region. It is seen the crack propagation region is located in the center region of the specimen and overload occurred along both of the narrow edges. Although the precise location of crack-initiation was not determined from the optical image, the absence of visible defects or pores within the internal areas of the crack-propagation region suggests the crack initiation most likely occurred from the rough outer-surface of the specimen.

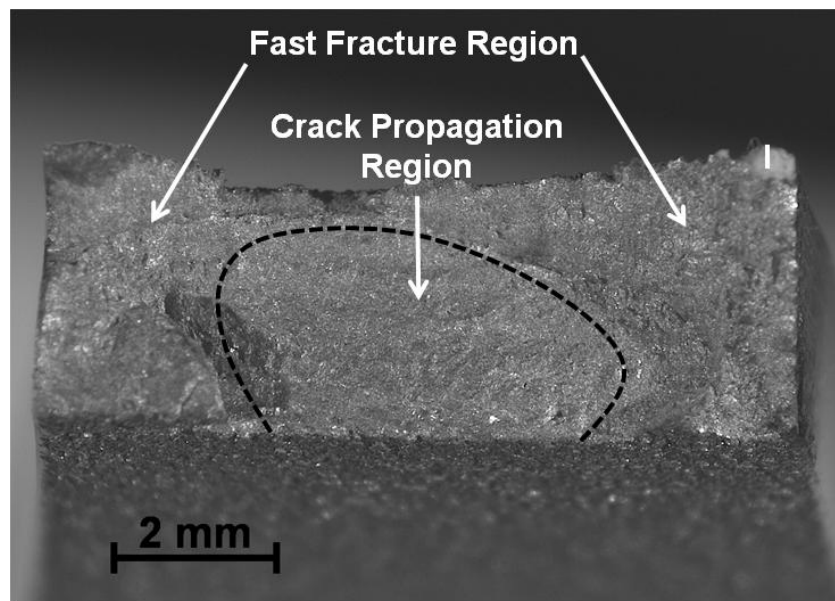


**Figure 47. Optical microscope image at 12 $\times$  magnification with a 0.63 $\times$  objective lens of the fatigue fracture surface for specimen F-65 showing crack initiation from the mid-point of the specimen's width.**

## V. Conclusions and Recommendations

### 5.1. Review of Research Objectives

The overarching goal of this research was to investigate the high-cycle fatigue life properties of SLM Ti-64, and specifically, determine whether HIP improves the fatigue life of specimens built directly to net-shape when the surface is not machined. To fulfill this goal, research was conducted in support of the following five research objectives:

1. Verify the quality of SLM Ti-64 test specimens fabricated with a commercially available machine by verifying the static tensile properties are consistent with data published by the manufacturer.
2. Collect experimental data to generate a stress-life curve for a baseline, stress-relieved SLM Ti-64 fatigue specimen fabricated directly to net dimensions.
3. Collect experimental data to generate a stress-life curve for SLM Ti-64 fatigue specimens fabricated directly to net dimensions and then processed by HIP.
4. Conduct examination of fracture surfaces to determine whether HIP influences the location of the fatigue crack initiation sites.
5. Collect experimental data to generate a stress-life curve for a second HIP-treated configuration with machined edges to assess the impact to fatigue life after removal of stair-step ridges.

A total of 20 tensile specimens and 65 fatigue specimens were successfully manufactured in three production runs with an EOSINT M 280 DMLS machine operated by a commercial vendor. Furnace heat-treatment and HIP were successfully performed in accordance with ASTM F2924-14 and guidelines from the manufacturer.

Objective 1 was satisfied through tensile testing of as-built, heat-treated, and HIP-treated test specimens following the procedures of ASTM E8/E8M. As shown in Table 12, test results from the as-built and stress-relieved specimens demonstrated the experimental UTS and yield strength for the as-built and stress-relieved material are slightly below the typical values reported by EOS. However, the experimental values exceed minimum strength requirements specified by the manufacture and ASTM F2924. Experimental data indicates heat-treatment is required to meet minimum elongation at break requirements by improving ductility. Although the stress relief process was demonstrated sufficient, the experimental data indicates the HIP parameters used in this study increased  $\epsilon_f$  above the minimum threshold of 10%.

**Table 12. Comparison of experimental tensile results to manufacture's data.**

	<b>ASTM F2924 Powder Bed Fusion</b>	<b>EOS As-built</b>	<b>Present Study As-Built</b>	<b>EOS Stress-Relieved*</b>	<b>Present Study Stress-Relieved*</b>	<b>Present Study HIP**</b>
<b>UTS ± STD (MPa)</b>	895 (min)	1230 ± 50 (typ)	1140.7±5.0	1050 ± 20 (typ) 930 (min)	936.9±3.6	910.1±2.9
<b>YS ± STD (MPa)</b>	825 (min)	1060 ± 50 (typ)	938.2±7.7	1000 ± 20 (typ) 860 (min)	862.4±3.1	835.4±3.8
<b><math>\epsilon_f</math> (%)</b>	10 (min)	10 ± 2 (typ)	6.7±1.0	10 (min)	11.4±0.8	7.2±1.0
<b>E ± STD (GPa)</b>	NA	110 ± 10 (typ)	91.8±0.5	116 ± 10 (typ)	98.0±1.2	106.8±1.3

\* Experimental data shown for as-built and stress-relieved is based on 30  $\mu\text{m}$  build layers

\*\* Experimental data shown for HIP is based on 60  $\mu\text{m}$  build layers

Objectives 2 and 3 were satisfied through successful HCF testing of 65 fatigue specimens in accordance with the procedures of ASTM E466-07. Testing was conducted with a stress ratio of  $R = 0.1$  at a frequency of 60 Hz. Test results were sufficient to generate stress-life curves for both the stress-relieved and HIP-treated material configurations using the log-linear fatigue model presented in equation (8). An unintended and unanticipated difference in the processing parameters between Build 1 and builds 2/3 resulted in 19 stress-relieved fatigue specimens produced with 60  $\mu\text{m}$  build layers and 11 stress-relieved fatigue specimens produced with 30  $\mu\text{m}$  build layers. However, experimental data demonstrated the differences in HCF stress-life behavior between the 30  $\mu\text{m}$  and 60  $\mu\text{m}$  layer thicknesses are relatively minor. Accordingly, the stress-relieved data points were analyzed as a single population for comparison to the HIP-treated results.

Fracture surfaces were examined under an optical microscope and SEM in support of Objective 4. Based on the macroscopic features of the fracture surface, the appearance of the crack propagation and fast-fracture regions indicates all HCF failures in the stress-relieved specimens had crack initiations originating from the as-built edge of the specimen. The same pattern was observed in 22 of the 24 successful tests on the HIP-treated configuration. SEM examination of the two HIP-treated specimens with failures originating from the wire-EDM edge suggests these failures were caused by the presence of subsurface voids containing particles of un-melted Ti-64 powder. Due to the limited presence of fatigue striations or other distinguishing features, the precise location(s) of crack-initiation was not determined. However, examination by the SEM did not indicate the presence of internal porosity in non-HIP-treated specimens from which fatigue cracks

may have initiated. Since HCF failures in all of the specimens appear to initiate from the surface, experimental data suggests HIP did not have a quantifiable impact on the location of HCF crack-initiation compared to the stress-relieved specimens.

Finally, Objective 5 was satisfied through HCF testing of specimens with machined edges. The purpose of the machining was to remove stair step ridges and match the surfaces finishes of the narrow edges. A total of 10 specimens were available for this configuration. Using the limited number of available specimens, six specimens were tested among three maximum stress levels to determine the slope of the finite-life portion of the stress-life curve. During testing at the 300 MPa stress level, a specimen fractured within the grip area resulting in a failed test. Staircase testing was attempted with the remaining three specimens to estimate the mean fatigue life. However, all three specimens survived until test run-out. Since the attempted staircase data points were insufficient for analysis using the Dixon-Mood methodology, the mean fatigue life was estimated as the average of the lowest stress level at which a failure occurred and the highest stress level at which a survival was observed.

## **5.2. Discussion of Results**

Experimental data from this study indicates HIP improved the fatigue life of specimens built directly to net tolerances by 61.4% when subjected to a maximum stress level of 500 MPa compared to the baseline stress-relieved configuration. At a lower stress level of 300 MPa, HIP improved fatigue life by 102% compared to the baseline stress-relieved configuration. Staircase testing revealed HIP had a negligible impact on the observed HCF endurance limit for life spans up to  $10^7$  cycles. The experimental

mean fatigue life was determined by the Dixon-Mood method as  $\bar{\mu} = 226$  MPa for the stress-relieved specimens and  $\bar{\mu} = 235$  MPa for the HIP-treated configuration. Tensile testing results confirm the static material properties for the specimens produced in this study are representative of the typical performance of SLM Ti-64 manufactured with an EOSINT M 280 machine based on data published by the manufacturer. Therefore, from a standpoint of material quality, the experimental HCF results are considered representative of typical commercially produced SLM Ti-64 material built directly to net tolerances.

A comparison of the experimental fatigue results with the results of past SLM Ti-64 HCF studies conducted by Van Hooreweder *et al.* and Gong *et al.* is shown in Figure 48 [31, 47]. Figure 48 also includes the range of expected stress-life for wrought Ti-64 with machined and polished surfaces based on data published in Donachie [73]. In the study by Van Hooreweder *et al.*, HCF testing with  $R = 0$  at 75 Hz was conducted on flat, dog-bone shaped specimens with machined surfaces. Specimens were manufactured in the horizontal XY-direction with a non-commercial, in-house SLM machine with a 250 watt laser using a build layer thickness of 30  $\mu\text{m}$ . Specimens were stress-relieved at 650  $^{\circ}\text{C}$  for 4 hours in an argon atmosphere [47]. In the study by Gong *et al.*, HCF testing with  $R = 0.1$  at 50 Hz was conducted on cylindrical shaped specimens built directly to net-dimensions without surface machining. Specimens in Gong *et al.* were manufactured in the vertical Z-direction with an EOSINT M 270 employing the same DMLS process as the EOSINT M 280 used for the present study. Specimens were built with a 30  $\mu\text{m}$  build layer thickness and stress-relieved at 650  $^{\circ}\text{C}$  for 4 hours in an argon atmosphere [31].

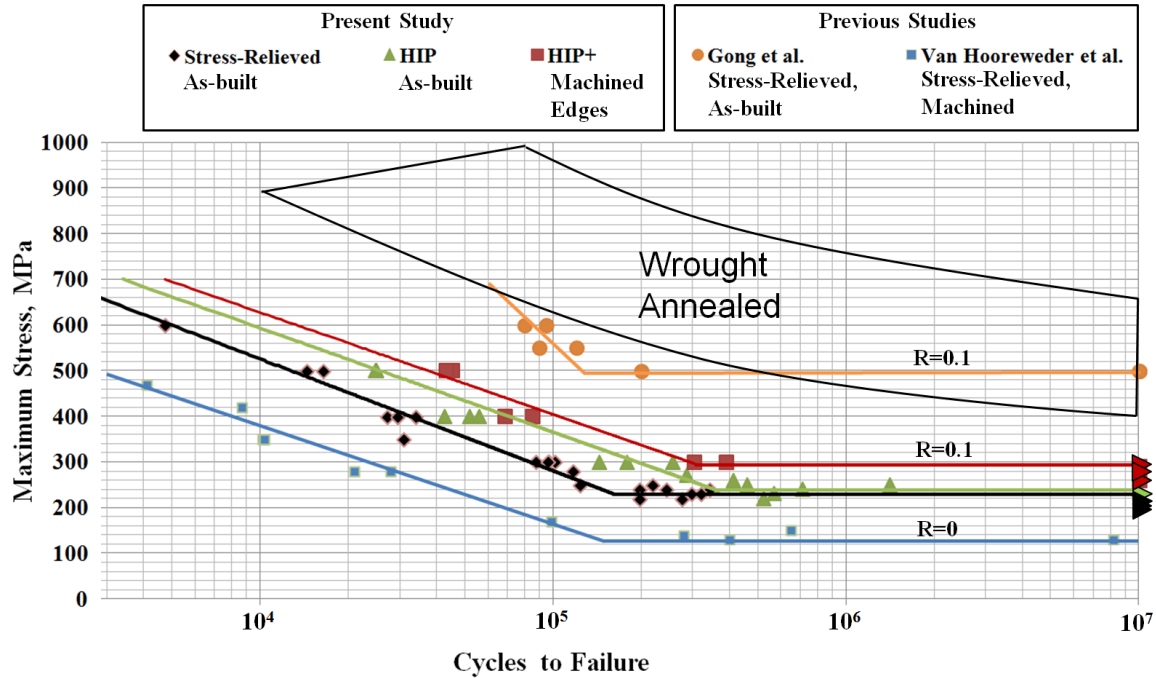


**Figure 48. Stress-life comparison of the experimental HCF data with previous research on stress-relieved Ti-64 specimens and the typical expected range of wrought material [31,47,73].**

From Figure 48, experimental stress-life data obtained in this study falls within the range of expected results based on data from previous studies published in literature. The fatigue specimens in this study share similar size and geometry to those tested in Van Hooreweder *et al.* Despite having machined surfaces, the mean fatigue life reported in Van Hooreweder *et al.* of  $\bar{\mu} = 126.2$  MPa is 44% lower than the mean fatigue life observed for the stress-relieved specimens with as-built surfaces in the present study [47]. Likely contributors for the difference in HCF-life are the differences in machines and processing parameters used to manufacture the specimens. Such differences highlight the benefits of using optimized parameter sets offered in currently available commercial SLM machines such as the EOSINT M 280. However, the data in Figure 48 from Gong *et al.* presents an additional challenge: specimens produced using the same process by

similar machines from the same manufacture produced different experimental results in HCF stress-life behavior. The specimens in Gong *et al.* were produced using an EOSINT M 270 which uses the same patented DMLS process as the EOSINT M 280. Per the manufacture, the M 280 is an updated and improved version of the M 270 with a slightly larger build volume and a higher power laser energy source [60]. Furthermore, EOS does not indicate a difference in typical material properties for SLM Ti-64 based on production with an M 280 versus M 270. As shown in Figure 48, the experimental data published in Gong *et al.* demonstrates a stress-life nearly equivalent to the typical stress-life of wrought and annealed Ti-64 specimens. Of note, the specimens in Gong *et al.* were built directly to net tolerances without surface machining or polishing. The primary difference between the experimental set-up in Gong *et al.* and the present study is the specimen geometry. The specimens in the study by Gong *et al.* utilized cylindrical shaped-specimens which have a lower theoretical stress concentration factor than the rectangular cross section specimens used in the present study [31]. Additionally, it is possible variations in the powder feedstock, processing conditions, and the experimental methods may have also influenced the differences in the experimental HCF performance.

Although the experimental results indicate HIP had a measurable improvement on fatigue life ranging from 61.4% to 102% compared to the stress-relieved baseline, the data collected in this study is inconclusive on the role played by internal porosity and defects. Several previous studies in literature have pointed to porosity in SLM Ti-64 as a driver of reduced fatigue life [9, 15-17]. However, porosity was not observed in microscopic examination of the fracture surfaces or polished samples of either the as-built or stress-relieved specimens. Therefore, it is difficult to conclude the observed

increase in fatigue life exhibited by the HIP-treated specimens was influenced by densification of the material achieved by the HIP process. The lack of evidence of crack-initiation from internal pores or defects in the fracture surfaces of the stress-relieved fatigue specimens suggests surface roughness and defects near the surface are of greater significance to fatigue crack initiation than any micro-porosity potentially present in non-HIP-treated specimens. The results of this study support alternative explanations for HCF susceptibility rather attributing the reduced fatigue-life to porosity. Experimental results are in agreement with the same conclusion reached in the study in Van Hooreweder *et al.* which concluded reduced fatigue life in SLM Ti-64 is likely caused by anisotropy and other microstructure characteristics as opposed to internal porosity or material imperfections [47].

### **5.3. Recommendations for Future Work**

Experimental data from this study provides an initial assessment on the impact of HIP to the HCF-life of Ti-64 specimens built directly to net-tolerances without subsequent machining of the surfaces to reduce surface roughness. Such insight is beneficial to the USAF and other DoD organizations to assess whether HIP is a necessary processing step to ensure adequate performance and reliability of SLM parts used in aerospace components susceptible to HCF failure. However, a considerable amount of future research is necessary to further investigate the fatigue characteristics of SLM Ti-64 and the effects of HIP before SLM parts built directly to net tolerances are qualified for operational use. A possible next step is to further investigate the microstructural changes occurring as the result of the HIP process. In the present study, the temperature of 798 °C used for the stress relief process was lower than the temperature of 899 °C used during

HIP. There is uncertainty as to whether the difference in observed fatigue life between the stress-relieved and HIP-treated specimens is the result of densification achieved by HIP or from preferential microstructure evolution resulting from the higher temperatures used during the HIP process. Once these microstructural changes are better understood, it is possible to conduct research on optimizing HIP temperature, pressure, and soak-time parameters to tailor the material properties for improved HCF performance.

Additionally, if porosity is determined an insignificant factor, it is possible to conduct research on achieving equivalent results by standard heat-treatment methods not requiring pressurized furnaces.

The surface pitting observed on many of the wire-EDM surfaces on specimens utilizing reduced density support material in builds 2/3 warrants an investigation of the effects of support material on bordering solid surfaces. For the two HIP-treated specimens with HCF failures originating from the wire-EDM edge, surface pitting was present in the vicinity of the fracture. Examination of the fracture surfaces revealed subsurface voids near the wire-EDM surface. Further investigation is needed to determine if these defects were the direct result of building the solid layers forming the test specimen on top of layers of porous support material during SLM fabrication. Research in this area is important to understanding the design constraints and implications of utilizing porous support material during SLM fabrication.

Finally, it is recommended future research is directed towards compiling available fatigue data in both the high-cycle and low-cycle regimes to develop analytical models to predict fatigue life for SLM parts built directly to net shape. Such models must account for factors unique to the SLM process such as surface roughness, stair-stepping, build

layer thickness, and anisotropy. Incorporating these factors into existing finite element analysis design tools will allow designers to evaluate the performance of proposed SLM-fabricated parts based on the specific part geometry and loading conditions. Improved analysis tools will facilitate optimization of part geometry to balance mechanical performance with SLM-fabrication constraints.

## Bibliography

- [1] NASA, "3D Printing In Zero-G Technology Demonstration (3D Printing In Zero-G)," 25 November 2014. [Online]. [http://www.nasa.gov/mission\\_pages/station/research/experiments/1115.html](http://www.nasa.gov/mission_pages/station/research/experiments/1115.html). Accessed on: 22 December 2014.
- [2] I. Gibson, D. W. Rosen and B. Stucker, *Additive Manufacturing Technologies*, New York: Springer, 2010.
- [3] J. Ruan, T. E. Sparks, Z. Fan, J. K. Stroble, A. Panackal and F. Liou, "A review of layer based manufacturing processes for metals," presented at *Solid Freeform Fabrication Symposium*, 2006. Available: <http://hdl.handle.net/10355/31485>.
- [4] K. D. Rekedal and D. Liu, "Fatigue life of selective laser melted and hot isostatically pressed ti-6Al-4v absent of surface machining," presented at *2015 AIAA Scitech Conference*, Kissimmee, FL, 2015.
- [5] H. Richards and D. Liu, "Topology optimization of additively-manufactured, lattice-reinforced penetrative warheads," presented at *2015 AIAA Scitech Conference*, Kissimmee, FL, 2015.
- [6] D. Walker and D. Liu, "Topology optimization of an aircraft wing," presented at *2015 AIAA Scitech Conference*, Kissimmee, FL, 2015.
- [7] R. D. Pollak, "Analysis of Methods for Determining High Cycle Fatigue Strength of a Material With Investigation of Ti-6Al-4V Gigacycle Fatigue Behavior," Ph.D. dissertation, Air Force Institute of Technology (AU), Wright-Patterson AFB, OH, October 2005 (ADA441887).
- [8] S. S. Shipp, *et al.*, "Emerging global trends in advanced manufacturing," Institute for Defense Analyses, Alexandria, VA, March 2012 (ADA558616).
- [9] P. Edwards and M. Ramulu, "Fatigue Performance Evaluation of Selective Laser Melted Ti-6Al-4V," *Materials Science and Engineering*, vol. 598, pp. 327-337, 26 March 2014. DOI: 10.1016/j.msea.2014.01.041.
- [10] M. Koike, *et al.*, "Evaluation of Titanium Alloys Fabricated Using Rapid Prototyping Technologies-Electron Beam Melting and Laser Beam Melting," *Materials*, vol. 4, issue 10, pp. 1776-1792, 2011. DOI: 10.3390/ma4101776.
- [11] J. Yu, M. Rombouts, G. Maes and F. Motmans, "Material Properties of Ti6Al4V Parts Produced by Laser Metal Deposition," *Physics Procedia*, vol. 39, pp. 416-424, 2012. DOI: 10.1016/j.phpro.2012.10.056.

- [12] B. A. Cowles, "High cycle fatigue in aircraft gas turbines-an industry perspective," *International Journal of Fracture*, vol. 80, issue 2-3, pp. 147-163, April 1989. DOI: 10.1007/bf00012667.
- [13] T. Nicholas, *High Cycle Fatigue: A Mechanics of Materials Perspective*, San Diego, CA: Elsevier, 2006.
- [14] K. S. Chan, M. Koike, R. L. Mason and T. Okabe, "Fatigue Life of Titanium Alloys Fabricated by Additive Layer Manufacturing Techniques for Dental Implants," *Metallurgical and Materials Transactions*, vol. 44, issue 2, pp. 1010-1022, 2013. DOI: 10.1007/s11661-012-1470-4.
- [15] S. Leuders, *et al.*, "On the Mechanical Behaviour of Titanium Alloy TiAl6V4 Manufactured by Selective Laser Melting: Fatigue Resistance and Crack Growth Performance," *International Journal of Fatigue*, vol. 48, pp. 300-307, 2013. DOI: 10.1016/j.ijfatigue.2012.11.011.
- [16] M. Simonelli, "Microstructure evolution and mechanical properties of selective laser melted Ti-6Al-4V," Ph.D. dissertation, Loughborough University, Leicestershire, U.K., 2014. Available: <https://dspace.lboro.ac.uk/2134/15070>.
- [17] M. Thöne, S. Leuders, A. Riemer, T. Tröster and H. Richard, "Influence of heat-treatment on selective laser melting products—eg Ti6Al4V," presented at *Twenty-Third Annual International Solid Freeform Fabrication (SFF) Symposium*, 2012. Available: <http://utwired.engr.utexas.edu/lff/symposium/proceedingsarchive/pubs/manuscripts/2012/2012-38-thoene.pdf>.
- [18] K. Hartke, Air Force Research Laboratory Materials and Manufacturing Directorate, Wright-Patterson AFB, OH, Tech. Rep. AFRL-RX-WP-TR-2011-4322, August 2011 (ADA551779).
- [19] C. Fink, "An overview of additive manufacturing, part I," *AMMTIAC Quarterly*, vol. 4, issue 2, pp. 9-12, August 2009. Available: [https://www.dsiac.org/files/legacy\\_journal/TechSolutions12.pdf](https://www.dsiac.org/files/legacy_journal/TechSolutions12.pdf).
- [20] C. M. McNulty, N. Arnas and T. A. Campbell, "Toward the printed world: Additive manufacturing and implications for national security," *Defense Horizons*, issue 73, pp. 1-16, September 2012.
- [21] ASTM International, "Committee F42 on Additive Manufacturing Technologies," 2014. [Online]. <http://www.astm.org/COMMITTEE/F42.htm>. Accessed on: 16 October 2014.

- [22] General Electric Company, "World's First Plant to Print Jet Engine Nozzles in Mass Production - GE Reports," 2014. [Online].  
<http://www.gereports.com/post/91763815095/worlds-first-plant-to-print-jet-engine-nozzles-in-mass>. Accessed on: 16 October 2014.
- [23] R. R. Dehoff, et al., "Case study: Additive manufacturing of aerospace brackets," *Advanced Materials and Processes*, vol. 171, issue 3, pp. 19, 2013. Available:  
<http://www.asminternational.org/documents/10192/6012351/amp17103p19.pdf/9587521c-e59b-423b-9b99-422d6584b2c6>.
- [24] D. Brackett, I. Ashcroft and R. Hague, "Topology optimization for additive manufacturing," presented at *Proceedings of the 24th Solid Freeform Fabrication Symposium (SFF' 11)*, 2011. Available: <http://utwired.engr.utexas.edu/lff/symposium/proceedingsarchive/pubs/Manuscripts/2011/2011-27-Brackett.pdf>.
- [25] M. Tomlin and J. Meyer, "Topology optimization of an additive layer manufactured (ALM) aerospace part," presented at *The 7th Altair CAE Technology Conference*, Gaydon, UK, 2011. Available: <http://www.altairuniversity.com/wp-content/uploads/2013/10/Altair-Paper-Topology-Optimisation-of-Nacelle-Hinge-Matt-Tomlin.pdf>.
- [26] P. Heintl, L. Müller, C. Körner, R. F. Singer and F. A. Müller, "Cellular Ti-6Al-4V structures with interconnected macro porosity for bone implants fabricated by selective electron beam melting," *Acta Biomaterialia*, vol. 4, issue 5, pp. 1536-1544, September 2008. DOI: 10.1016/j.actbio.2008.03.013.
- [27] E. Bennett and E. Pettus, "Building a Competitive Edge with Additive Manufacturing," Air War College, Air University, Maxwell AFB, AL, 2013. Available: [http://www.au.af.mil/au/awc/awcgate/cst/bh\\_2013\\_bennett.pdf](http://www.au.af.mil/au/awc/awcgate/cst/bh_2013_bennett.pdf).
- [28] C. J. R. Drushal, "Additive Manufacturing: Implications to the Army Organic Industrial Base in 2030," United States Army War College, Carlisle, PA, 2013 (ADA593246).
- [29] M. Simonelli, Y. Tse and C. Tuck, "Effect of the build orientation on the mechanical properties and fracture modes of SLM ti-6Al-4V," *Materials Science and Engineering*, vol. 616, pp. 1-11, 2014. Available: <http://www.sciencedirect.com/science/article/pii/S0921509314009538>.
- [30] C. B. Williams, F. Mistree and D. W. Rosen, "Towards the design of a layer-based additive manufacturing process for the realization of metal parts of designed mesostructure," presented at *16th Solid Freeform Fabrication Symposium*, Austin, TX, 2005. Available: <http://edge.rit.edu/content/P10551/public/SFF/SFF%202005%20Proceedings/Manuscripts%202005/20-Williams.pdf>.

- [31] H. Gong, K. Rafi, H. Gu, T. Starr and B. Stucker, "Analysis of Defect Generation in Ti-6Al-4V Parts Made Using Powder Bed Fusion Additive Manufacturing Processes," *Additive Manufacturing*, pp. 499-506, 2014. DOI: 10.1016/j.addma.2014.08.002.
- [32] J. Coykendall, M. Cotteleer, J. Holdowsky and M. Mahto, "3D opportunity in aerospace and defense: Additive manufacturing takes flight," Deloitte University Press, Westlake, TX, 02 June 2014. Available: <http://dupress.com/articles/additive-manufacturing-3d-opportunity-in-aerospace>.
- [33] J. Scott, N. Gupta, C. Weber, S. Newsome, T. Wohlers and T. Caffrey, "Additive manufacturing: Status and opportunities," Institute for Defense Analysis, Alexandria, VA, March 2012. Available: [https://cgsr.llnl.gov/content/assets/docs/IDA\\_AdditiveM3D\\_33012\\_Final.pdf](https://cgsr.llnl.gov/content/assets/docs/IDA_AdditiveM3D_33012_Final.pdf).
- [34] Advanced Manufacturing National Program Office, "America Makes (NAMII)," 2014. [Online]. [http://manufacturing.gov/nnmi\\_pilot\\_institute.html](http://manufacturing.gov/nnmi_pilot_institute.html). Accessed on: 23 October 2014.
- [35] America Makes, "Mission Statement," 2014. [Online]. <https://americamakes.us/about/mission>. Accessed on: 23 October 2014.
- [36] H. Rafi, N. Karthik, H. Gong, T. L. Starr and B. E. Stucker, "Microstructures and Mechanical Properties of Ti6Al4V Parts Fabricated by Selective Laser Melting and Electron Beam Melting," *Journal of Materials Engineering and Performance*, vol. 22, issue 12, pp. 3872-3883, 2013. DOI: 10.1007/s11665-013-0658-0.
- [37] C. Fink, "An overview of additive manufacturing, part II," *AMMTIAC Quarterly*, vol. 4, issue 3, pp. 7-10, August 2009. Available: [http://www.dsiac.org/files/legacy\\_journal/TechSolutions13.pdf](http://www.dsiac.org/files/legacy_journal/TechSolutions13.pdf).
- [38] ASTM Standard F2792-12a, "Standard Terminology for Additive Manufacturing Technologies," 2012. DOI: 10.1520/F2792-12A.
- [39] W. E. Frazier, "Metal additive manufacturing: A review," *Journal of Materials Engineering and Performance*, vol. 23, issue 6, pp. 1917-1928, 2014. Available: <http://dx.doi.org/10.1007/s11665-014-0958-z>.
- [40] B. Dutta and F. Froes, "Additive manufacturing of titanium alloys," *Advanced Materials & Processes*, vol. 172, issue 2, pp. 18-23, 2014. Available: <http://www.asminternational.org/c/portal/pdf/download?articleId=17001408&groupId=10192>.

- [41] B. Song, S. Dong, B. Zhang, H. Liao and C. Coddet, "Effects of processing parameters on microstructure and mechanical property of selective laser melted Ti6Al4V," *Materials & Design*, vol. 35, pp. 120-125, March 2012. DOI: 10.1016/j.matdes.2011.09.051.
- [42] L. Chauke, K. Mutombo and C. Kgomo, "Characterization of the direct metal laser sintered Ti6Al4V components," presented at *14th Annual International RAPDASA 2013 Conference*, Bloemfontein, Pretoria, 2013. Available: <http://hdl.handle.net/10204/7244>.
- [43] J. Kruth, M. Badrossamay, E. Yasa, J. Deckers, L. Thijs and J. Van Humbeeck, "Part and material properties in selective laser melting of metals," presented at *Proceedings of the 16th International Symposium on Electromachining*, Shanghai, China, 2010. Available: [https://lirias.kuleuven.be/bitstream/123456789/265815/1/kruth\\_isem-xvi\\_keynote\\_paper.pdf](https://lirias.kuleuven.be/bitstream/123456789/265815/1/kruth_isem-xvi_keynote_paper.pdf).
- [44] B. Vrancken, L. Thijs, J. Kruth and J. V. Humbeeck, "Heat treatment of Ti6Al4V produced by selective laser melting: Microstructure and mechanical properties," *Journal of Alloys and Compounds*, vol. 541, pp. 177-185, November 2012. Available: <http://dx.doi.org/10.1016/j.jallcom.2012.07.022>.
- [45] L. Thijs, F. Verhaeghe, T. Craeghs, J. V. Humbeeck and J. Kruth, "A study of the microstructural evolution during selective laser melting of Ti-6Al-4V," *Acta Materialia*, vol. 58, issue 9, pp. 3303-3312, May 2010. DOI: 10.1016/j.actamat.2010.02.004.
- [46] N. Yu, "Process parameter optimization for direct metal laser sintering (DMLS)," Ph.D. Dissertation, National University of Singapore, 2005. Available: <http://scholarbank.nus.edu.sg/handle/10635/14768>.
- [47] B. Van Hooreweder, R. Boonen, D. Moens, J. Kruth and P. Sas, "On the determination of fatigue properties of Ti6Al4V produced by selective laser melting," presented at *53rd AIAA/ASME/ASCE/AHS/ASC Structures, Structural Dynamics and Materials Conference*, Honolulu, Hawaii, 2012. DOI: 10.2514/6.2012-1733.
- [48] E. Sallica-Leva, A. L. Jardini and J. B. Fogagnolo, "Microstructure and mechanical behavior of porous Ti-6Al-4V parts obtained by selective laser melting," *Journal of the Mechanical Behavior of Biomedical Materials*, vol. 26, pp. 98-108, October 2013. DOI: 10.1016/j.jmbbm.2013.05.011.
- [49] ASTM Standard B243-13, "Standard Terminology of Powder Metallurgy," 2013. DOI: 10.1520/B0243-13.

- [50] H. V. Atkinson and S. Davies, "Fundamental aspects of hot isostatic pressing: An overview," *Metallurgical and Materials Transactions A*, vol. 31, issue 12, pp. 2981-3000, Dec 2000. DOI: 10.1007/s11661-000-0078-2.
- [51] J. B. Conway and L. H. Sjödal, *Analysis and Representation of Fatigue Data*, Materials Park, OH: ASM International, 1991.
- [52] ASTM Standard E468-11, "Standard Practice for Presentation of Constant Amplitude Fatigue Test Results for Metallic Materials," 2011. DOI: 10.1520/E0468-11.
- [53] Y. Lee and D. Taylor, "Stress-based fatigue analysis and design," in *Fatigue Testing and Analysis: Theory and Practice*, Burlington, MA: Elsevier, 2005, pp. 103.
- [54] ASTM Standard E739-10, "Standard Practice for Statistical Analysis of Linear or Linearized Stress-Life (S-N) and Strain-Life ( $\epsilon$ -N) Fatigue Data," 2010. DOI: 10.1520/E0739-10.
- [55] *Metallic Materials Properties Development and Standardization (MMPDS)*, 6th Edition, Battelle Memorial Institute, 2011.
- [56] ASTM Standard E466-07, "Standard Practice for Conducting Force Controlled Constant Amplitude Axial Fatigue Tests of Metallic Materials," 2007. DOI: 10.1520/E0466-07.
- [57] ASTM Standard F2924-14, "Standard Specification for Additive Manufacturing Titanium-6 Aluminum-4 Vanadium with Powder Bed Fusion," 2014. DOI: 10.1520/F2924.
- [58] ISO/ASTM Standard 52921:2013(E), "Standard Terminology for Additive Manufacturing Technologies-Coordinate Systems and Test Methodologies," 2013.
- [59] EOS GmbH Electro Optical Systems, "Material Data Sheet: EOS Titanium Ti64," 2011. Available: [http://ip-saas-eos-cms.s3.amazonaws.com/public/fe8d0271508e1e03/78e37a19596648ee1e1f660a5aa3e622/EOS\\_Titanium\\_Ti64\\_en.pdf](http://ip-saas-eos-cms.s3.amazonaws.com/public/fe8d0271508e1e03/78e37a19596648ee1e1f660a5aa3e622/EOS_Titanium_Ti64_en.pdf).
- [60] EOS GmbH Electro Optical Systems, "Technical Description: EOSINT M 280," 2010.
- [61] EOS GmbH Electro Optical Systems, "System Data Sheet: EOSINT M 280," 2013. Available: [http://ip-saas-eos-cms.s3.amazonaws.com/public/b1a64caa0c54d208/bc2d30d3f7b4b821634dfafa303ee441/systemdatasheet\\_M280.pdf](http://ip-saas-eos-cms.s3.amazonaws.com/public/b1a64caa0c54d208/bc2d30d3f7b4b821634dfafa303ee441/systemdatasheet_M280.pdf).

- [62] R. E. Williams and K. P. Rajurkar, "Study of wire electrical discharge machined surface characteristics," *Journal of Materials Processing Technology*, vol. 28, issue 1–2, pp. 127-138, 1991. DOI: 10.1016/0924-0136(91)90212-W.
- [63] Y. S. Liao, J. T. Huang and Y. H. Chen, "A study to achieve a fine surface finish in Wire-EDM," *Journal of Materials Processing Technology*, vol. 149, issue 1–3, pp. 165-171, 10 June 2004. DOI: 10.1016/j.jmatprotec.2003.10.034.
- [64] A. Burchi, Application Engineer, EOS of North America, Inc., Electronic message, 4 August 2014.
- [65] ASTM Standard E8/E8M, "Standard Test Methods for Tension Testing of Metallic Materials," 2013. DOI: 10.1520/E0008\_E0008M.
- [66] ASTM Standard E6-09b, "Standard Terminology Relating to Methods of Mechanical Testing," 2009. DOI: 10.1520/E0006-09BE01.
- [67] MTS Systems Corporation, "MTS Landmark Testing Solutions," Product Information Sheet, 2014. Available: <http://www.mts.com>.
- [68] ASTM STP588, "Manual on Statistical Planning and Analysis," 1975. DOI: 10.1520/STP588-EB.
- [69] S. Lin, Y. Lee and M. Lu, "Evaluation of the staircase and the accelerated test methods for fatigue limit distributions," *International Journal of Fatigue*, vol. 23, issue 1, pp. 75-83, January 2001. DOI: 10.1016/S0142-1123(00)00039-6.
- [70] I. J. Myung, "Tutorial on maximum likelihood estimation," *Journal of Mathematical Psychology*, vol. 47, issue 1, pp. 90-100, February 2003. DOI: 10.1016/S0022-2496(02)00028-7.
- [71] FEI Company, "An Introduction to Electron Microscopy," 2010. Available: <http://www.fei.com/documents/introduction-to-microscopy-document/>.
- [72] P. P. Milella, "Morphological aspects of fatigue crack formation and growth," in *Fatigue and Corrosion in Metals*, Milan, Italy: Springer, 2012, pp. 73-108. DOI: 10.1007/978-88-470-2336-9\_2.
- [73] M. J. Donachie, Ed., *Titanium: A Technical Guide*, Metals Park, OH: ASM International, 1988.

<b>REPORT DOCUMENTATION PAGE</b>				<i>Form Approved OMB No. 074-0188</i>	
<p>The public reporting burden for this collection of information is estimated to average 1 hour per response, including the time for reviewing instructions, searching existing data sources, gathering and maintaining the data needed, and completing and reviewing the collection of information. Send comments regarding this burden estimate or any other aspect of the collection of information, including suggestions for reducing this burden to Department of Defense, Washington Headquarters Services, Directorate for Information Operations and Reports (0704-0188), 1215 Jefferson Davis Highway, Suite 1204, Arlington, VA 22202-4302. Respondents should be aware that notwithstanding any other provision of law, no person shall be subject to a penalty for failing to comply with a collection of information if it does not display a currently valid OMB control number.</p> <p><b>PLEASE DO NOT RETURN YOUR FORM TO THE ABOVE ADDRESS.</b></p>					
<b>1. REPORT DATE (DD-MM-YYYY)</b> 26-03-2015		<b>2. REPORT TYPE</b> Master's Thesis		<b>3. DATES COVERED (From - To)</b> March 2014 - March 2015	
<b>TITLE AND SUBTITLE</b>  Investigation of the High-Cycle Fatigue Life of Selective Laser Melted and Hot Isostatically Pressed Ti-6Al-4v				<b>5a. CONTRACT NUMBER</b>	
				<b>5b. GRANT NUMBER</b>	
				<b>5c. PROGRAM ELEMENT NUMBER</b>	
<b>6. AUTHOR(S)</b>  Rekedal, Kevin D, Captain, USAF				<b>5d. PROJECT NUMBER</b> 14Y105	
				<b>5e. TASK NUMBER</b>	
				<b>5f. WORK UNIT NUMBER</b>	
<b>7. PERFORMING ORGANIZATION NAMES(S) AND ADDRESS(S)</b> Air Force Institute of Technology Graduate School of Engineering and Management (AFIT/ENY) 2950 Hobson Way, Building 640 WPAFB OH 45433-8865				<b>8. PERFORMING ORGANIZATION REPORT NUMBER</b>  AFIT-ENY-MS-15-M-212	
<b>9. SPONSORING/MONITORING AGENCY NAME(S) AND ADDRESS(ES)</b> Joint Aircraft Survivability Program Dennis Lindell 735 S Courthouse Road Suite 1100 Arlington, VA 22204-2489 dennis.lindell@navy.mil				<b>10. SPONSOR/MONITOR'S ACRONYM(S)</b>  JASP	
				<b>11. SPONSOR/MONITOR'S REPORT NUMBER(S)</b>	
<b>12. DISTRIBUTION/AVAILABILITY STATEMENT</b> Distribution Statement A. Approved for Public Release; Distribution Unlimited					
<b>13. SUPPLEMENTARY NOTES</b> This work is declared a work of the U.S. Government and is not subject to copyright protection in the United States.					
<b>14. ABSTRACT</b> Experimental research was conducted on the effectiveness of Hot Isostatic Pressing (HIP) to improve the high-cycle fatigue life of Selective Laser Melted Ti-6Al-4v (SLM Ti-64). A thorough understanding of the fatigue life performance for additively manufactured parts is necessary before such parts are utilized in an operational capacity in Department of Defense (DoD) systems. Such applications include the rapid, on-demand fabrication of replacement parts during contingency operations or the production of light-weight topology-optimized components. This research assesses the fatigue life of SLM Ti-64 test specimens built directly to net dimensions without any subsequent surface machining. The configuration is designed as representative of end-use parts where further surface machining is unavailable or undesirable. Past research suggests utilization of HIP as a densification process to reduce the negative impact on fatigue life from internal porosity within SLM Ti-64. The impact of HIP on the rough surface of SLM Ti-64 to remove stress concentrations on the surface is not addressed in literature. The experimental data from this research demonstrates HIP improves high-cycle fatigue-life of un-machined test specimens by 61.4% at a maximum stress level of 500 MPa and 102% at a maximum stress level of 300 MPa.					
<b>15. SUBJECT TERMS</b> Additive Manufacturing, Selective Laser Melting, Ti-6Al-4v					
<b>16. SECURITY CLASSIFICATION OF:</b>			<b>17. LIMITATION OF ABSTRACT</b>  UU	<b>18. NUMBER OF PAGES</b>  140	<b>19a. NAME OF RESPONSIBLE PERSON</b> Maj David Liu, AFIT/ENY
<b>a. REPORT</b>  U	<b>b. ABSTRACT</b>  U	<b>c. THIS PAGE</b>  U			<b>19b. TELEPHONE NUMBER (Include area code)</b> (937) 255-3636, ext 4542 david.liu@afit.edu